

1991

# Formation of Superhexagonal Chromium Hydride by Exposure of Chromium Thin Film to High Temperature, High Pressure Hydrogen in a Ballistic Compressor

Yi Pan  
*Portland State University*

Follow this and additional works at: [https://pdxscholar.library.pdx.edu/open\\_access\\_etds](https://pdxscholar.library.pdx.edu/open_access_etds)

**Let us know how access to this document benefits you.**

---

## Recommended Citation

Pan, Yi, "Formation of Superhexagonal Chromium Hydride by Exposure of Chromium Thin Film to High Temperature, High Pressure Hydrogen in a Ballistic Compressor" (1991). *Dissertations and Theses*. Paper 1243.

<https://doi.org/10.15760/etd.1242>

This Dissertation is brought to you for free and open access. It has been accepted for inclusion in Dissertations and Theses by an authorized administrator of PDXScholar. Please contact us if we can make this document more accessible: [pdxscholar@pdx.edu](mailto:pdxscholar@pdx.edu).

FORMATION OF SUPERHEXAGONAL CHROMIUM HYDRIDE BY  
EXPOSURE OF CHROMIUM THIN FILM TO HIGH TEMPERATURE,  
HIGH PRESSURE HYDROGEN IN A BALLISTIC COMPRESSOR

by

YI PAN

A dissertation submitted in partial fulfillment of the  
requirement for the degree of

DOCTOR OF PHILOSOPHY  
in  
ENVIRONMENTAL SCIENCES AND RESOURCES: PHYSICS

Portland State University  
1991

TO THE OFFICE OF GRADUATE STUDIES:

The members of the Committee approve the dissertation  
of Yi Pan presented in June 27, 1991.

[Redacted Signature]

Makoto Takeo, Chair

[Redacted Signature]

John Dash, co-Chair

[Redacted Signature]

Donald Howard

[Redacted Signature]

Erik Bodegom

[Redacted Signature]

Marvin H. Beeson

[Redacted Signature]

David H. Peyton

[Redacted Signature]

Bruce W. Brown

APPROVED:

[Redacted Signature]

Pavel Smejtek, Director of Environmental Sciences and  
Resources Doctoral Program

[Redacted Signature]

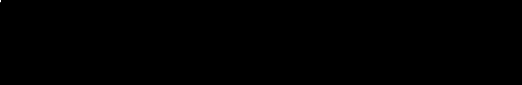
C. William Savery, Vice Provost for Graduate Studies and  
Research

AN ABSTRACT OF THE DISSERTATION OF Yi Pan for the Doctor of  
Philosophy in Environmental Sciences and Resources:Physics  
presented in June 27, 1991.

Title: Formation of Superhexagonal Chromium Hydride by  
Exposure of Chromium Thin Film to High Temperature,  
High Pressure Hydrogen in a Ballistic Compressor

APPROVED BY THE MEMBERS OF THE DISSERTATION COMMITTEE:

  
Makoto Takeo, Chair

  
John Dash, co-Chair

  
Donald Howard

  
Erik Bodegom

  
Marvin H. Beeson

  
David H. Peyton

  
Bruce W. Brown

The interaction of hydrogen with metals has great environmental significance in problems ranging from the catastrophic failure of materials due to hydrogen embrittlement to safe and efficient storage of hydrogen as a metal hydride.

Chromium (Cr) is widely used as an alloying agent to produce materials such as stainless steel and as an electroplated coating on materials to prevent corrosion and to minimize wear. Hydrogen which co-deposits with chromium during electroplating forms hexagonal close packed CrH or face centered cubic CrH<sub>2</sub> which cracks the deposit.

The behavior of hydrogen in Cr, especially the crystal structure modifications of metal Cr when it is exposed to hot, dense hydrogen gas is not completely understood. In equilibrium study, chromium hydride has been found of hexagonal close packed structure under 400 °C with high hydrogen pressure. Experiments at higher temperatures are limited by the equipment and technology. This dissertation describes a novel, non-equilibrium method which was used to synthesize a new chromium hydride phase.

Single crystal, body centered cubic Cr thin films were prepared by vacuum evaporation. These films were exposed to high temperature (close to the melting point of Cr), high pressure hydrogen gas in a ballistic compressor. This was followed by rapid cooling ( $>10^5$  °C/s) to room temperature.

Using the transmission electron microscope (TEM),

second phase particles of superhexagonal structure, which has lattice constant  $A=4.77\text{\AA}$  and  $C/A=1.84$ , are found in the films. This structure has a volume per Cr atom slightly large than that of hexagonal closed packed CrH, so that the superhexagonal structure may contain more hydrogen than the hexagonal close packed CrH. The superhexagonal particles have a definite orientation relationship with the matrix:  $[021]_{sh} // [001]_b$  and  $(2\bar{1}2)_{sh} // (\bar{1}\bar{1}0)_b$ . The superhexagonal structure is quite stable in air and at room temperature, but decomposes to body centered cubic Cr when heated by the electron beam illumination in the TEM. No such particles were observed in Cr films exposed to pure argon under similar conditions in the ballistic compressor.

Positive identification of hydrogen content was obtained by high-temperature vacuum extraction in a discharge tube. After vacuum extraction, hydrogen spectrum was observed, and the intensity of electron diffraction from superhexagonal structure decreased.

Using an energy dispersive spectrometer with the capability of detecting elements down to atomic number six (carbon), no changes in composition of the films were found by comparing the characteristic x-ray spectra of the same film before and after exposure to hot, dense hydrogen in the ballistic compressor.

This result suggests that this non-equilibrium method may be used for other metal-hydrogen system to obtain new

structural phases that are of scientific or technological interest.

## ACKNOWLEDGEMENTS

I am very grateful to Dr. Makoto Takeo, my academic advisor, for giving me the interesting topic and guiding me throughout the entire research. His advice, judgement, and instructions were helpful in bringing this research to a fruitful conclusion. I would like to thank Dr. John Dash, co-advisor of my Ph. D. program, for his valuable suggestions, his experimental experience and technical advice, especially electron microscopy, upon which a major portion of this dissertation depends.

I want to express my appreciation to Mr. Rudi Zupan, Mr. Brian McLaughlin, and late Mr. Garo Arakelian, for their help in maintenance of the apparatus, especially the ballistic compressor. I also give special thanks to Dr. Gary Gard, Dr. Pui-Tak Leung, and Mr. Wen Li, for their kind help. I would like to thank the faculty and staff in the Physics Department, for their friendship and support.

I wish to thank my uncle and aunt Dr. Shang Yi and Ruth Pan Chen, for encouraging me to further my education at Portland State University. Through their efforts, I have been fortunate to work under the guidance of Dr. M. Takeo, to complete this dissertation.

Finally, I must thank my family, especially my parents, Yuehua Shao and Fen Pan, to whom this is dedicated.



## TABLE OF CONTENTS

		PAGE
	ACKNOWLEDGEMENTS . . . . .	iii
	LIST OF TABLES . . . . .	vii
	LIST OF FIGURES . . . . .	ix
 CHAPTER		
I	INTRODUCTION . . . . .	1
	Motivation for Research on Metal-Hydrogen Systems . . . . .	2
	Review on Cr-H system . . . . .	6
	Purpose and Methods of This Research	10
	Procedures of Experiment . . . . .	11
II	EPITAXIAL GROWTH OF Cr THIN FILMS . . . . .	12
	Introduction . . . . .	12
	Epitaxial Growth of Cr Thin Film . . . . .	12
III	EXPOSURE OF Cr THIN FILM TO HOT DENSE H <sub>2</sub> GAS	19
	Introduction . . . . .	19
	Ballistic Compressor . . . . .	19
	Exposure . . . . .	22
IV	MICROGRAPHS AND DIFFRACTION PATTERNS	
	BY TEM . . . . .	25
	Introduction . . . . .	25
	The Grown Particles . . . . .	25

		v
	Electron Diffraction Patterns . . . . .	28
	Summary . . . . .	43
V	SUPERHEXAGONAL STRUCTURE . . . . .	44
	Introduction . . . . .	44
	Superhexagonal Structure . . . . .	44
	Orientation of Superhexagonal in Bcc	
	Matrix . . . . .	51
	Phase Transformation from Bcc to	
	Superhexagonal . . . . .	54
	Summary . . . . .	55
VI	STABILITY OF SUPERHEXAGONAL STRUCTURE . .	56
VII	HYDROGEN DETECTION AND CHEMICAL COMPOSITION	
	ESTIMATION . . . . .	59
	Introduction . . . . .	59
	High Temperature Vacuum Extraction .	59
	Chemical Composition Estimation by	
	Other Methods . . . . .	62
	Summary . . . . .	72
VIII	X-RAY DIFFRACTION EXPERIMENT AND DISCUSSION	73
	Introduction . . . . .	73
	X-ray Diffraction Experiment . . . . .	73
	Discussion . . . . .	77
IX	CONCLUSION . . . . .	84
	REFERENCES . . . . .	86

## APPENDICES

A	PROCEDURE FOR MAKING SINGLE CRYSTAL Cr THIN FILMS . . . . .	91
B	PROCESSING OF ELECTRON MICROSCOPE DATA . .	94
C	COMPUTER PROGRAM . . . . .	105
D	CuK <sub>β</sub> PEAKS IN THE X-RAY SPECTRA FROM GENERAL ELECTRIC XRD-5 D/F UNIT . . . . .	117

## LIST OF TABLES

TABLE		PAGE
I	Solubility of H in Bcc Cr . . . . .	7
II	Condition for Epitaxial Growth of Cr Thin Film . . . . .	16
III	Thermodynamic Condition of Exposure . . . . .	24
IV	Observed and Theoretical d-spacings and Angles from Figure 10 (c) . . . . .	31
V	Observed and Theoretical d-spacings and Angles from Figure 13 (b) . . . . .	37
VI	Observed and Theoretical d-spacings and Angles from Figure 16 (c) . . . . .	41
VII	Lattice Constants and Unit Cell Volumes for Cr, CrH and Superhexagonal Chromium Hydride . . . . .	45
VIII	Diffraction Pattern Indices in both Sh and Hcp Coordinates . . . . .	49
IX	TEM Observation from Figure 24 and Literature d-spacings of Cr <sub>2</sub> O <sub>3</sub> (Å) . . . . .	64
X	TEM Observation from Figure 25 and Literature d-spacings of Cr <sub>3</sub> O <sub>4</sub> (Å) . . . . .	64
XI	Thermodynamic Condition of Exposure of Cr Thin Films to Ar . . . . .	66

XII	X-ray Diffraction of Cr Thin Film on Mo Grid after Five Exposures to H <sub>2</sub> . . . .	75
XIII	X-ray Diffraction of Cr Thin Film Deposited on Glass Slide after Six Exposures to H <sub>2</sub> .	76
XIV	X-ray Diffractions of Various Samples . . . .	119

LIST OF FIGURES

FIGURE		PAGE
1	Formation (■◆●) and (□◇○) Decomposition Curves for Chromium Hydride in a $P_{H_2}$ , T Plot . . . . .	9
2	Vacuum Chamber . . . . .	14
3	Cr Thin Film as Deposited . . . . .	17
4	PSU Ballistic Compressor . . . . .	20
5	Free Piston . . . . .	21
6	Pressure Oscillograph of the Test Gas $H_2$ . . . . .	24
7	Cr Thin Film Experienced Five Exposures to $H_2$ . . . . .	26
8	Dark Field Micrograph from New Structure in a 4-time $H_2$ -exposed Cr Film . . . . .	27
9	Electron Diffraction Pattern in $[021]_{sh}$ Zone . . . . .	29
10	Analysis of Diffraction Pattern in $[021]_{sh}$ Zone . . . . .	30
11	Diffraction at Tilt Angle $40'$ . . . . .	34
12	Electron Diffraction Pattern in $[\bar{2}23]_{sh}$ Zone . . . . .	35
13	Analysis of Diffraction Pattern in $[\bar{2}23]_{sh}$ Zone . . . . .	36
14	Electron Diffraction from an Area Densely Populated with Precipitate Particles . . . . .	38
15	Micrograph of Figure 14 . . . . .	39

16	Analysis of Diffraction Pattern in $[210]_{sh}$ Zone . . . . .	40
17	Model of the Undistorted Superhexagonal Structure . . . . .	47
18	Hcp and Bcc Models Show Their Relative Orientation . . . . .	53
19	Phase Transformation Correspondence for Bcc to Hcp . . . . .	55
20	Cr Thin Film 79 Days after Exposures to $H_2$ . . .	56
21	Superhexagonal Structure Bombarded by Electron Beam . . . . .	57
22	Spectra from Discharge Tubes . . . . .	61
23	Structure Reversion . . . . .	61
24	$Cr_2O_3$ on Cr Thin Film . . . . .	63
25	$Cr_3O_4$ on Cr Thin Film . . . . .	65
26	SEM Image of Cr Thin Film on the Mo grid . . .	68
27	EDS Spectrum from As-deposited Cr Film . . . .	69
28	EDS Spectrum from $H_2$ -exposed Cr Film . . . . .	70
29	EDS Spectrum from Ar-exposed Cr Film . . . . .	71
30	Image Rotation by intermediate lens . . . . .	100
31	Image Rotation by projector lens . . . . .	101
32	Image Rotation by intermediate lens . . . . .	102
33	Image Rotation by projector lens . . . . .	103

## CHAPTER I

### INTRODUCTION

This dissertation describes the experiments in which chromium (Cr) hydride of superhexagonal crystal structure is synthesized and identified.

Chapter I presents the motivation for my research on metal-hydrogen system, a brief review of Cr-H system and the methods and procedures employed in this research. Chapter II presents the epitaxial growth of Cr thin films by vapor-deposition. Chapter III presents experiments in which the superhexagonal chromium hydride is synthesized. Chapter IV presents an electron microscopic analysis of the superhexagonal structure of chromium hydride. Chapter V describes the superhexagonal structure and its relative orientation to the body centered cubic (bcc) matrix on Cr thin film. Chapter VI presents a study of stabilities of the superhexagonal structure with time and temperature. Chapter VII presents a high-temperature vacuum extraction experiment in which hydrogen content in the superhexagonal structure is spectroscopically detected by gas discharge method. Chapter VIII gives a discussion on experiments with x-ray diffraction and energy dispersive spectrometry (EDS),



and some perspectives for future experiments. Chapter IX is a brief conclusion.

#### MOTIVATION FOR RESEARCH ON METAL-HYDROGEN SYSTEMS

The motivation of research on hydrogen in metals is generated from the unique properties and a great variety of both immediate and potential applications of metal hydrides, which are closely related to environmental sciences and resources.

#### Hydrogen Embrittlement

Hydrogen can go into a metal by directly reacting with the metal and being absorbed during electrochemical process such as pickling or electroplating operations. Hydrogen in metals can make the metal crystal expand or change its crystal structure by forming a metal hydride. Very often metal hydrides are quite brittle [1]. This phenomenon is called hydrogen embrittlement.

The fact that hydrogen embrittlement can cause failure of the metal parts is well known, but the mechanism of hydrogen embrittlement in metal and the nature of chemical bonding in metallic hydrides is still poorly understood. Therefore, experimental and theoretical research to provide a general explanation of the mechanism of hydrogen embrittlement is much needed.

### Powder Metallurgy and Alloying

Another characteristic property of metal hydrides is that they are easily decomposed and release  $H_2$  at higher temperatures. Metallurgists use these unique properties of metal hydrides in powder metallurgy.

Preparing high-purity metal powder for powder metallurgy becomes more and more difficult as the desired powder size is smaller and smaller. This is caused by the malleability of pure metals and possible contamination by surrounding media. To overcome these difficulties, brittle metal hydrides can be used. Firstly, they can be ground more easily to a desired mesh size; secondly, since hydrogen released during sintering serves as an effective protective atmosphere, impurities can then be kept to a minimum [1].

### Nuclear Reactor Materials

The prime function of a reactor is to release and control neutrons, which are the principal particles involved in the fission reaction. Hydrogen has unique properties in its reaction with neutrons. Because the mass of the hydrogen atom is close to the mass of a neutron, the kinetic energy of a neutron may dissipate efficiently by elastic collision with a hydrogen nucleus. Metal hydrides used in a mobile nuclear reactor where the volume and weight are the dominant considerations, such as a power source for aircraft [2], submarines [3] and spaceships [4], would greatly reduce

reactor volume and weight. A detail technical specification for the mobile nuclear reactors has been described in [5].

#### Storage and Purification of Hydrogen

Hydrogen is an ideal high-energy fuel without significantly polluting the environment, because the product of its combustion is simply water. Hydrogen has been used as fuel in fuel cells which serve as the power source of spaceships [6]. Hydrogen is also widely used in the food industry for hydrogenation of oils of animal and vegetable origin, and in power plants for cooling electric generating equipment. However, the present supply of hydrogen in compressed gas and liquid forms limit its applications because of heavy and bulky cylinders and mechanical work for liquefaction of hydrogen (14,450 kJ/kg [7]). Metal hydrides can be used as efficient portable sources of hydrogen because the density of hydrogen in metals is as high as liquid hydrogen. Pure hydrogen can be obtained when uranium hydride decomposes on heating, retaining oxygen and nitrogen in the uranium as the oxide and nitride, respectively [1].

#### Hydrogen Pump for Utilization of Solar and Geothermal Heat

Conventional central power plants employ Rankine power cycle with water as the working fluid. In this cycle, a water pump or a compressor is necessary to produce high pressure, so that the net output of mechanical energy from

the turbine is reduced. Only 30-40% of their thermal input can be converted into electricity [8].

The efficiency can be substantially increased by using a hydrogen pump or hydrogen compressor in which  $H_2$  is the working fluid. The hydrogen can be compressed to a very high pressure or restored to the hydride by a slight increase or decrease the temperature of the metal hydride [9], and thus energy resources such as geothermal and solar heat can be used for the absorption-desorption cycle. The high pressure hydrogen is used to drive the turbine. Hydrogen gas has high thermal conductivity, which minimizes the regenerator cost and enthalpy loss. Hydrogen gas is also stable at typical working temperatures.

There are several high efficiency power cycles with some well-known metal or alloy hydrides suggested by different authors [10], in which, the overall efficiency can be increased from 30-40% to 50%. The major problem with using  $H_2$  is embrittlement of the materials used for the turbines and heat exchangers.

### Summary

Metal hydrides used in energy generation, utilization and conversion, as well as many other potential applications may make a substantial change in economy and the people's daily life.

## REVIEW ON Cr-H SYSTEM

Although metal hydrides have applications of great significance, the data for their formation and decomposition, and for their physical and chemical properties are limited. For example, although Cr is one of the most widely used metals in alloying and electroplating, the behavior of hydrogen in chromium, and especially the crystal structure modifications of the metal chromium when it is exposed to hot, dense hydrogen gas are not completely known. This research is centered on this particular topic in Cr-H system.

Electrolytic Chromium Hydride

Chromium hydride was first identified in an electrolytic method in 1947 [11]. The crystal structure of chromium deposited from chromic acid solution is either the hexagonal close-packed (hcp), with reported composition CrH, or the face-centered cubic (fcc), with reported composition CrH<sub>2</sub>, depending on the electrolysis conditions. In both hydrides, Cr atoms form the crystal lattice and H atoms occupy the interstitial positions. Unit cell dimensions of chromium hydrides were determined by x-ray diffraction [11,12]. At room temperature, the hcp structure from electroplating was rather stable. An x-ray diffraction study showed that more than two years after plating, the hcp structure was still persistently present in the plated layer

[13]. In marked contrast, when ground into powder, the hcp structure changed to bcc Cr (under normal conditions, the metal Cr has bcc crystal structure) in about 40 days at room temperature [13,14]. Fcc chromium hydride indirectly transformed into bcc Cr after forming an intermediate hcp structure. With increasing temperature, both hcp and fcc structures were rapidly transformed into bcc.

#### Directly Synthesized chromium hydride

The solubility of hydrogen in bcc Cr is very small [15]. TABLE I shows that with increase in temperature, the solubility of hydrogen in chromium increases. Nevertheless the small amount of hydrogen in the interstitial sites of bcc Cr does not cause the lattice constant to change significantly [16]. In order to observe hydrogen effects on the crystal structure of Cr, some extreme experimental conditions--high pressure and high temperature--may be necessary.

TABLE I  
SOLUBILITY OF H IN BCC Cr [15]

t (°C)	400	800	1200
H/Cr	$0.13 \times 10^{-4}$	$0.44 \times 10^{-4}$	$2.62 \times 10^{-4}$

Note: solubility is expressed as atomic ratio.

In 1972, chromium hydride was first synthesized by direct reaction of metallic chromium thin foil of 20  $\mu\text{m}$  in

thickness with gaseous hydrogen under a high hydrogen pressure (22 kbar) at 150 °C [17]. The x-ray diffraction pattern from the hydride showed that the crystal structure was hcp. In 1976, the dependence of the formation and decomposition temperatures of hcp chromium hydride on hydrogen pressure over a broad temperature range (up to 400 °C), at pressures up to 20 kbar was studied [18]. Instead of a thin foil, chromium powder having a grain size of 0.05-0.10 mm was used. At temperatures below 200 °C, formation of chromium hydride on these powder specimens was not observed. In Figure 1, the T vs.  $P_{H_2}$  curves summarize data obtained by different authors and experimental methods (either isothermal or isobaric) for the formation and decomposition of hcp chromium hydride [18]. The formation curve is composed by solid symbols, and the decomposition curve by hollow symbols. From these curves, the decomposition pressure at 25 °C was estimated as about 700 atm [19]. Differing from chromium hydride prepared by electrolytic method, the hydride by direct-synthesis had no fcc structure, but only hcp structure. It was unstable in air at atmospheric pressure and completely decomposed in 3-4 hours [18].

Synthesis of chromium hydride by direct reaction of metallic chromium and  $H_2$  requires high  $H_2$  pressure (16-20 kbar). The temperatures in these experiments were under 400 °C. In order to investigate Cr- $H_2$  direct reaction at higher

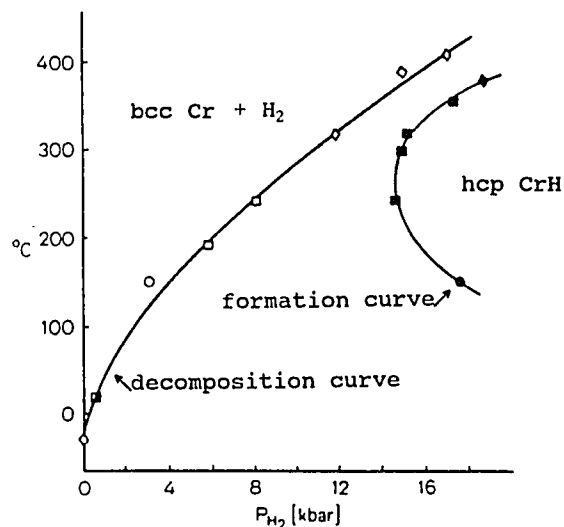


**Figure 1.** Formation (◆◆) and decomposition (◇◇) curves for chromium hydride in a  $P_{H_2}$ ,  $T$  plot [18].

temperature, special equipment and experimental methods are needed.

Above experiments for investigating the direct reaction of Cr and H<sub>2</sub> were performed under equilibrium condition, either isobaric or isothermal. With a special piece of equipment--a ballistic compressor (BC)--at PSU, a non-equilibrium method is developed. When Cr thin film was exposed to a hot dense gas mixture of argon and hydrogen at 1700 °C and 10<sup>7</sup> Pa by using the BC, strong streaks along bcc <100> direction appeared in the electron diffraction pattern [20]. This experiment suggests that hydrogen modifies Cr crystal structure under the conditions of BC.



## PURPOSE AND METHODS OF THIS RESEARCH

Purpose

The purpose of this research is to investigate the modification of crystal structure of metallic Cr under high pressures of H<sub>2</sub> at temperatures close to melting point of Cr (1875 °C [21]).

Method

This research employed the non-equilibrium method with a unique apparatus--the BC. The BC can generate hot, dense gases at more than  $3 \times 10^3$  atm and 6000 °K for a short time (about a millisecond). If Cr samples are made thin enough, the temperature of the thin samples will be close to that of gases to which they are exposed. By the subsequent rapid cooling ( $>10^5$  °C/s), the physical and chemical reactions which happened at peak pressure and temperature may be frozen and observed under normal conditions. In this way a non-equilibrium thermodynamic and mechanical condition is imposed on the Cr samples. This non-equilibrium method has been developed to investigate the effects of hot, dense gases on Cr [20,22] and other materials [23]. The present research on Cr-H system is an extension of previous work. Different from [20], it uses pure hydrogen as test gas instead of Ar and H<sub>2</sub> mixture.

## PROCEDURES OF EXPERIMENT

1. Preparation of Cr Thin Film

Thin Cr films with a known crystal structure and orientation are prepared by epitaxial growth on rock salt substrates.

2. Exposure of Cr Thin Films to H<sub>2</sub>

Cr thin film samples are exposed to hot, dense hydrogen gas in the BC. The experimental thermodynamic conditions depends on the peak temperature and pressure in the BC.

3. Investigation

Crystal Structure. Before and after exposures to hot, dense H<sub>2</sub>, samples of Cr thin films are investigated with a transmission electron microscope (TEM) and an x-ray diffractometer to investigate the modification in crystal structure.

Hydrogen Content. A qualitative analysis for H<sub>2</sub> content is conducted by high temperature vacuum extraction. Samples of Cr thin film exposed to H<sub>2</sub> are sealed into a discharge tube and observation of the hydrogen spectrum from the discharge tube is performed.

A scanning electron microscope (SEM) equipped with an x-ray energy dispersive spectrometer (EDS) is also used to examine the samples before and after exposure to hot dense H<sub>2</sub>.

## CHAPTER II

### EPITAXIAL GROWTH OF Cr THIN FILMS

#### INTRODUCTION

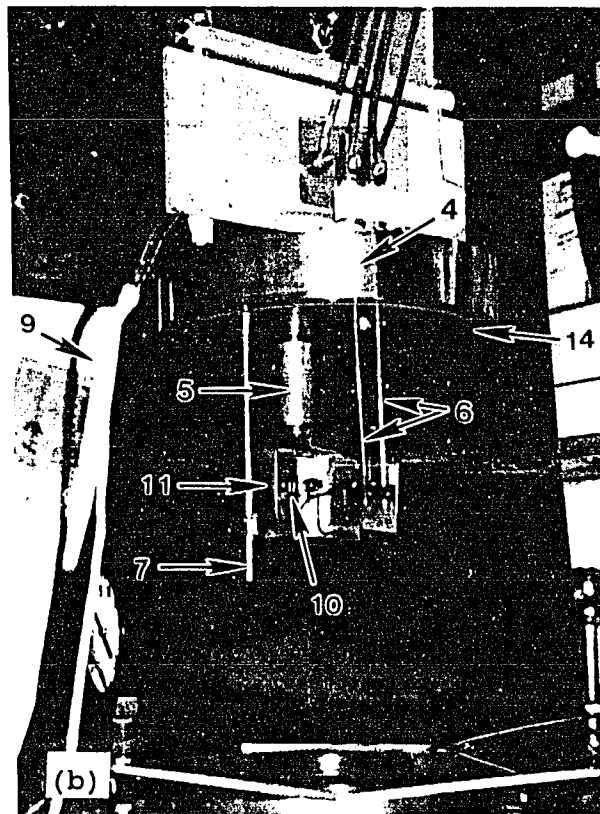
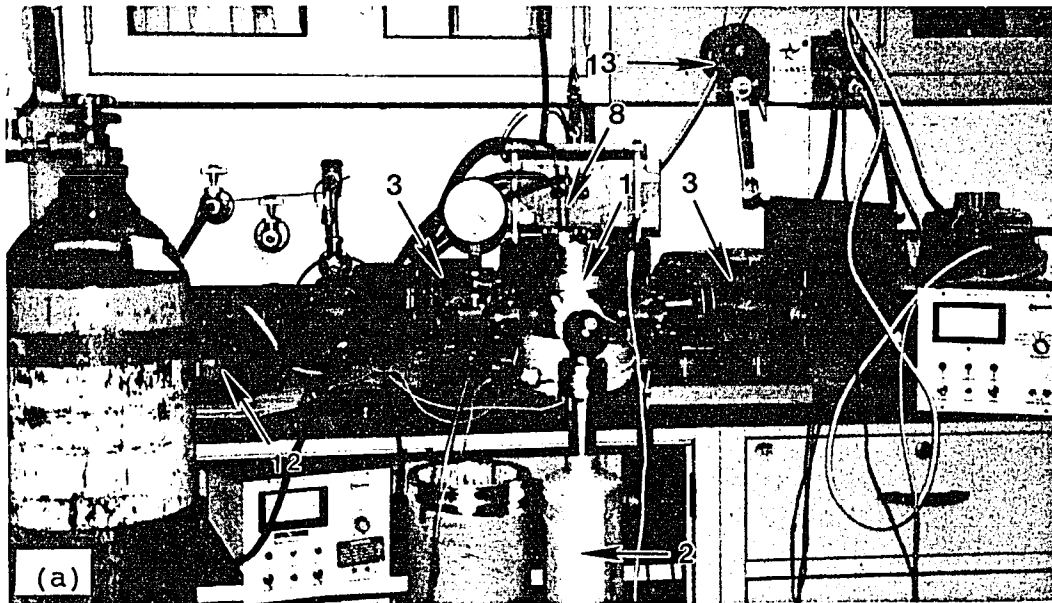
In order to obtain crystallographic information from the TEM, thin films with known crystal structure and orientation are needed. It is known that the crystal structure of metallic thin films depend on the composition of the substrate, its temperature, the residual gas pressure, the deposition rate, film thickness and some other factors in the process of deposition [24-27]. Cr thin films have been vapor-deposited on various substrates with different experimental conditions [28-39]. The thin film microstructure was either amorphous or polycrystalline depending on the experimental conditions.

#### EPITAXIAL GROWTH OF Cr THIN FILM

Epitaxy denotes the formation of single crystalline films usually on single crystal substrates either of the same substance, which is homo-epitaxy, or of other substances, which is hetero-epitaxy. Rock salt single crystal was used as the substrate in making Cr thin film, since it is easily separated from Cr thin film by being dissolved in the water.

### Description of Apparatus

Figure 2 depicts the vacuum chamber used for vapor deposition of Cr thin film in this work. Cr powder was evaporated in vacuum and deposited on the surface of cleaved rock salt, forming a thin film. The chamber was made of stainless steel with an inner volume:  $v = \pi \times r^2 \times h = 3.14 \times 7.52^2 \times 16 = 2.8 \times 10^3 \text{ cm}^3$ . One molecular absorption pump (DSP-651) and two ion pumps (Varian 911-5032 and 911-5034) are attached to the chamber to generate an oil vapor-free vacuum. On the cap of the chamber were mounted a substrate oven, electrode rods, and a supporting rod. The substrate oven was composed of a copper body (with volume =  $\pi \times r^2 \times h = 3.14 \times 1.4^2 \times 6.3 = 38.8 \text{ cm}^3$ ) with two electric heaters embedded in it. The copper body had good thermal conductivity so that a uniform high temperature region could be achieved in the oven. Two copper tubes were used to carry cooling substances into and out of the oven in order to lower the temperature quickly. A chromel-alumel thermocouple was fixed inside the copper body. The substrate rock salt was mounted on the substrate holder at the lower portion of the body; 5 cm underneath was a tungsten basket where the chromium powder was vaporized by an electric current. The tungsten basket was kept in a stainless steel case to prevent unnecessary deposition on the chamber wall and to keep the chamber clean. The case had a hole on the top to let the chromium vapor out. The



1. vacuum chamber
2. absorption pump
3. ion pump
4. chamber cap
5. substrate oven
6. electrode rods
7. supporting rod
8. copper tubes
9. thermocouple wires
10. tungsten basket
11. stainless steel case
12. variac
13. ratchet mechanism
14. o-ring

Figure 2. Vacuum chamber. (a). the outside view; (b). the inside view.

deposit on the inner surface of the case was easily removed by a hydrochloric acid solution. The electric current going through the tungsten basket was controlled by a variac. The cap of the vacuum chamber could be lifted by a pulley and ratchet mechanism when the chamber needed to be opened. An O-ring without vacuum grease was used for sealing between the cap and the chamber.

#### Experimental Conditions

It was reported [40] that single crystal Cr thin films (bcc) with the (001)<sub>0</sub> plane parallel to the surface were obtained by vapor-deposition in an ultra-high vacuum of  $10^{-9}$  torr. The substrate rock salt was heated to 250-300 °C. The deposition rate was 3 Å/sec. With a relatively poor vacuum of  $10^{-6}$  torr, the thin films were always polycrystalline but with highly preferred orientation.

With the vacuum system used in this work, the best vacuum is  $2-3 \times 10^{-8}$  torr. It took 2 to 3 days to pump down to  $10^{-7}$  torr, and a week or so to pump down to the best vacuum. However, the vacuum of  $6-8 \times 10^{-7}$  torr can be easily obtained in one day or over night pumping. Because it is known that higher deposition rates and higher substrate temperatures may help epitaxial growth, the highest evaporation rate and highest substrate temperature (515-525 °C) were used to compensate for the relatively poor vacuum. It was noted [41] that heating rock salt above 500 °C could

cause sublimation of rock salt and result in contaminating the deposit film. But in the present work, sublimation was not a problem in making chromium films. This was proven by EDS spectra which detected neither chlorine nor sodium in the deposit films.

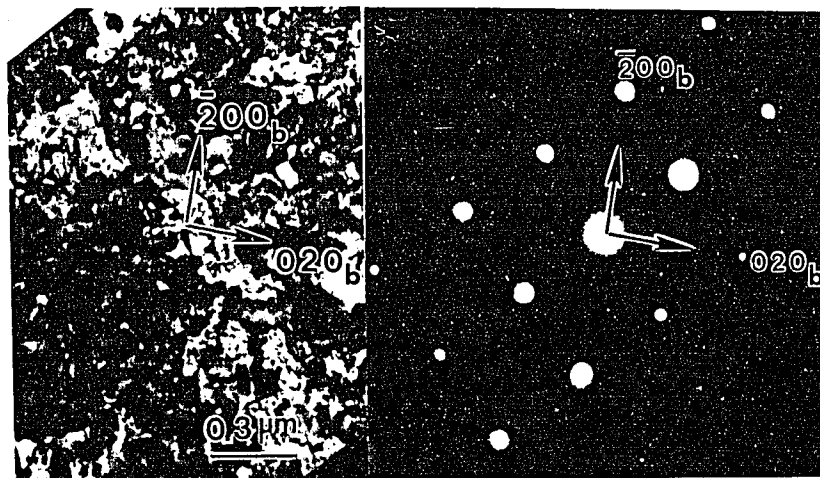
The conditions for epitaxial growth of Cr thin films are listed in TABLE II. The deposition was almost instantaneously completed by manually turning the variac rapidly to its highest position. The chromium powder (99.996%) is supplied by AESAR and the rock salt by AESAR (optical grade) and PELCO. A more detail procedure for preparation of Cr thin film by the vapor deposition is put in APPENDIX A.

TABLE II  
CONDITION FOR EPITAXIAL GROWTH OF Cr THIN FILM

	this work	literature [38]
Substrate	NaCl	NaCl
Temp. of sub.	515 °C	250-300 °C
Vacuum	$6-8 \times 10^{-7}$ torr	$10^{-9}$ torr
Deposition rate	hundreds of Å/s	3 Å/s

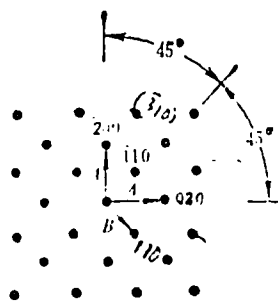
#### Single Crystal Cr Thin Film Sample

By dissolving the rock salt substrate in water, the Cr thin film was floated on the water due to the surface tension. If the thin film was cut into small pieces (2mm x



(a)

(b)



(c)

Figure 3. Cr thin film as deposited. (a). micrograph, (b). electron diffraction pattern. (c). standard electron diffraction pattern for bcc [001] zone. Note: The Cr film is a single crystalline and its surface is parallel to  $(001)_b$  plane.



2mm), then it was easy to sandwich them with Mo folding grids for TEM observation.

Figure 3 shows the TEM micrograph (a) and the electron diffraction pattern of single crystal (b) from a chromium thin film as deposited. Comparing with the standard electron diffraction pattern of bcc  $[001]_b$  zone (c)  $[42-44]$ , the single crystal film had bcc structure and its surface was parallel to the  $(001)_b$  plane. This was the same crystal structure and orientation as obtained by  $[41]$ .

## CHAPTER III

### EXPOSURE OF Cr THIN FILM TO HOT DENSE H<sub>2</sub> GAS

#### INTRODUCTION

A free-piston type ballistic compressor (BC) has been a key apparatus in the research on the effect of hot, dense gases on various materials [22,23]. It can produce hot, dense gases with density comparable to liquids. Samples are mounted on the piston head and the exposure can be easily repeated on the same sample under the same conditions.

#### BALLISTIC COMPRESSOR

Figure 4 shows the BC used in this work, which consists of a horizontally-mounted 2.9 meter long, 5.7 cm inner diameter tube, attached on one end to the driving gas reservoir and on the other to the high pressure compartment. A free piston is put inside the tube. The front of the piston is filled with test gas and the back with driving gas. Driven by the high pressure gas behind the piston, the released piston flies along the tube and compresses the test gas into the high pressure compartment at high temperature and pressure. The peak gas condition lasts about a millisecond. The recoil of the piston then produces a rapid

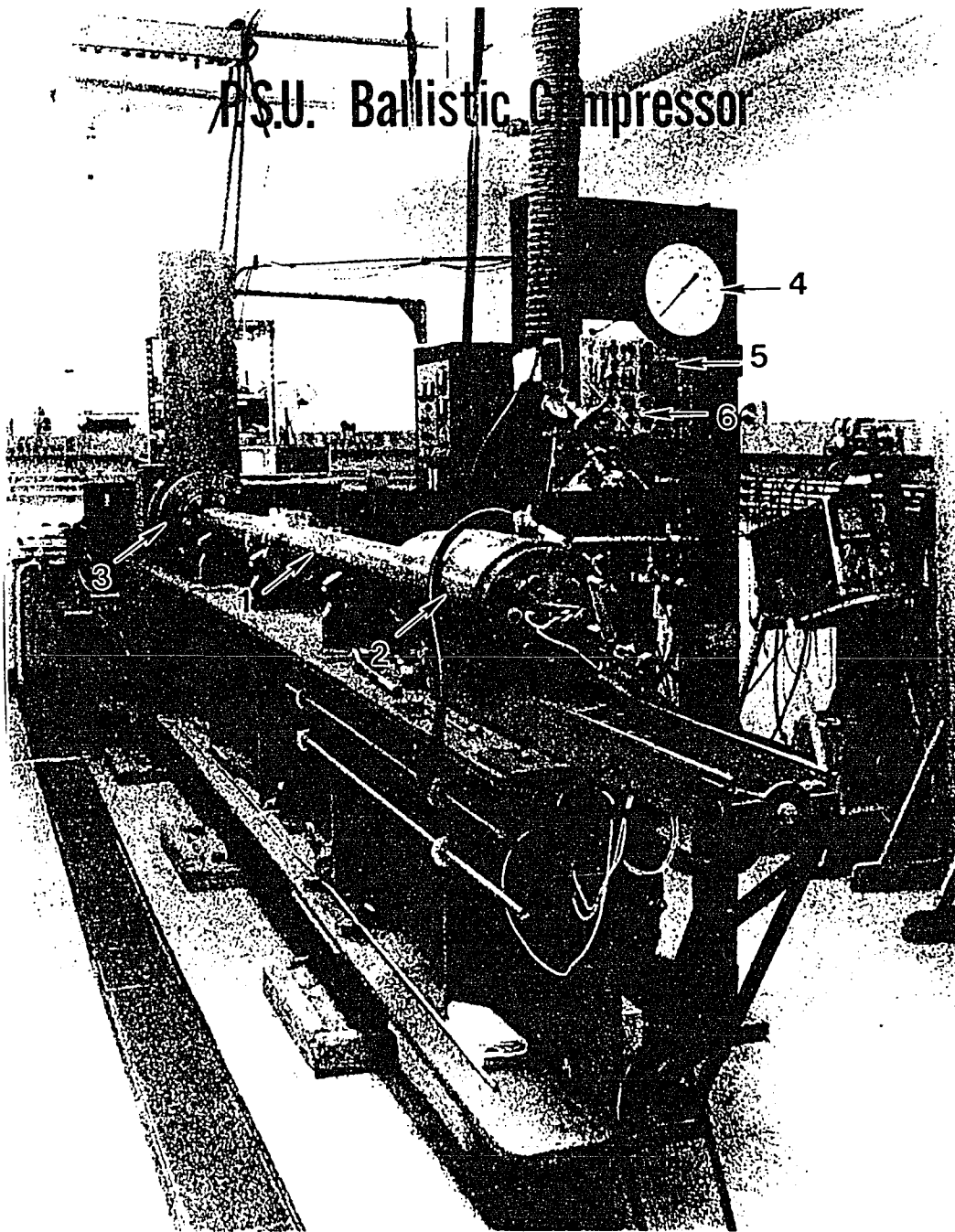


Figure 4. PSU ballistic compressor.  
1. compressor tube. 2. driving gas reservoir.  
3. high pressure compartment. 4. driving gas  
pressure gauge. 5. polaroid camera.  
6. oscilloscope.

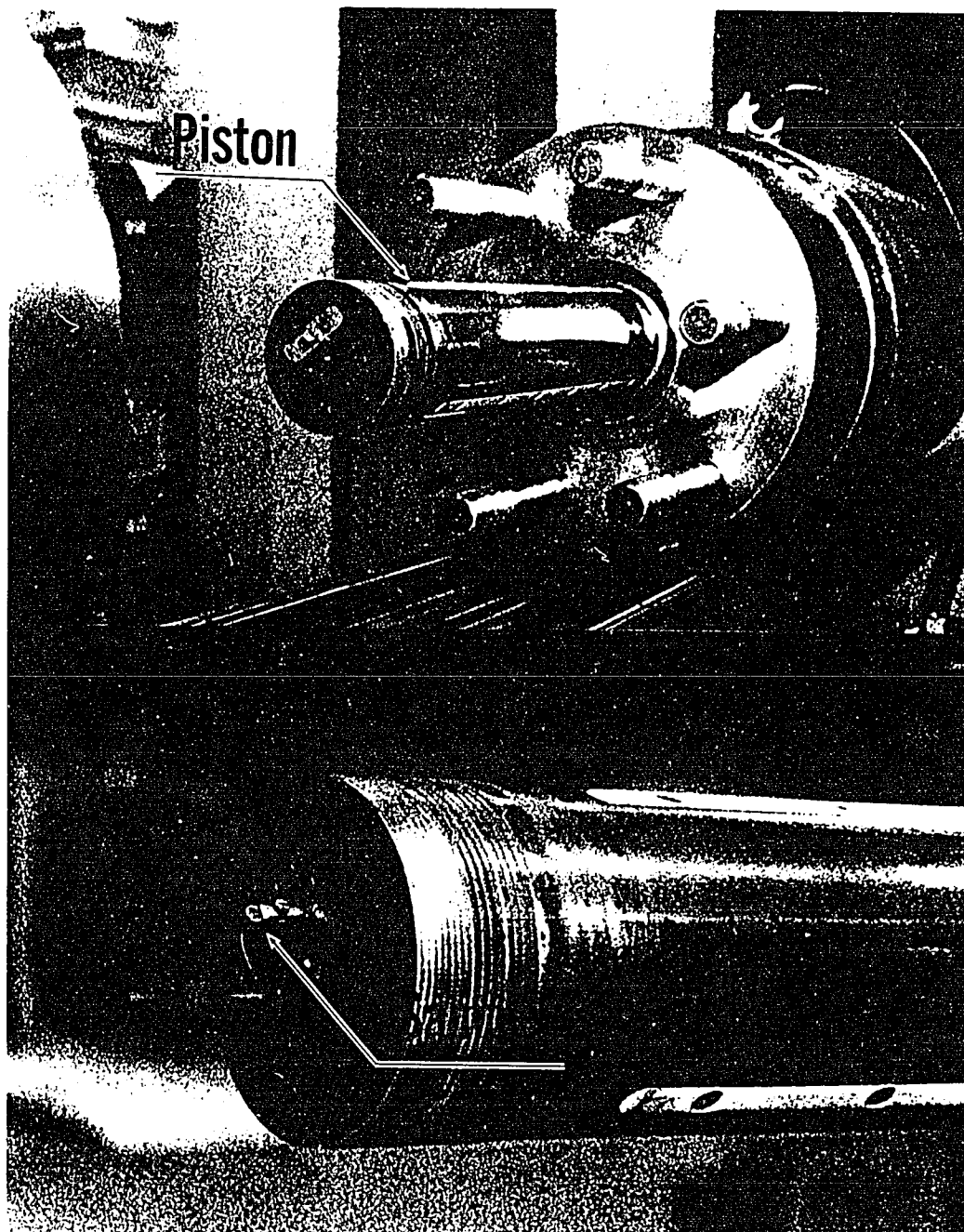


Figure 5. Free piston. (a) in pre-fired position in the gas reservoir. (b) a sample Cr thin film is mounted in front of the piston.

cooling. The entire exposure process including rapid increase and decrease of pressure and temperature was completed within a few tenths of a second. Cr thin films were mounted in front of the piston head and subjected to a non-equilibrium process in the BC. Their exposure to hot dense gases causes a modification of the crystal structure and the modification is then frozen in the cooling stroke in the BC, so that it can be observed at ambient. A detailed description and analysis of thermodynamical conditions in the BC, with a computer program for calculation of the test gas temperature (if the van der Waals constants are known), is available in [45].

## EXPOSURE

### Test Gas and Driving Gas

In this work, the driving gas is argon (99.999%) and the test gas is hydrogen (99.95%) provided by Air Products, Inc.

Before the test gas is admitted to the BC, argon is used to flush the BC 3 or 4 times to avoid any contamination by air.

### Thermodynamical Condition

Fill-in pressure. In order to get the highest peak condition usable for the present observation with the BC, several trials with different fill-in test gas pressure and driving Ar pressure have to be made until a small portion of

the mounted thin film is melted. Then the thermodynamic condition is kept the same for all subsequent exposures. A sample film may be exposed to hot, dense gas more than once to determine the reproducibility.

Peak Pressures. Peak pressure of the test gas is measured by a pressure transducer mounted on the side wall of the high pressure compartment. The output of the transducer is recorded on an oscilloscope with a polaroid camera. Figure 6 is an example of the oscillographs from which the peak pressures were obtained.

Peak Temperatures. Peak temperature is estimated from the fact that some portion of the Cr thin film was melted during exposure: the peak temperature of test gas must be higher than and close to the melting point of Cr--1875 °C. Inside the thin film, the peak temperatures are estimated to be 1700-1875 °C.

The cooling rates can be estimated from the oscillograph and peak temperature: the half-peak width in Figure 6 is about 2 ms which represents the cooling time from the peak to room temperature. The cooling rate =  $(1800-25)/(2 \times 10^{-3}) > 10^5$  °C/s.

Minimum Distance. The minimum volume of the test gas can be obtained by measuring the minimum distance of the piston head from the front inner end wall of the BC by a sliding pin mounted on the piston head.

The experimental thermodynamic conditions are listed

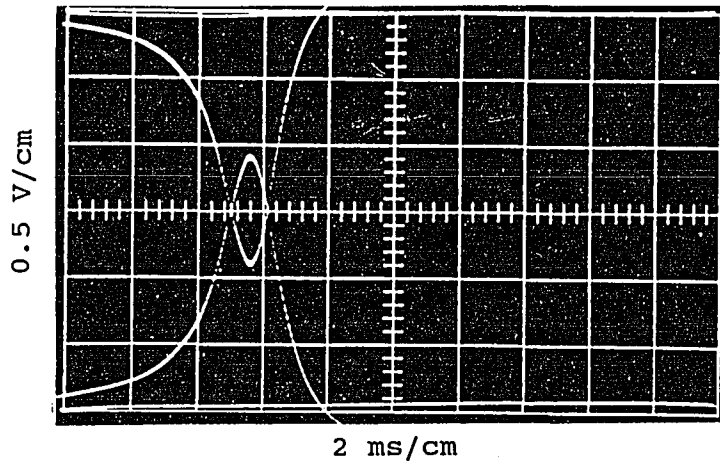


Figure 6. Pressure oscillograph of the test gas  $H_2$ . It shows the pressure signal from pressure transducer.

TABLE III

THERMODYNAMIC CONDITION OF EXPOSURE

Test gas	$H_2$
Fill-in pressure	-8 inHg
Driving Ar pressure	250 psi
Minimum distance	1.2 cm
Peak pressure	550 atm
Peak temperature of Cr film	1700-1875 °C

in TABLE III. The pressures are gauge pressures: negative sign means below one atmosphere.

After exposure, the sample grid is studied with TEM, SEM, EDS, and x-ray diffractometer. Hydrogen content of  $H_2$  exposed samples are spectroscopically tested by high-temperature vacuum extraction in a discharge tube.

## CHAPTER IV

### MICROGRAPHS AND DIFFRACTION PATTERNS BY TEM

#### INTRODUCTION

Particles are found on the Cr thin film after exposure to hydrogen in BC under TEM. Electron diffraction patterns show that the particles have a different crystal structure from the original bcc matrix. Patterns from three different zones are analyzed to obtain the crystallographic information. The electron microscopy work was done with Hitachi HU-125C transmission electron microscope at Portland State University.

#### THE GROWN PARTICLES

Particles are found on the Cr thin films after exposure to hot, dense H<sub>2</sub> in BC. The size of particles increases with each successive exposure. Figure 7 consists of a group of micrographs and diffraction patterns from (a) to (e), which show the effect of each exposure. After 4 or 5 time exposures, the films are full of grown particles. The orientation of grown particles seems to be correlated. Most of particles are elongated in nearly the  $\langle 100 \rangle$  directions.



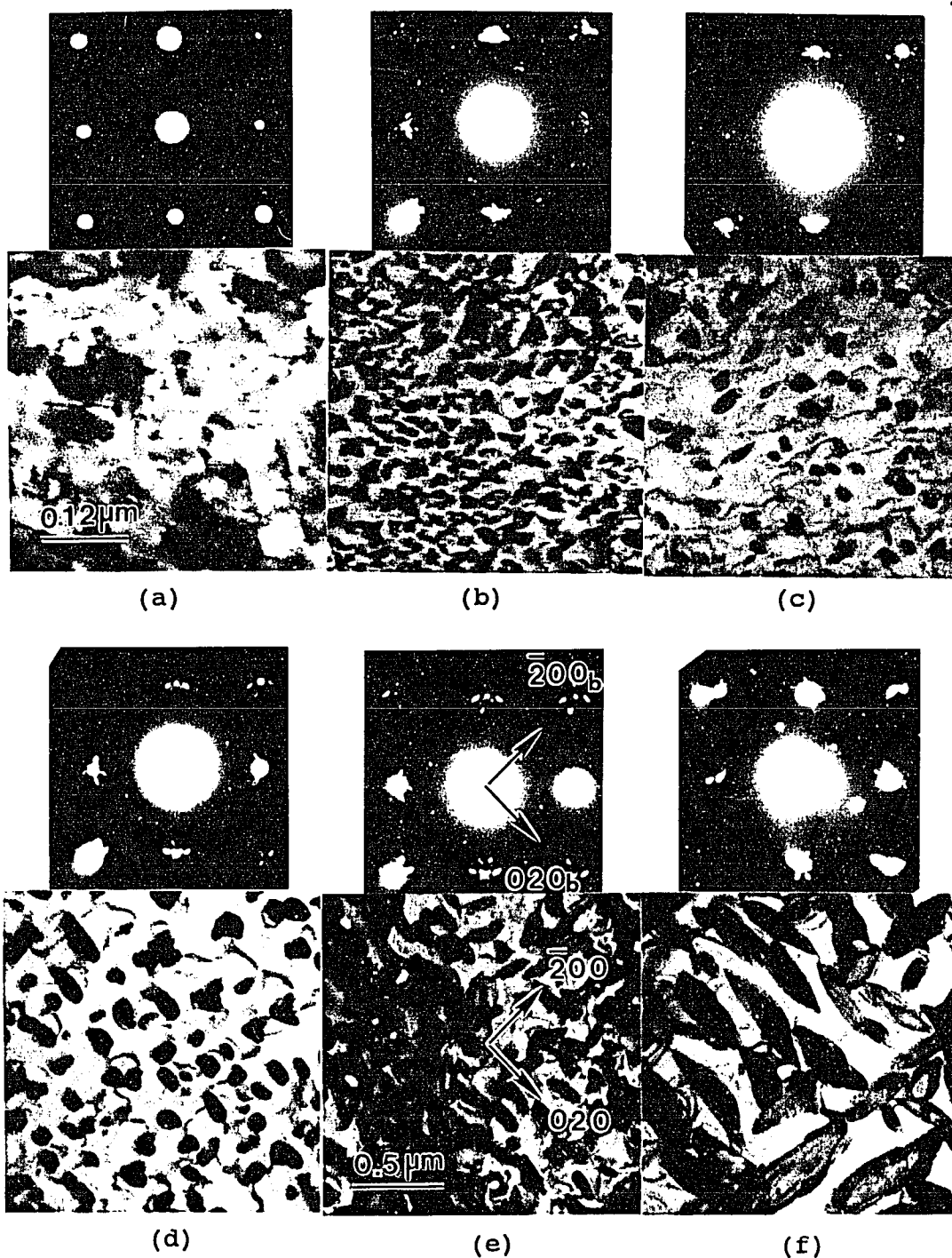


**Figure 7.** Cr thin film experienced five exposures to  $H_2$ . From (a) to (f), each shows the effect from 0 to five exposures. Note: the orientation shown in (e) applies to all photos; the scale bar in (e) applies to photos from (b) to (f).

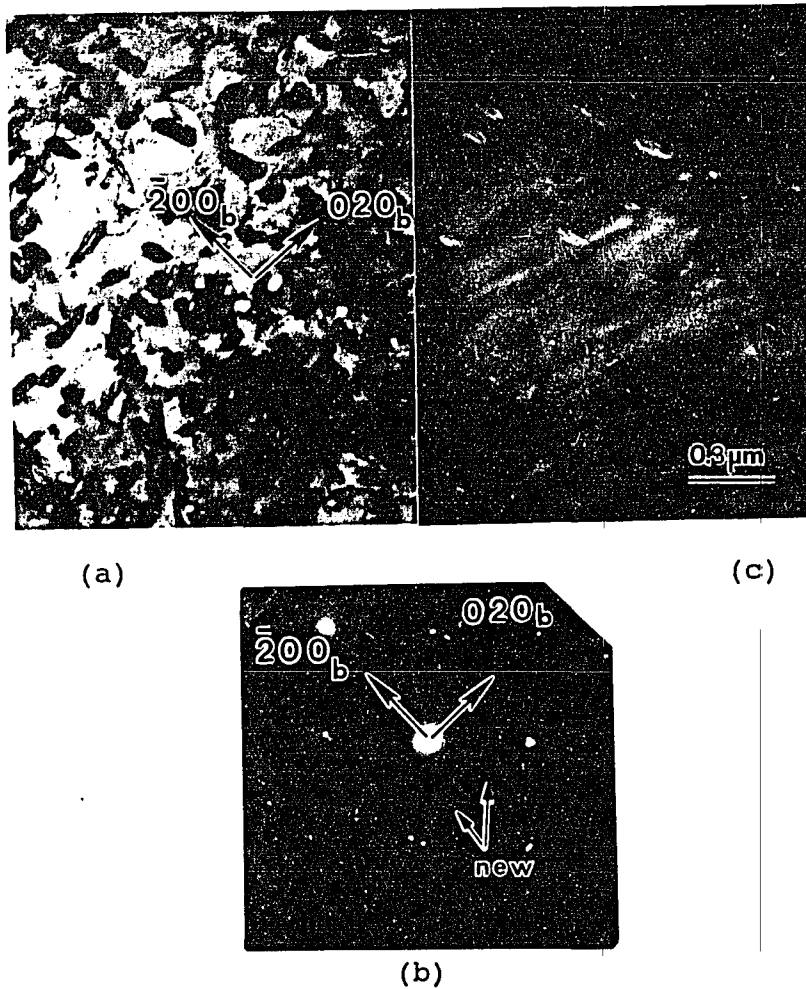


**Figure 8.** Dark field micrograph from new structure in a 4-time  $\text{H}_2$ -exposed Cr film. (a). bright field micrograph, (b). selected area diffraction pattern from precipitate particles shows a new pattern, (c). dark field image from one of those new spots, indicating precipitate particles have new structure.

The diffraction patterns show that the crystal structure of the film has been modified.

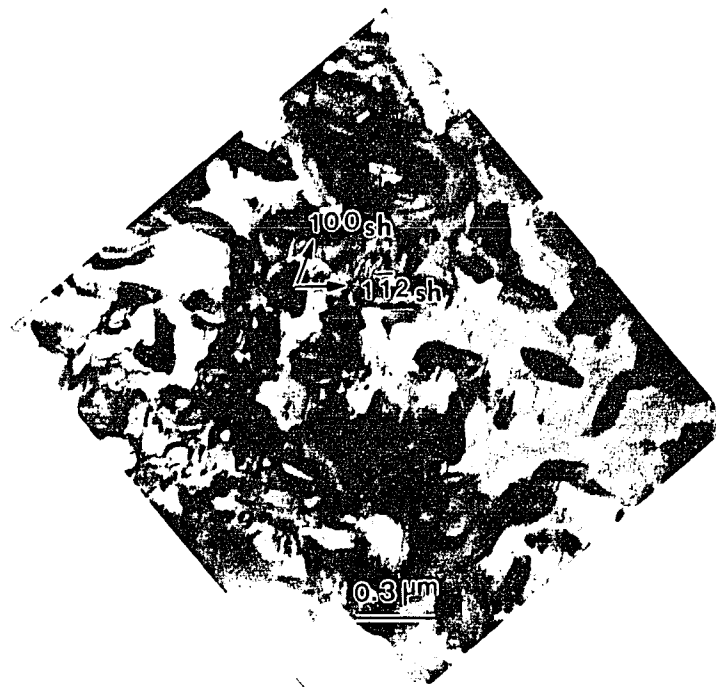
Figure 8 (a) shows the micrograph of a 4-times  $H_2$ -exposed chromium film. A typical particle size is about 150 nm x 50 nm. Figure 8 (b) shows the selected area diffraction pattern from a particle. Besides the original bcc pattern, a new pattern is superimposed, as indicated by the arrows. Figure 8 (c) shows the dark field image from one of the new diffraction spots. It indicates that new diffraction spots are from the particles and the surrounding matrix is still in the  $bcc [001]_b$  orientation.

There are also several holes appearing in this area, indicating that the local temperature of the thin film was close to the melting point of chromium. The smooth edges of the holes indicate that they were not due to mechanical damage, which usually leaves very sharp edges.

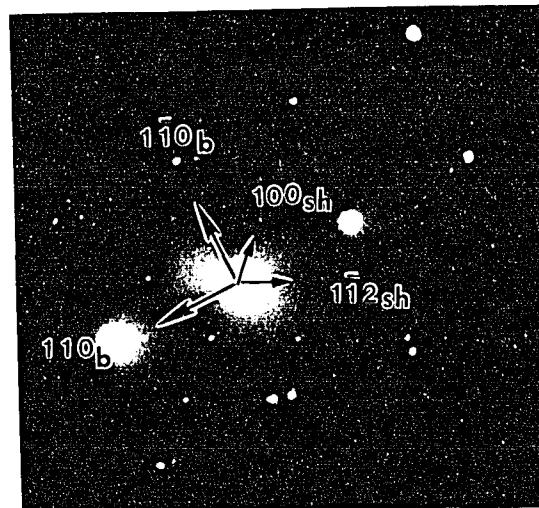
#### ELECTRON DIFFRACTION PATTERNS

##### Hexagonal Pattern in $[021]_{sh}$ Zone

The structure of the precipitated phase is identified as hexagonal. Figure 9 shows a micrograph (a) and selected area diffraction pattern (b) taken from one of the particles on the film of three exposures. Besides the original bcc pattern in the  $[001]_b$  zone, a pattern from a hexagonal structure is observed. Here a subscript 'b' indicates bcc and a subscript 'sh' is used to indicate the new hexagonal



(a)



(b)

**Figure 9.** Electron diffraction pattern in  $[021]_{sh}$  zone. (a). micrograph, (b). selected area diffraction pattern taken from one precipitate particle (the selected area is shown in (a)), the new superposed pattern indicates a hexagonal structure by comparing the standard electron diffraction pattern.



TABLE IV  
OBSERVED AND THEORETICAL d-SPACINGS AND ANGLES FROM  
FIGURE 10 (c)

(H K L)	d (obs.) (Å)	angle(obs) (deg.)	d (th.) (Å)	angle(th) (deg.)
(1 0 0)	4.16	0.0	4.131	0.0
(2 0 0)	2.06	0.6	2.065	0.0
(1 1 $\bar{2}$ )	2.10	40.3	2.096	40.5
(0 1 $\bar{2}$ )	3.03	68.3	3.008	68.5
( $\bar{1}$ 2 $\bar{4}$ )	1.61	90.5	1.615	90.0
( $\bar{1}$ 1 $\bar{2}$ )	3.06	111.1	3.008	111.4
( $\bar{1}$ 0 0)	4.16	178.9	4.131	180.0
( $\bar{2}$ 0 0)	2.06	179.7	2.065	180.0
( $\bar{3}$ 0 0)	1.35	179.4	1.377	180.0
( $\bar{1}$ $\bar{1}$ 2)	2.11	139.5	2.096	139.5
(0 $\bar{1}$ 2)	3.07	110.6	3.008	111.4
(1 $\bar{1}$ 2)	3.03	68.0	3.008	68.6

Note: Angles are measured relative to (100)<sub>sh</sub>. Theoretical lattice constant A=4.77Å and ratio C/A=1.84 (C=8.78Å).

structure. Compared with the standard hcp diffraction pattern of Figure 10 (a) [42], the new hexagonal structure appears in [021]<sub>sh</sub> zone. Both bcc and hexagonal pattern are indexed in a duplicated pattern Figure 10 (c). The spots constituting the bcc [001]<sub>b</sub> pattern are connected by dashed lines and indexed as (hkl)<sub>b</sub>. Spots constituting the hexagonal [021]<sub>sh</sub> pattern are connected by thin solid lines and indexed as (HKL)<sub>sh</sub>. Here again the capital letters are used for the new hexagonal indices. Because (H00)<sub>sh</sub> spots appear in this pattern, the lattice constant A for hexagonal

structure is rather precisely determined as  $4.77\text{\AA}$ . However, the ratio  $C/A$  is relatively hard to decide in this zone, because the angles between diffraction spots are not sensitive to this quantity. The determination of  $C/A$  as 1.84 is made after a diffraction pattern in which  $(00L)_{sh}$  spots are found. This is shown in  $[210]_{sh}$  zone pattern later.

TABLE IV lists the observed d-spacings and relative angles measured from  $(100)_{sh}$  compared with theoretical prediction of hexagonal structure with  $A$  equal to  $4.77\text{\AA}$  and ratio of  $C/A$  equal to 1.84. A computer program [46] is used in processing the diffraction pattern together with electronic camera device. The detailed procedure of processing an electron diffraction pattern is put in APPENDIX B.

#### Hexagonal Pattern in $[\bar{2}23]_{sh}$ Zone by Bending Thin Film

The tilt angle of the Hitachi HU-125C is limited to  $\pm 10^\circ$ , so that tilting does not work well for obtaining another symmetrical diffraction pattern. The nearest zone axis of a densely populated reciprocal planes is  $[031]_{sh}$  which makes an angle of  $11.1^\circ$  from  $[021]_{sh}$  zone axis by calculation. That means even if the sample films have been tilted by a maximum angle  $10^\circ$ , still at least there is a deviation by  $1.1^\circ$ . The  $1.1^\circ$  deviation from the exact zone axis is too large to keep the diffraction pattern. This is

proved by the following fact: the diffraction patterns from zone  $[021]_{sh}$  disappears when the tilt angle is set only  $40'$  in two opposite directions, leaving strong bcc diffraction only, as shown in Figure 11. To overcome this obstacle, the method of bending the sample or selecting a large aperture is employed.

Figure 12 (a) and (b) show the micrograph and diffraction pattern from a particle on a bent sample of four exposures. Again there are many holes indicating the exposure temperature is close to the Cr melting point. Due to the bending, the chromium thin film is locally tilted at a large angle so that diffraction from a new zone axis is obtained. The standard pattern of  $[\bar{2}23]$  zone for hexagonal indexed in 4-axis system from [43], is shown in Figure 12 (c). Indices for the planes in 3-axis system can be easily obtained by removing the third figure in the indices in 4-axis system. The triangle spots represent the diffraction on the first order Ewald plane which should be ignored at this moment. This fits the observed pattern Figure 12 (b). The angle between  $[\bar{2}23]_{sh}$  and  $[021]_{sh}$  is  $24.2^\circ$  by calculation. This indicated the thin film had been locally tilted  $24.2^\circ$  by bending. The diffraction from bcc matrix Cr shows with less intensity a  $[\bar{1}13]_b$  zone diffraction pattern compared with the standard diffraction pattern of bcc in  $[\bar{1}13]$  zone (Figure 13 (a)). The angle between  $[\bar{1}13]_b$  zone axis and  $[001]_b$  zone axis is  $25.2^\circ$  by calculation. So the tilt angle



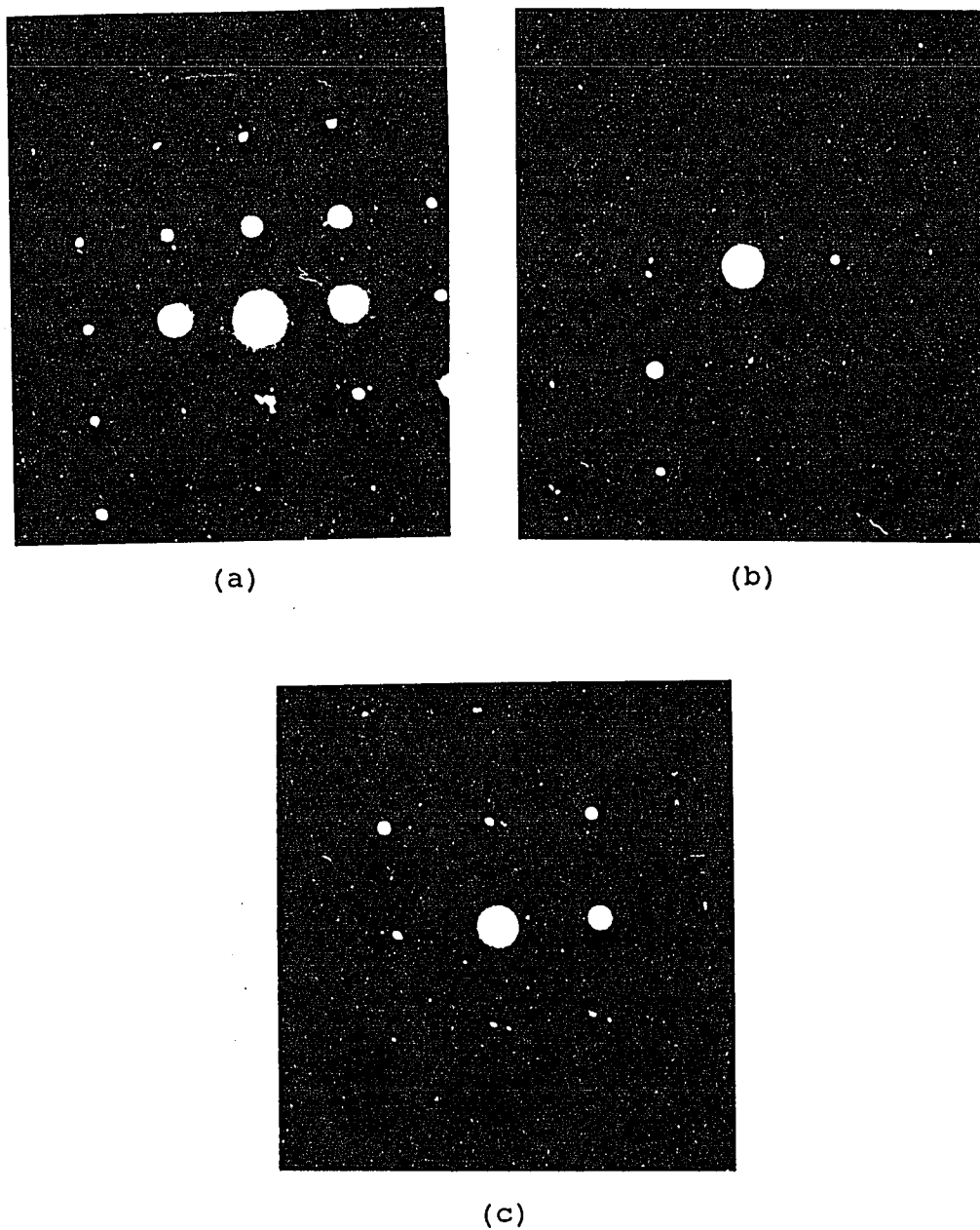
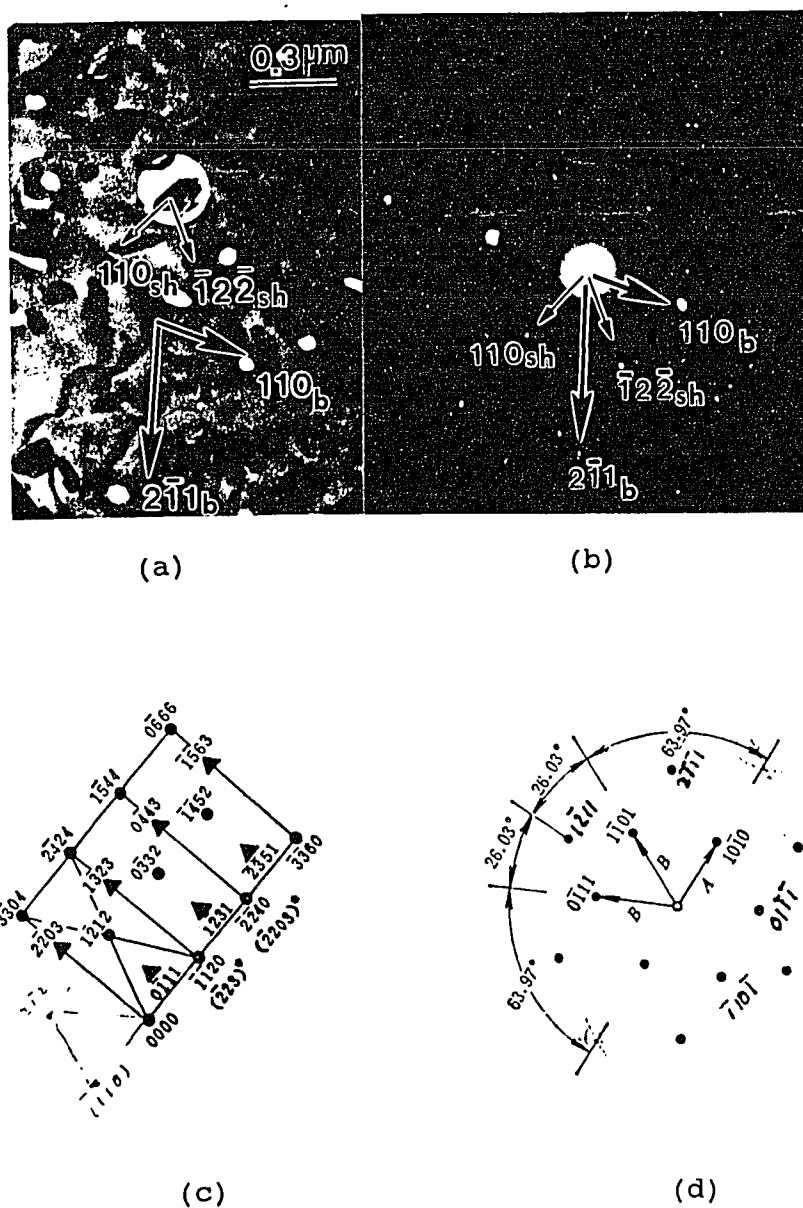


Figure 11. Diffractions at tilt angle  $40'$ .  
(a). tilt angle at  $40'$  and rotation angle at  $0^\circ$ ; (b). tilt angle at  $40'$  and rotation angle at  $180^\circ$ ; (c). before tilt and rotation.



**Figure 12.** Electron diffraction pattern in  $[\bar{2}23]_{sh}$  zone. (a) micrograph, (b) selected area electron diffraction pattern from one precipitate (selected area is shown in (a)) in  $[\bar{2}23]_{sh}$  and  $[011]_{hcp}$  zones with weak  $[\bar{1}13]_b$  pattern from matrix by comparing with standard patterns. (c) standard hcp pattern in  $[\bar{2}23]_{sh}$  zone, (d) standard hcp pattern in  $[011]$  zone.



24.2° can only produce weak  $[\bar{1}13]$  zone diffraction pattern from the matrix. TABLE V lists the observed and theoretical d-spacings and relative angles for the hexagonal structure from this pattern. The detailed calculation following the above procedure is put in APPENDIX B.

TABLE V  
OBSERVED AND THEORETICAL d-SPACINGS AND ANGLES FROM  
FIGURE 13 (b)

(H K L)	d (obs.) (Å)	angle(obs) (deg.)	d (th.) (Å)	angle(th) (deg.)
$(\bar{1} \bar{1} 0)$	2.34	0.0	2.385	0.0
$(1 1 0)$	2.36	180.0	2.385	180.0
$(\bar{1} 2 \bar{2})$	2.07	115.2	2.096	116.1
$(1 \bar{2} 2)$	2.09	63.2	2.096	63.9
$(3 0 2)$	1.28	146.5	1.314	145.7
$(\bar{3} 0 \bar{2})$	1.31	33.6	1.314	34.3
$(\bar{3} 3 \bar{4})$	1.17	89.6	1.166	90.0
$(\bar{2} 4 \bar{4})$	1.05	115.8	1.048	116.1
$(0 3 \bar{2})$	1.30	145.2	1.314	145.7
$(2 2 0)$	1.16	179.4	1.192	180.0

Note: Angles are measured relative to  $(110)_{sh}$ . Theoretical lattice constant  $A=4.77\text{Å}$  and ratio  $C/A=1.84$  ( $C=8.78\text{Å}$ ).

#### Hexagonal Pattern in $[210]_{sh}$ Zone by Large Selected Aperture

Figure 14 and 15 show a micrograph and diffraction pattern taken with a larger aperture which includes a film area about  $2.3 \mu\text{m}^2$ . This area is densely populated with precipitate particles after four exposures. The total area of particles in the aperture is about 1/4-1/3 of total area

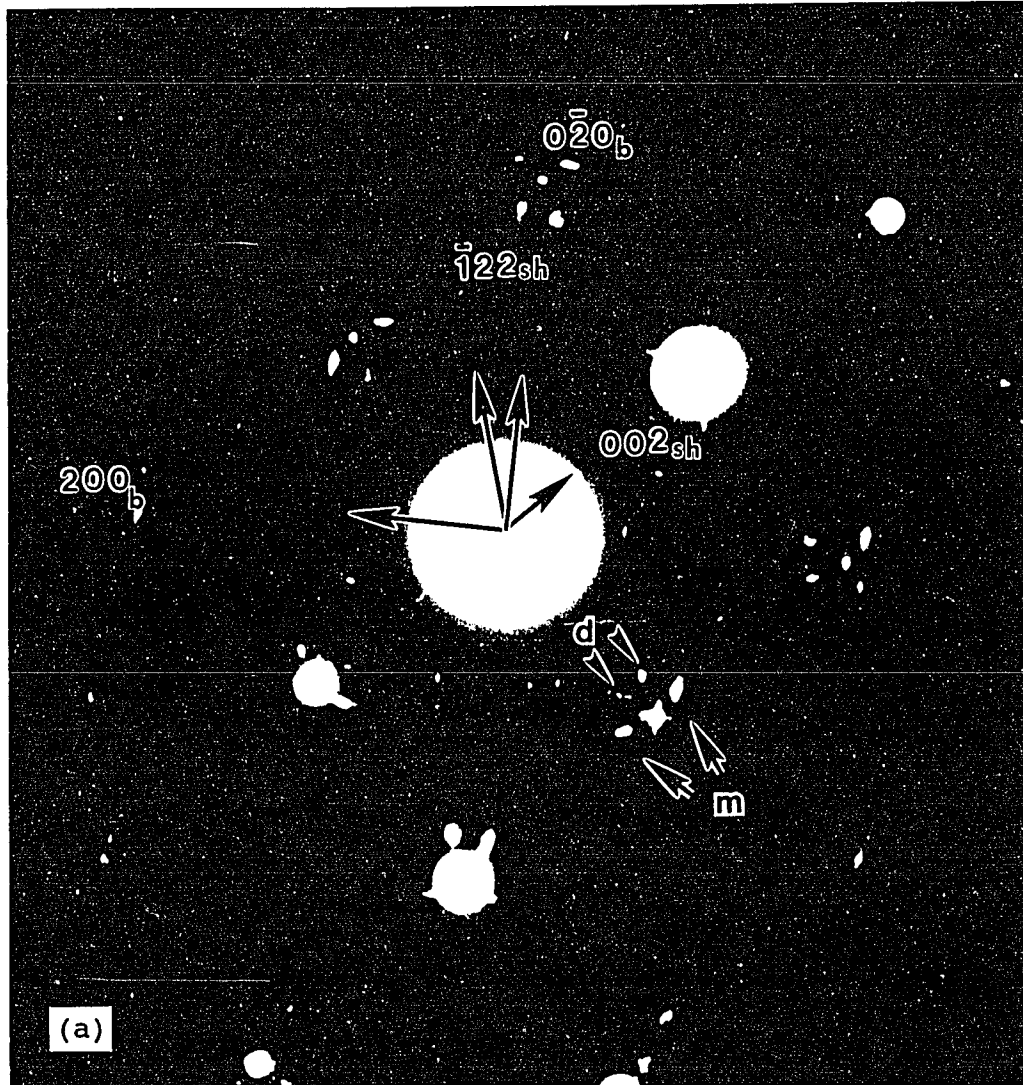


**Figure 14.** Electron diffraction pattern from an area densely populated with precipitate particles. (The selected area is shown in **Figure 15**.) Note: 1. more than one hexagonal pattern in  $\langle 021 \rangle_{sh}$  because more than one particle are included in selected area. 2. patterns in  $\langle 021 \rangle_{sh}$  can be obtained by rotating one single  $[021]_{sh}$  pattern  $90^\circ$  each time and/or taking mirror pattern with one of  $\{110\}_b$  as mirror plane. 3. satellite spots by double diffraction. 4. intensity difference between hcp and superhexagonal spots. 5. weak  $[210]_{sh}$  zone pattern.



Figure 15. Micrograph of Figure 14. It shows the selected area is densely populated with precipitate particles after four exposures.

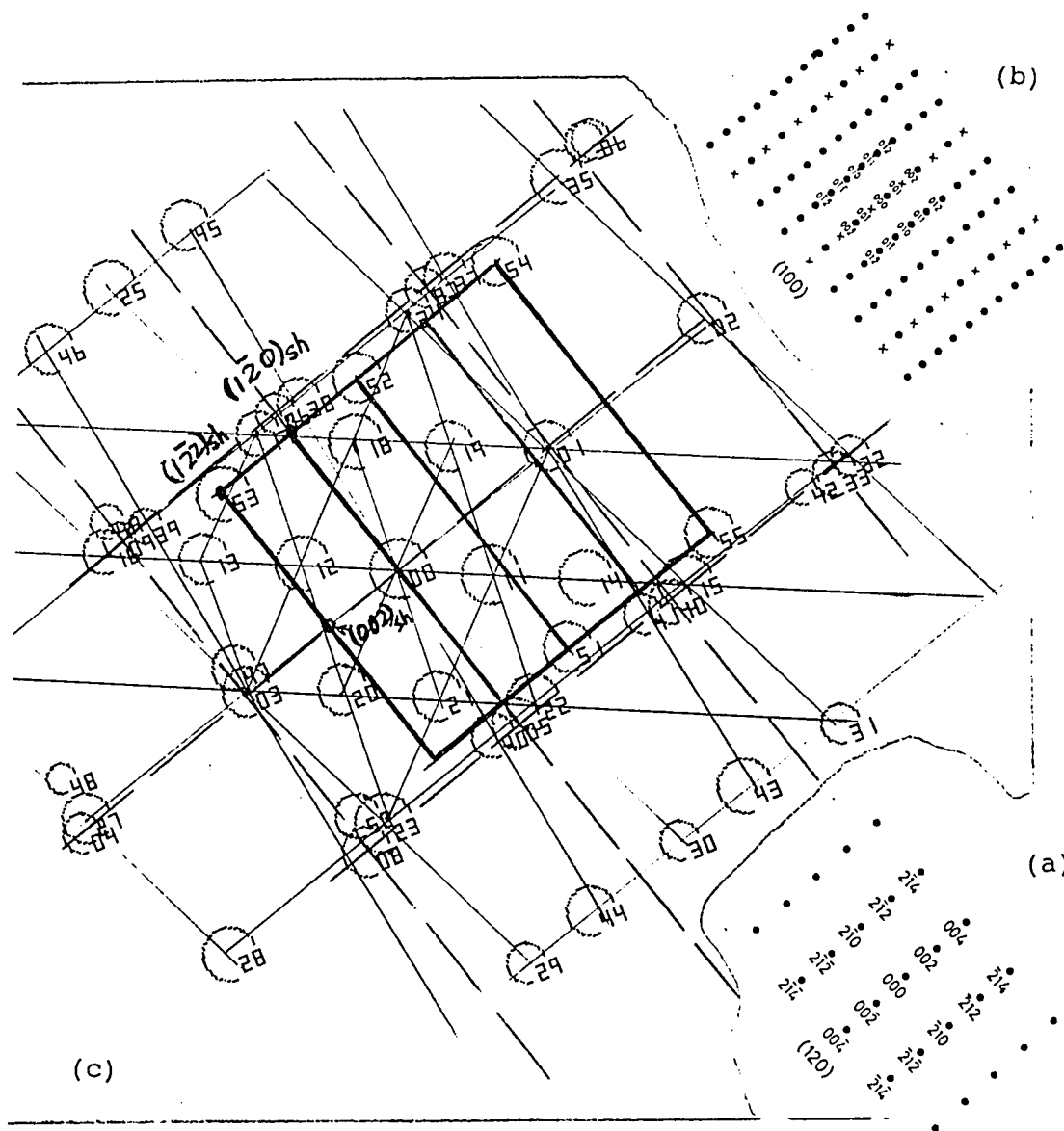


**Figure 16.** Analysis of electron diffraction pattern in  $[210]_{sh}$  zone. (a). standard hcp electron diffraction pattern in  $[210]$ , (b). standard hcp pattern  $[100]$  zone, (c). duplicated and indexed pattern of electron diffraction pattern Figure 14. Note: 1. bcc structure in  $[001]_b$  zone, spots connected by broken lines. 2. hexagonal structure in  $\langle 021 \rangle_{sh}$  zone, spots connected by thin solid lines and designated by  $(HKL)_{sh}$ . 3. hcp structure in  $\langle 011 \rangle_{hcp}$  zone, spots connected by thin solid lines also. 4. hexagonal spots in  $[210]_{sh}$  zone, connected by heavy solid lines.

included in the aperture. The diffraction pattern shows that the bcc matrix is in the  $[001]_b$  zone, the same as in Figure 9.

Compared with Figure 9, a very weak  $[210]_{sh}$  zone pattern is superposed in this photograph. From spots  $(002)_{sh}$  and  $(1\bar{2}0)_{sh}$  in this zone pattern, the lattice constant ratio is evaluated as 1.84. TABLE VI lists the calculated d-spacings and angles compared with observed values in this zone pattern. The detail of the evaluation of the C/A ratio is put in APPENDIX B.

TABLE VI  
OBSERVED AND THEORETICAL d-SPACINGS AND ANGLES FROM  
FIGURE 16 (c)

( H K L)	d (obs.) (Å)	angle(obs) (deg.)	d (th.) (Å)	angle(th) (deg.)
(0 0 2)	4.40	0.0	4.388	0.0
(1 $\bar{2}$ 0)	2.38	90.0	2.385	90.0
(1 $\bar{2}$ 2)	2.09	61.6	2.096	61.5

Note: Angles are measured relative to  $(002)_{sh}$ . Theoretical lattice constant  $A=4.77\text{Å}$  and ratio  $C/A=1.84$  ( $C=8.78\text{Å}$ ).

Notice that since the angle between  $[021]_{sh}$  zone axis and  $[210]_{sh}$  zone axis in hexagonal is  $90^\circ$  by calculation, the appearance of a new zone pattern indicates some crystals are orientated as if they were rotated  $90^\circ$  from  $[021]_{sh}$  to  $[210]_{sh}$  zone. Since the bcc matrix has three equivalent orientations (one  $\perp$  and two  $\parallel$  the film surface), the superhexagonal has the possibility of different



orientations. Crystals grown in one of the the other two equivalent orientation then contribute the  $[210]_{sh}$  pattern. From  $\{H00\}_{sh}$  spots in Figure 10 (c),  $[210]_{sh}$  (in direction of spot  $(001)_{sh}$ ) deviates from  $[010]_b$  by about  $3^\circ$ . If the area of the thin film in the selected area is exactly in the  $[001]_b$  zone, the  $[210]_{sh}$  pattern would not appear. The thin film must have buckled, so that locally an angle about  $3^\circ$  is obtained. If the selected area is not large enough, the  $[210]_{sh}$  pattern will not be superimposed on the  $[021]_{sh}$  pattern. The superimposed weak  $[210]_{sh}$  zone pattern is seen only when a large selector aperture is used.

Compared with Figure 9 (b), more than one hexagonal pattern in  $\langle 021 \rangle_{sh}$  appear in Figure 14, because many particles are included in the aperture area and they have different orientations. These orientations have definite crystallographic correlations. Since the bcc structure has four-fold rotational symmetry in the  $[001]_b$  zone, hexagonal structure will also have four different orientations, each rotated  $90^\circ$  to each other along the  $\langle 012 \rangle$  zone axis.

The  $\{110\}_b$  planes in Figure 14 seem to be mirror planes of different hexagonal orientations and one pair of mirror spots are indicated by 'm' arrows. This indicates that hexagonal structures have some definite orientations relative to bcc structure of the matrix upon which they grow. If two particles grown from different sides of the thin film are observed, the mirror diffraction pattern will

be obtained. The mirror pattern from the opposite beam direction is the same pattern on the negative when it is seen from the other side.

Compared with Figure 9 (b), there are satellite spots due to double diffraction indicated by 'd' arrows in Figure 14. When a larger selector area including more particles in it is used for the electron diffraction, the chance to have double diffraction is larger. The double diffraction is also responsible for the appearance of elongation of diffraction spots, because  $\{110\}_b$  is close to  $\{\bar{2}1\bar{2}\}_{sh}$ , making the double diffraction spots close to the first diffraction spots.

Compared with Figure 9 (b), the intensity differences among hexagonal spots is evident in Figure 14. The stronger ones comes from hcp structure, as will be discussed in next chapter. This indicates hcp and superhexagonal could exist separately, though have particular relation in their orientations.

#### SUMMARY

From analyses of electron diffraction patterns, the lattice constants of a new hexagonal structure have been determined as  $A=4.77\text{\AA}$ ,  $C/A=1.84$  ( $C=8.78\text{\AA}$ ).

## CHAPTER V

### SUPERHEXAGONAL STRUCTURE

#### INTRODUCTION

Both electrolytic [11] and direct synthesis [18] methods produce the hcp structure of chromium hydride CrH, with chromium atoms forming hcp shell and hydrogen atoms occupying octahedral interstices [47]. The lattice constant  $a=2.72\text{\AA}$  and ratio  $c/a=1.625$  [11]. In the present work, the observed hexagonal lattice constant  $A=4.77\text{\AA}$  and ratio  $C/A=1.84$ . To distinguish the two hexagonal structures, superhexagonal lattice is used to refer the new structure since it has a larger crystallographic period and 'sh' for short has been used for indexing diffraction pattern in the last section. In this chapter, the superhexagonal structure, its relation to hcp, and its relative orientation to the bcc Cr matrix are described.

#### SUPERHEXAGONAL STRUCTURE

##### Volume Of Unit Cell

For comparison, the unit cell volume of hexagonal structure is calculated according to observed lattice constants. It is a little larger than that of 6 hcp unit cells of CrH. TABLE VII lists the lattice constants and

TABLE VII

LATTICE CONSTANTS AND UNIT CELL VOLUMES FOR Cr, CrH  
AND SUPERHEXAGONAL CHROMIUM HYDRIDE

	lattice const. (Å)	unit cell volume (Å <sup>3</sup> )	vol. per 2 Cr atoms (Å <sup>3</sup> )
bcc (Cr)	a=2.884	24.0	24.0
hcp (CrH)	a=2.72 c=4.42	28.3	28.3
s.hex. (CrH <sub>7</sub> )	A=4.77 C=8.78	172.9	28.8
undist. hcp accord. to sh	a=2.75 c=4.39	28.8	28.8

unit cell volumes for bcc Cr, hcp CrH and the superhexagonal structure. The volume per two chromium atoms in superhexagonal is larger than that of hcp by 0.5 Å<sup>3</sup>. This indicates that the expansion in volume may be caused by more hydrogen entering interstitial vacancies, which in turn distorted the hcp into a superhexagonal.

According to above analysis, the superhexagonal model is constructed in two steps: first, it consists of 6 hcp units, with 12 chromium atoms in its unit cell; then, inside the superhexagonal unit some chromium atoms are shifted by trapping more than 12 hydrogen atoms so that the symmetry of original hcp would be destroyed, but still retain the hexagonal structure in the larger lattice constants. Since the shift or distortion in the second step involves the knowledgement of the hydrogen locations which is not clear

at present time, it is left for future study. The way of constructing the superhexagonal structure from hcp is depicted in Figure 17. It consists of five close-packed layers with the same layers on top and at bottom, packing as ...ABABA... arrangement. The black balls belong to layer A and white balls belong to layer B respectively. Hydrogen atoms occupying the interstitial positions, are not drawn here. An alternative arrangement ...ABACA... is also possible, where there is a faulted packing layer C. In the layer C, the atoms occupy the positions where the atoms in B layer are uniformly shifted by one atomic distance. The other choice ...ABCBA... made no difference from ...ABACA.... Both ...ABABA... and ...ABACA... arrangements could produce the electron diffraction patterns in the last chapter, if inside the unit cell there is a distortion.

#### Description of Superhexagonal with Two Coordinate System

A conceived undistorted hexagonal close-packed, based on superhexagonal structure, is not the same as hcp CrH. Since it has some advantages to show the relationships between superhexagonal and hcp CrH here, and between superhexagonal and bcc Cr in the next chapter, its coordinate system is also used as well as that of superhexagonal. One way to define the relationship of two coordinate systems has been used in Chapter IV and is depicted in Figure 17 (b). The superhexagonal unit cell is formed by  $A$ ,  $B$ ,  $C$ , and hcp unit cell by  $a$ ,  $b$ ,  $c$ . The miller

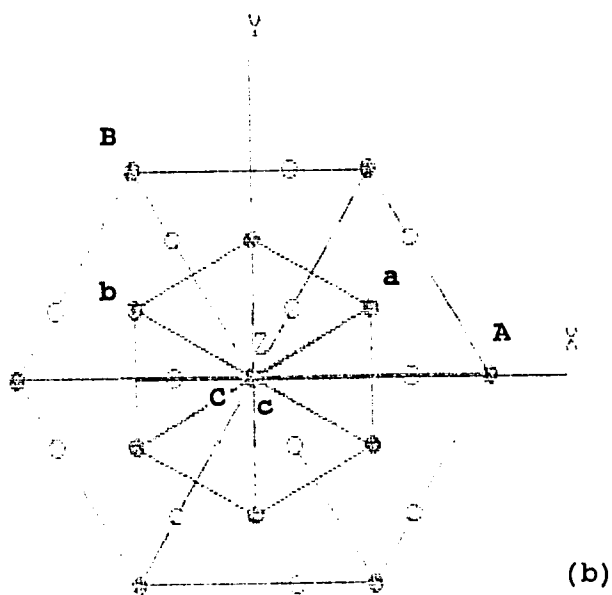
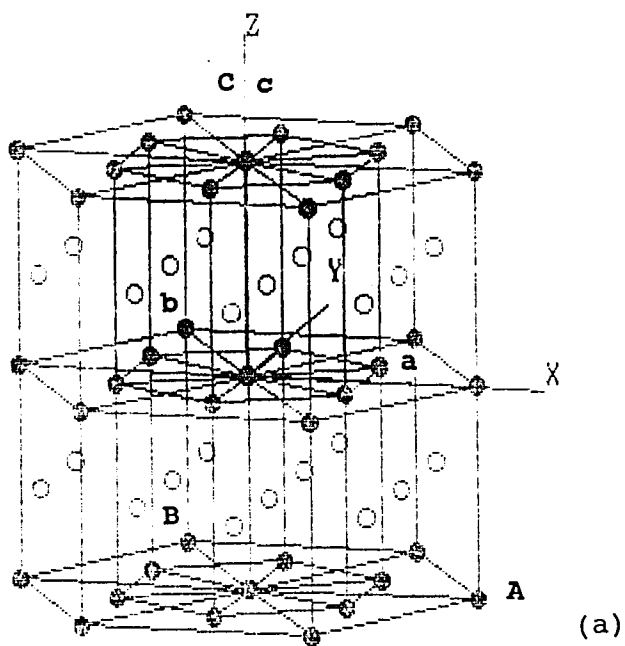


Figure 17. Model of the undistorted superhexagonal structure. The superhexagonal unit cell is formed by A, B, C, and the hcp unit cell by a, b, c.

indices in two coordinate systems are related by the following matrix transformations. For plane indices, the transformations are:

$$\begin{pmatrix} H \\ K \\ L \end{pmatrix} = \begin{pmatrix} 1 & -1 & 0 \\ 1 & 2 & 0 \\ 0 & 0 & 2 \end{pmatrix} \begin{pmatrix} h \\ k \\ l \end{pmatrix}$$

and

$$\begin{pmatrix} h \\ k \\ l \end{pmatrix} = \begin{pmatrix} 2/3 & 1/3 & 0 \\ -1/3 & 1/3 & 0 \\ 0 & 0 & 1/2 \end{pmatrix} \begin{pmatrix} H \\ K \\ L \end{pmatrix}$$

For direction indices, the transformations are:

$$\begin{bmatrix} U \\ V \\ W \end{bmatrix} = \begin{pmatrix} 2/3 & -1/3 & 0 \\ 1/3 & 1/3 & 0 \\ 0 & 0 & 1/2 \end{pmatrix} \begin{bmatrix} u \\ v \\ w \end{bmatrix}$$

and

$$\begin{bmatrix} u \\ v \\ w \end{bmatrix} = \begin{pmatrix} 1 & 1 & 0 \\ -1 & 2 & 0 \\ 0 & 0 & 2 \end{pmatrix} \begin{bmatrix} U \\ V \\ W \end{bmatrix}$$

The capital indices designate superhexagonal and the lower case indices designate undistorted hcp. The lattice constant  $a$  and ratio  $c/a$  for an undistorted hcp are:

$$a = 2/3 \times A \times \sin 60^\circ = 2.75 \text{ \AA}$$

$$c = 0.5 \times C = 4.388 \text{ \AA}$$

$$c/a = (1/2 \times C)/a = (C/A) \times 3/4/\sin 60^\circ = 1.59$$

These results have been put in the last row of TABLE VII.

TABLE VIII

DIFFRACTION PATTERN INDICES IN BOTH SH AND HCP COORDINATES

zone axis		plane	
$[U V W]_{sh}$	$[u v w]_{hcp}$	$(H K L)_{sh}$	$(h k l)_{hcp}$
$[0 2 1]_{sh}$	$[1 2 1]_{hcp}$	$(2 \bar{1} 2)_{sh}$	$(1 \bar{1} 1)_{hcp}$
		$(3 0 0)_{sh}$	$(2 \bar{1} 0)_{hcp}$
		$(1 1 \bar{2})_{sh}$	$(1 0 \bar{1})_{hcp}$
		$(\bar{1} 2 \bar{4})_{sh}$	$(0 1 \bar{2})_{hcp}$
$[\bar{2} 2 3]_{sh}$	$[0 1 1]_{hcp}$	$(2 \bar{1} 2)_{sh}$	$(1 \bar{1} 1)_{hcp}$
		$(1 1 0)_{sh}$	$(1 0 0)_{hcp}$
		$(\bar{1} 2 \bar{2})_{sh}$	$(0 1 \bar{1})_{hcp}$
		$(0 3 \bar{2})_{sh}$	$(1 1 \bar{1})_{hcp}^*$
		$(3 0 2)_{sh}$	$(2 \bar{1} 1)_{hcp}^*$
		$(2 2 0)_{sh}$	$(2 0 0)_{hcp}$
		$(\bar{2} 4 \bar{4})_{sh}$	$(0 2 \bar{2})_{hcp}$
		$(\bar{3} 3 \bar{4})_{sh}$	$(\bar{1} 2 \bar{2})_{hcp}$
$[2 1 0]_{sh}$	$[1 0 0]_{hcp}$	$(0 0 2)_{sh}$	$(0 0 1)_{hcp}^*$
		$(1 \bar{2} 0)_{sh}$	$(0 \bar{1} 0)_{hcp}$
		$(1 \bar{2} 2)_{sh}$	$(0 \bar{1} 1)_{hcp}$

\*: forbidden spot.

Compared with the hcp lattice constants of CrH, where  $a=2.72\text{\AA}$ ,  $c=4.42\text{\AA}$ , and  $c/a=1.625$ , the superhexagonal is stretched in each close-packed plane and compressed between those planes.

Planes and directions have been indexed in both coordinate systems in diffraction patterns in Chapter IV. Their indices are now listed in TABLE VIII. Lower case 'hcp' has been used for the undistorted hcp structure. The



zone axes  $[021]_{sh}$ ,  $[\bar{2}23]_{sh}$  and  $[210]_{sh}$  in superhexagonal transform into  $[121]_{hcp}$ ,  $[011]_{hcp}$  and  $[100]_{hcp}$  of undistorted hcp respectively. For comparison, standard diffraction patterns of these zone directions are shown in Figure 10 (b), Figure 12 (d) and Figure 16 (b) respectively. In Figure 9 (b), Figure 10 (a) and (b), removing superhexagonal spots  $(100)_{sh}$ ,  $(200)_{sh}$ ,  $(01\bar{2})_{sh}$ ,  $(\bar{1}1\bar{2})_{sh}$  and their negatives would transform  $[021]_{sh}$  zone pattern into  $[121]_{hcp}$  zone pattern. This indicates that if the distortion inside the superhexagonal were removed, the hcp would be recovered, and  $[021]_{sh}$  zone axis pattern would turn into  $[121]_{hcp}$  pattern. From the coordinate systems in Figure 17, one can see these two corresponding directions,  $[021]_{sh}$  and  $[121]_{hcp}$ , are indeed parallel.

In Figure 12 (a), (c), (d) and Figure 13 (b), the appearance of spots  $(2\bar{1}1)_{hcp}$ ,  $(\bar{2}1\bar{1})_{hcp}$  and  $(11\bar{1})_{hcp}$  which have corresponding indices  $(302)_{sh}$ ,  $(\bar{3}0\bar{2})_{sh}$  and  $(03\bar{2})_{sh}$  respectively, indicates the diffraction pattern of Figure 12 (a) is from superhexagonal with zone axis  $[\bar{2}23]_{sh}$ , instead of hcp since these spots are forbidden spots in hcp diffraction. If the distortion inside superhexagonal were removed so that hcp were recovered, the  $[\bar{2}23]_{sh}$  zone axis pattern would turn into  $[011]_{hcp}$  pattern. From Figure 13, one can see again, these two corresponding directions,  $[011]_{hcp}$  and  $[\bar{2}23]_{sh}$ , are indeed parallel.

In Figure 14 and Figure 16, the appearance of  $(001)_{hcp}$ ,

which has corresponding index  $(002)_{sh}$ , again indicated the diffraction pattern Figure 14 is from superhexagonal with zone axis  $[210]_{sh}$  instead of hcp, since  $(001)_{hcp}$  is a forbidden spot in hcp diffraction. If the distortion were removed so that hcp were recovered, the  $[210]_{sh}$  zone axis pattern would turn into  $[100]_{hcp}$  pattern. From the coordinate system in Figure 17, one can see again, these two directions are indeed parallel.

#### ORIENTATION OF SUPERHEXAGONAL IN BCC MATRIX

From electron diffraction patterns, another important relationship obtained is the relative orientation of superhexagonal to the bcc matrix. This is determined from a pair of parallel zone axes, one from superhexagonal and the other from bcc, and from a pair of nearly parallel planes, one from superhexagonal and the other from bcc. From Figure 9, since the superhexagonal  $[021]_{sh}$  zone axis pattern is superposed on the bcc Cr matrix  $[001]_b$  zone axis pattern, one relation can be expressed as these two zones in parallel:

$$[021]_{sh} \quad // \quad [001]_b,$$

or by hcp coordinate indices:

$$[121]_{hcp} \quad // \quad [001]_b \quad (5-1)$$

Here the undistorted hcp coordinate system is used again to

facilitate the explanation of the relative orientation. Also, from the electron diffraction pattern in Figure 9, one can see approximately:

$$(2\bar{1}2)_{sh} \quad // \quad (\bar{1}\bar{1}0)_b$$

or

$$(1\bar{1}1)_{hcp} \quad // \quad (\bar{1}\bar{1}0)_b \quad (5-2)$$

By these relations, the relative orientation of superhexagonal to the bcc matrix is determined uniquely.

The diffraction patterns in Figure 12 and Figure 14 are indexed so that they are all consistent with Figure 9. As described in Chapter IV, the angle between zone axis  $[\bar{2}23]_{sh}$  for superhexagonal pattern (or  $[011]_{hcp}$ ) in Figure 12 and zone axis  $[021]_{sh}$  (or  $[121]_{hcp}$ ) in Figure 9 is  $24.2^\circ$ ; for bcc Cr matrix in Figure 12, tilting the same angle  $24.2^\circ$  can only produce a weak  $[\bar{1}13]_b$  pattern. The zone axis  $[210]_{sh}$  (or  $[100]_{hcp}$ ) in Figure 14 is perpendicular to  $[021]_{sh}$  (or  $[121]_{hcp}$ ) in Figure 9, and the zone axis  $[0\bar{1}0]_b$  in Figure 14 is also perpendicular to zone axis  $[001]_b$  in Figure 9. It was noted in Chapter IV, that  $[210]_{sh}$  (or  $[100]_{hcp}$ ) is the normal of  $(300)_{sh}$  (or  $(2\bar{1}0)_{hcp}$ ) planes, and  $[0\bar{1}0]_b$  is the normal of  $(0\bar{1}0)_b$  planes. So the diffraction spots  $(300)_{sh}$  and  $(0\bar{2}0)_b$  in Figure 9 present the angle  $3^\circ$  between the two zone axes  $[210]_{sh}$  (or  $[100]_{hcp}$ ) and  $[0\bar{1}0]_b$ .

Figure 18 shows the views of relative orientation of

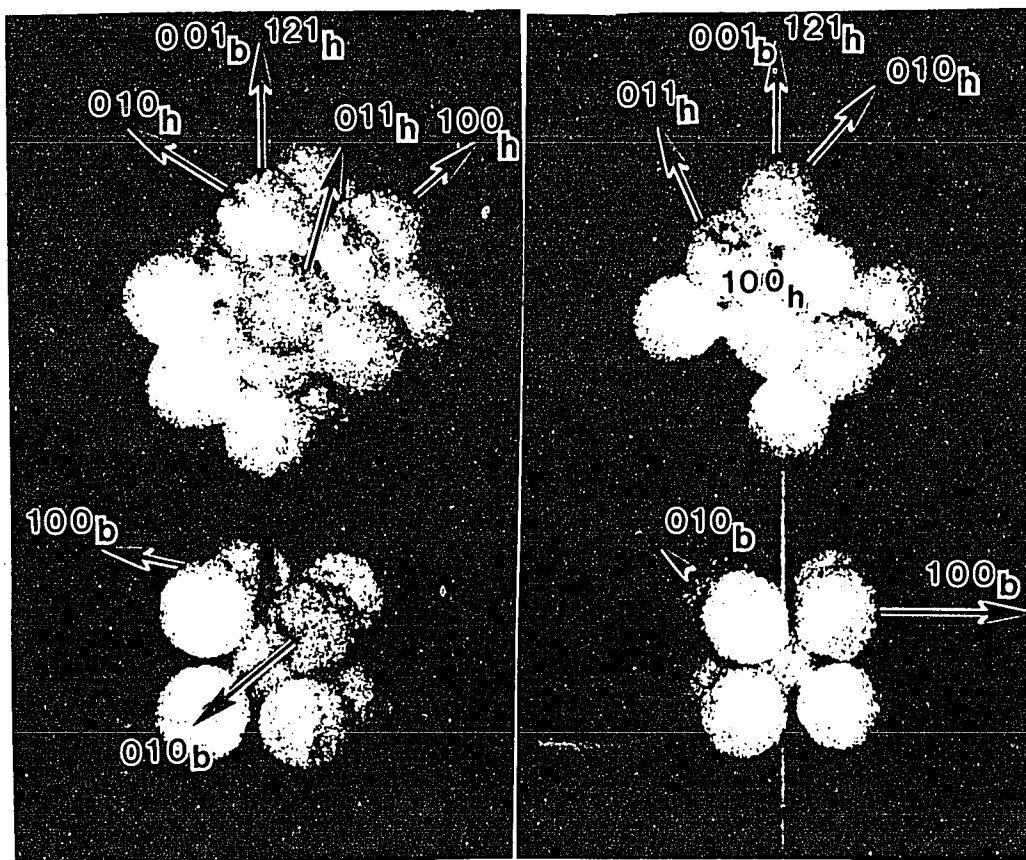


Figure 18. Hcp and bcc models show their relative orientation.

hcp and bcc unit cell models according to relation (5-2). The indices in the picture are all for directions, the brackets are omitted to save space. The 'hcp' has been shortened into 'h' to save space too. One can see from the picture,  $[121]_{\text{hcp}} // [001]_{\text{b}}$ , and approximately,  $[011]_{\text{hcp}} // [\bar{1}13]_{\text{b}}$  and  $[[100]_{\text{hcp}} // [0\bar{1}0]_{\text{b}}$ . These are the zone axes of electron diffraction patterns in Figure 9, Figure 12, and Figure 14.

## PHASE TRANSFORMATION FROM BCC TO SUPERHEXAGONAL

It is interesting to note from the view in  $[0\bar{1}0]_b$  direction in Figure 18 (b) that the close-packed layers of hexagonal are nearly parallel to  $(10\bar{1})_b$  planes. This indicates that one group of the most densely populated  $\{110\}_b$  planes in bcc transform into close-packed planes in hexagonal when the phase transition occurred.

When a new phase grows from the matrix, the atom rearrangement must tend to least displacement and least stress among atoms. Figure 19 illustrates the correspondence for the bcc to hcp transformation. It is similar to the case of the martensitic transformation of lithium, titanium, and zirconium from bcc to hcp structure [48]. The orientation of the two structures is exactly expressed by relation (5-2). Those zone axes of diffraction patterns in Figure 9, Figure 12, and Figure 14 are shown as arrows in Figure 19. Two parallel shadowed planes are  $(1\bar{1}1)_{hcp}$  and  $(\bar{1}\bar{1}0)_b$  respectively. The actual hcp crystal has to be slightly distorted from this arrangement during transformation so that only  $[121]_{hcp}$  and  $[001]_b$  keep parallel. The two shadowed planes are not strictly parallel to each other even though the parallel condition is still used approximately in (5-2), neither are the directions  $[100]_{hcp}$  and  $[0\bar{1}0]_b$  exactly parallel as has been shown in Figure 9.

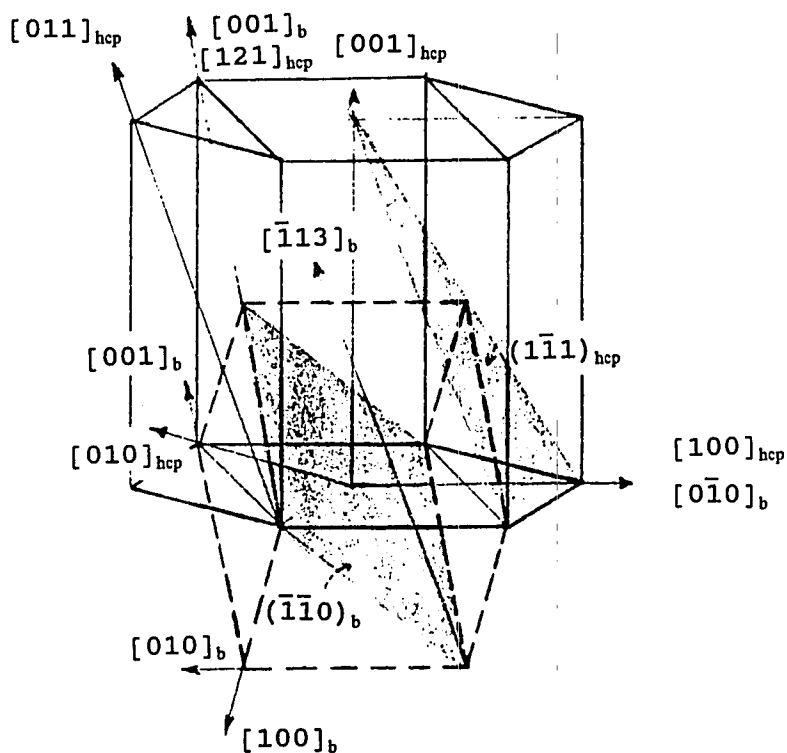


Figure 19. Phase transformation correspondence for bcc to hcp. The relative orientation of two structures is expressed by relation (5-1) and (5-2).

#### SUMMARY

The superhexagonal structure model is established based on electron diffraction analysis. With the help of a conceived undistorted hcp coordinate system, the geometric relation and difference between superhexagonal and real hcp CrH become obvious. The superhexagonal structure could be a distortion of real hcp CrH due to additional hydrogen trapped in its structure. Except for the hydrogen involved, the phase transformation from bcc to hexagonal is similar to the bcc to hcp transformation of pure metals such as lithium, titanium, and zirconium.

## CHAPTER VI

### STABILITY OF SUPERHEXAGONAL STRUCTURE

The superhexagonal structure in the Cr films exposed to hydrogen in the BC is observed to be quite stable in air at atmospheric pressure and room temperature. Figure 20 shows a hydrogen exposed Cr thin film sample 79 days after exposure. The particles and superhexagonal diffraction pattern still exist.

On the other hand, the superhexagonal structure is observed to be unstable under electron beam bombardment.

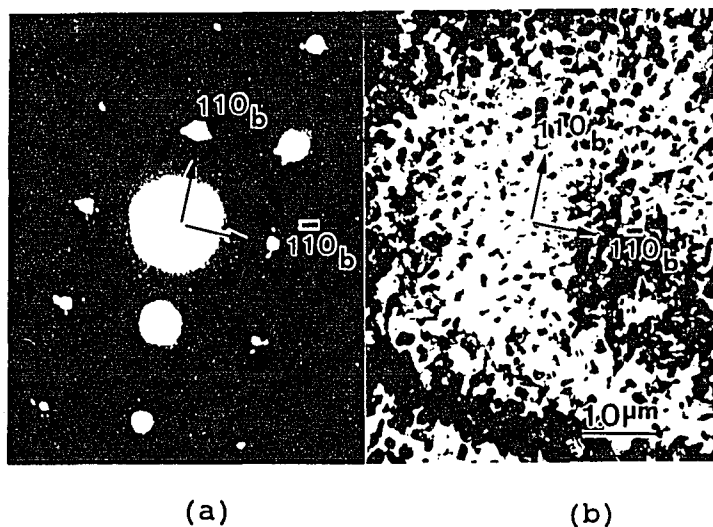


Figure 20. Cr thin film 79 days after exposures to  $\text{H}_2$ . (a), selected area electron diffraction pattern and (b), micrograph show the superhexagonal structure is quite stable at atmospheric pressure and room temperature.

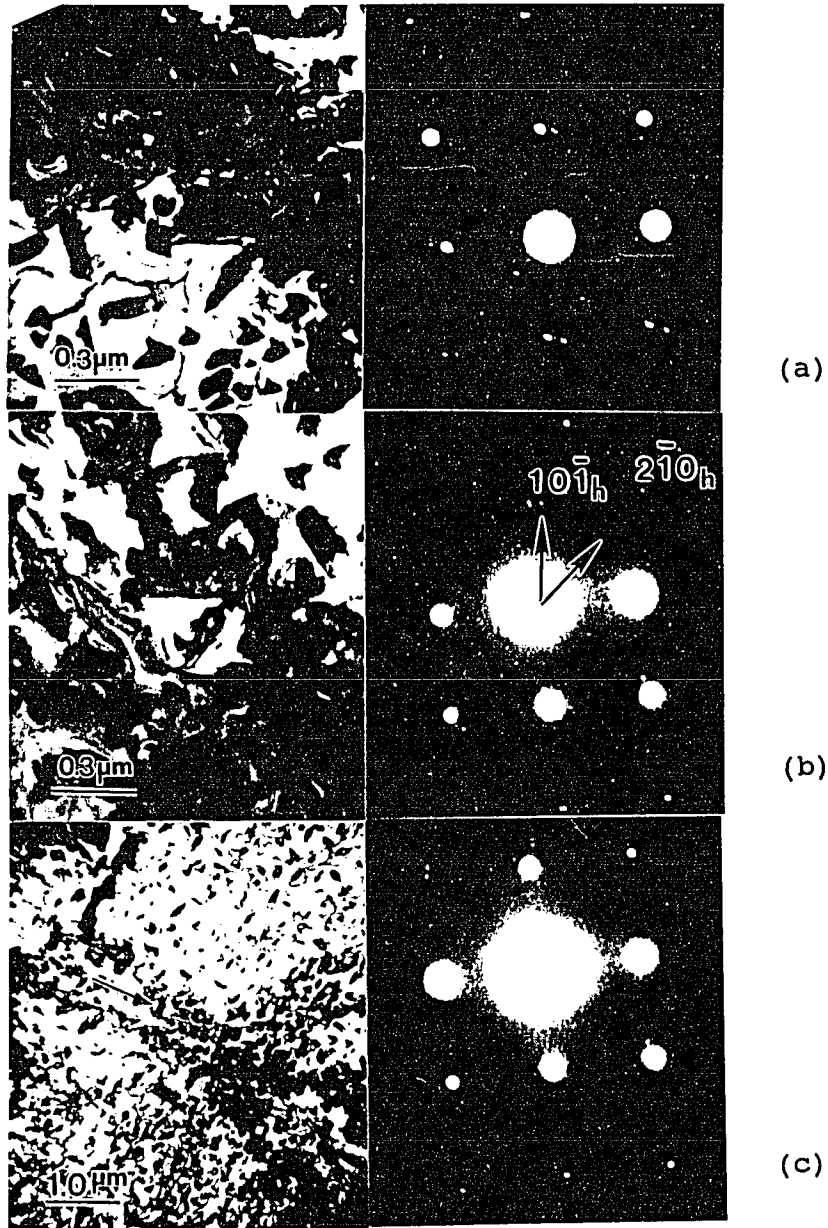


Figure 21. Superhexagonal structure bombarded by electron beam. (a) before and (b) after 75 keV electron beam bombardment for about 2 hrs.. Only strong superhexagonal spots in  $[021]_{sh}$  zone left and form hcp  $[121]_{hcp}$  zone pattern. (c) from larger area, diffraction pattern shows the superhexagonal spots are too weak to be seen.



Figure 21 shows diffraction patterns and corresponding micrographs before and after being bombarded by the electron beam of 75 keV (about  $0.8 \mu\text{A}/\mu\text{m}^2$ ) for about 2 hours. The superhexagonal diffraction pattern became weaker and weaker with time under the beam. Finally, some of the spots disappeared, leaving relatively strong spots remaining. The boundary of particles became less sharp. The instability of the superhexagonal could be caused by the release of extra hydrogen and the removal of distortion. The remaining strong spots in (b) themselves form a new pattern in  $[121]_{\text{hcp}}$  zone. This proves the relationship of superhexagonal and hcp as discussed in Chapter V.

The hcp structure was also unstable under the electron beam. Eventually all of the hexagonal pattern disappeared, leaving the bcc pattern behind. Figure 21 (c) shows the diffraction pattern with a large selected area. The superhexagonal spots are too weak to be seen and the hcp spots have become very weak. Compared with Figure 9, the structure produced by exposure to hydrogen has been removed by the electron beam bombardment.

It is common that metal hydrides release hydrogen when heated. As expected, the metal recovers the original structure of the pure metal. Here, the fact that the superhexagonal structure disappears and leaves only bcc structure suggests that decomposition of chromium hydride occurred in the area bombarded by the electron beam.

## CHAPTER VII

### HYDROGEN DETECTION AND CHEMICAL COMPOSITION ESTIMATION

#### INTRODUCTION

Quantitative determination of hydrogen content in small particles is rather difficult.

In this chapter, a qualitative detection of hydrogen content is performed by high temperature vacuum extraction and observation of the hydrogen spectrum in a discharge tube. Then some arguments are presented concerning the particles and why they are thought to be chromium hydride.

#### HIGH TEMPERATURE VACUUM EXTRACTION

A vertical discharge tube was made of glass tubing with 4-mm inner diameter. The tubing has glass-metal seals on both ends. In the middle, a horizontal tube is connected so that the tube is made into a T shape. Through the opening of horizontal tube, the H<sub>2</sub>-exposed samples are put in and the discharge tube is pumped to a vacuum about 10<sup>-4</sup> torr. Before the horizontal portion of the tube was torch sealed, it was degassed by heating at 270°C for half an hour, while the portion close to sample grids was kept at room temperature. After sealing, a potential of 5 kv is applied

to the discharge tube and no discharging occurs. After the portion of discharge tube with sample grids inside is heated to 250 °C for about 20 minutes, the discharge tube gives off weak purple light.

The spectrum is recorded by a spectrograph and compared with spectrum from a standard hydrogen tube. In Figure 22, spectrum (a) is taken from the hydrogen tube. This shows the first five lines of the Balmer series. The spectrum (b) is taken from the experimental tube. A very weak line in the position of the first Balmer line (wavelength  $\lambda=6562.8$  Å) was observed, indicating that hydrogen gas was in the tube due to decomposition of chromium hydride caused by heating the sample films. Other Balmer lines were too weak to be observed, even though the exposure time was as long as 40 minutes.

The structure was also investigated by TEM diffraction. Selected area diffraction patterns before and after this experiment are shown in Figure 23. After this experiment, the superhexagonal pattern became much weaker relative to the bcc pattern than before. The reversion of superhexagonal structure to bcc upon heating is expected for the same reason as bombardment by the electron beam--the decomposition of chromium hydride released hydrogen and recovered the pure metal Cr bcc structure.

It is interesting to compare this experiment with experiments by [13] and [49]. At atmospheric pressure and

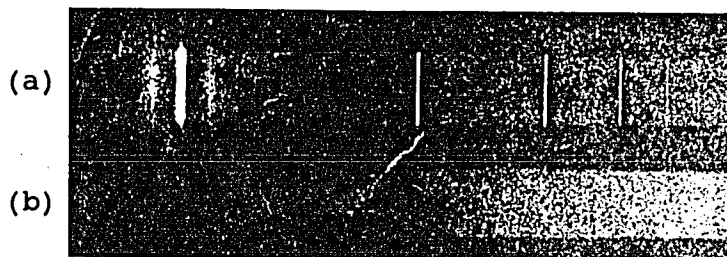


Figure 22. Spectra from discharge tubes. (a) from a hydrogen tube, (b) from the discharge tube in this experiment.

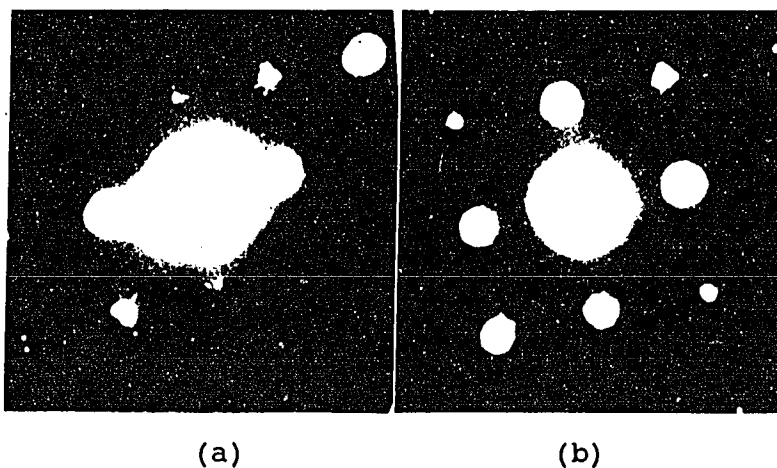


Figure 23. Structure reversion. A H<sub>2</sub>-exposed Cr thin film, (a), before, (b), after the high-temperature vacuum extraction experiment.

170 °C, the hcp chromium hydride made by electroplating started to transform in 10 minutes and completely changed into bcc in 50 minutes [13]. In a vacuum of  $10^3$  torr, it took only 2 minutes at 100 °C, and 20 minutes at 50 °C, for hcp chromium hydride to complete the transition [49]. The direct-synthesis chromium hydride [18] last only 3-4 hours at room temperature and under atmospheric pressure.

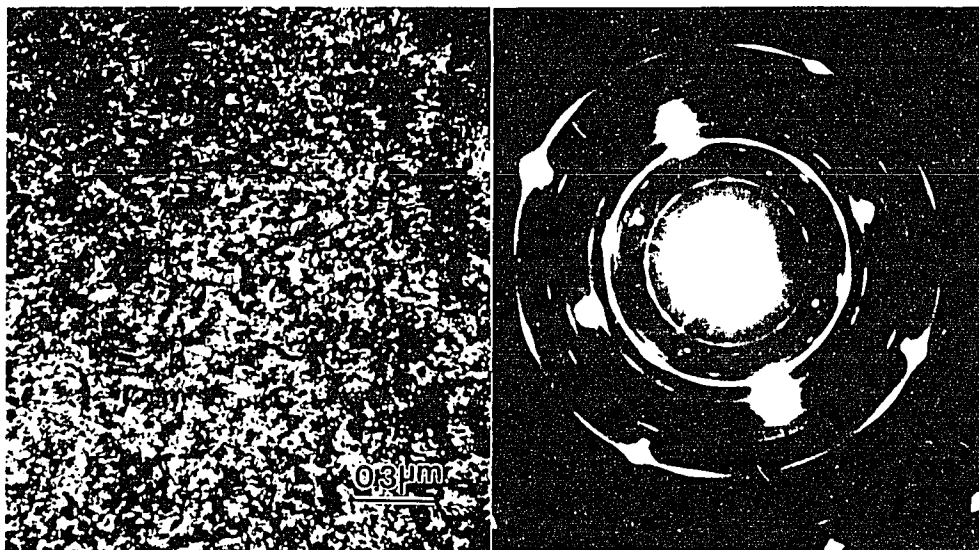
Obviously, the superhexagonal chromium hydride has the highest thermal stability. It requires a higher temperature to release hydrogen and recover the bcc structure.

#### CHEMICAL COMPOSITION ESTIMATION BY OTHER METHODS

##### Impurities in Hydrogen

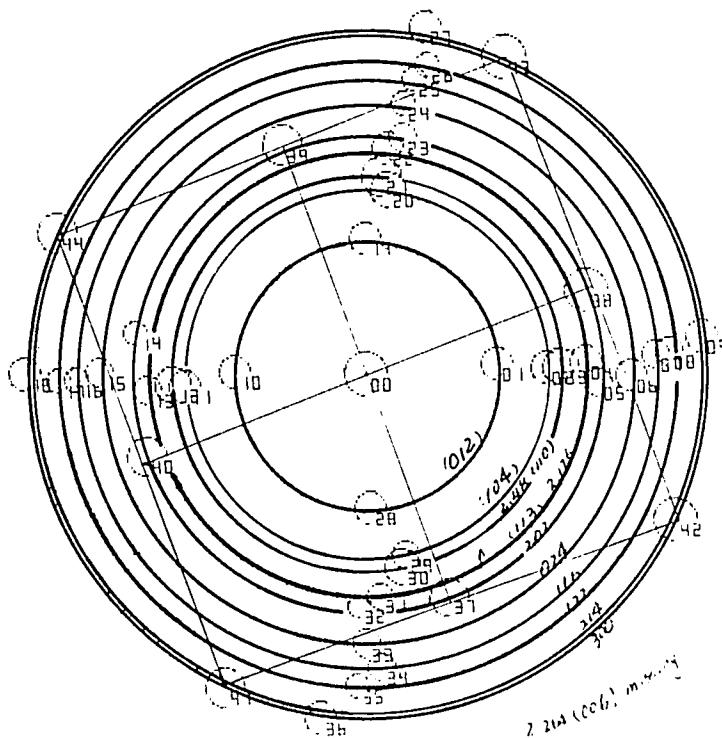
Hydrogen used in the experiment has a purity of 99.95%. It is almost impossible for any impurity less than 0.05% in hydrogen to produce large numbers of particles as shown in Figure 7. If air accidentally leaked into the BC during the filling with test gas  $H_2$ , chromium oxide,  $Cr_2O_3$ , would form. Figure 24 shows  $Cr_2O_3$  formed on the Cr film during the exposure to hydrogen contaminated with air. TABLE IX lists the observed d-spacings of  $Cr_2O_3$  and compared the literature values literature [50]. The detail calculation from the electron diffraction pattern is put in APPENDIX B. Figure 24 shows that  $Cr_2O_3$  has an obviously different appearance compared with the superhexagonal hydride on the thin film.

Sample chromium films were also exposed to argon (99.999%) as a control experiment. Figure 25 shows Cr film exposed to argon with air leaks. Neither precipitated particles nor superhexagonal diffraction pattern were observed.  $Cr_3O_4$  formed due to air contamination. TABLE X lists observed d-spacings and those of literature values of  $Cr_3O_4$  [51]. The detail calculation from the electron diffraction pattern is put in APPENDIX B. Figure 25 shows



(a)

(b)



(c)

**Figure 24.**  $\text{Cr}_2\text{O}_3$  on Cr thin film. A  $\text{H}_2$ -exposed sample contaminated by leak of air into BC shows  $\text{Cr}_2\text{O}_3$ . (a), micrograph. (b), ring pattern from  $\text{Cr}_2\text{O}_3$ . (c), indexed duplicated pattern of (b), the numbered spots are from the computer output for the d-spacing calculation.

TABLE IX

TEM OBSERVATION FROM FIGURE 24 AND LITERATURE [50]  
d-SPACINGS OF  $\text{Cr}_2\text{O}_3$  (Å)

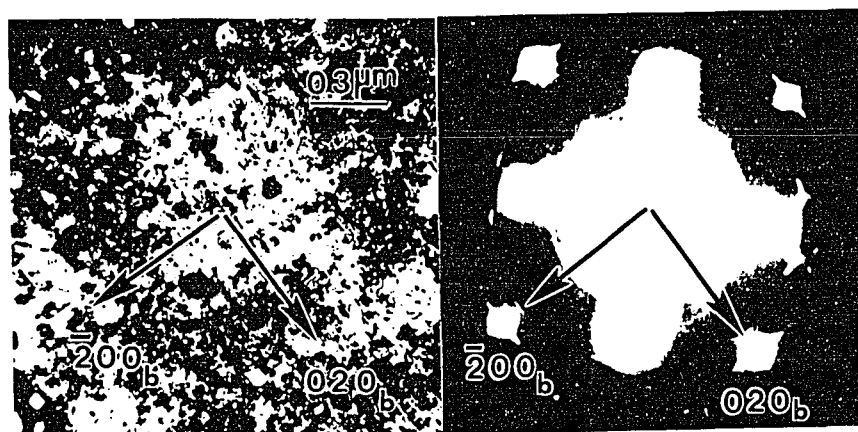
h	k	l	observed	literature
0	1	2	3.60	3.633
1	0	4	2.62	2.666
1	1	0	2.46	2.480
1	1	3	2.17	2.176
2	0	2	2.06	2.048
0	2	4	1.81	1.8156
1	1	6	1.67	1.672
1	2	2	1.58	1.579
3	0	0	1.43	1.4314

TABLE X

TEM OBSERVATION FROM FIGURE 25 AND LITERATURE [51]  
d-SPACINGS OF  $\text{Cr}_3\text{O}_4$  (Å)

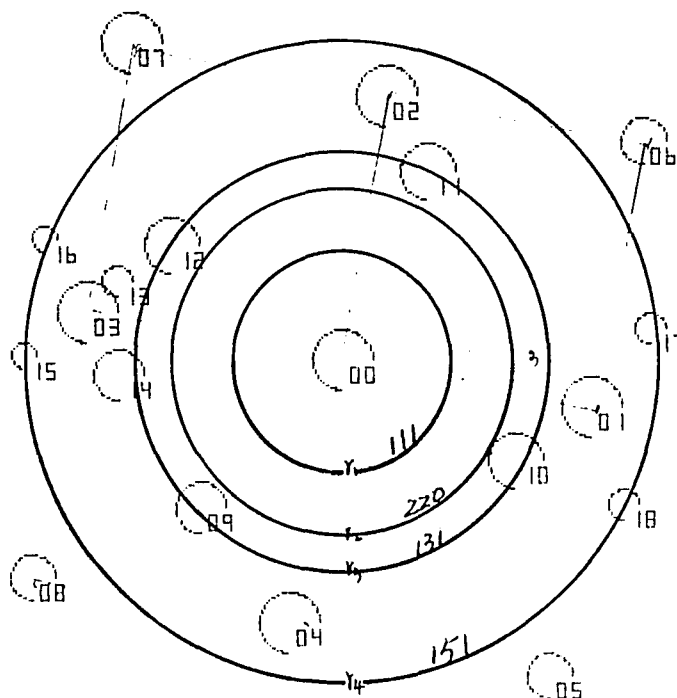
h	k	l	observed	literature
1	1	1	4.78	4.78
2	2	0	3.05	3.09
1	3	1	2.58	2.60
1	5	1	1.66	1.68

that  $\text{Cr}_3\text{O}_4$  has the obviously different appearance compared with the superhexagonal hydride on the thin film. Clearly, the superhexagonal structure is not due to contamination from air leaked into BC. The experimental condition for exposure to Ar is list in TABLE XI.



(a)

(b)



(c)

**Figure 25.**  $\text{Cr}_3\text{O}_4$  on Cr thin film. An Ar-exposed sample contaminated by leak of air into BC shows  $\text{Cr}_3\text{O}_4$ . (a), micrograph. (b), ring pattern from  $\text{Cr}_3\text{O}_4$ . (c), indexed duplicated pattern of (b), the numbered spots are from the computer output for the d-spacing calculation.



TABLE XI  
THERMODYNAMIC CONDITION OF EXPOSURE  
OF Cr THIN FILMS TO Ar

Test gas	Ar
Fill-in pressure	-15 inHg
Driving Ar pressure	200 psi
Minimum distance	5.8 cm
Peak pressure	190 atm
Peak temperature of Cr film	1700-1875 °C

#### Impurity from Mo grid

Another possible source of contamination is from the molybdenum grid. But the chance is eliminated since Mo has a much higher melting point (2610 °C) than Cr, and at the Cr melting point, the vapor pressure of Mo is below  $5 \times 10^{-6}$  mbar in contrast to Cr vapor pressure above 5 mbar (Appendix of [52]). Also the relatively thick Mo grid has lower surface temperature during the exposure because of its greater thermal conductivity. If those particles do result from a Mo compound, they should be formed on sample films exposed to argon as well.

#### Impurity Detection by EDS

SEM equipped with a EDS system was used to examine the Cr thin film before and after the exposures to hot dense gases. The purpose was to make sure that there were no other elements reacting with chromium except hydrogen.

Figure 26 shows the SEM images of Cr thin films on the Mo grids which were taped on the Al stub. The grid holes on the upper side of the grid is 100 mesh, the lower side 200 mesh. The thin films look transparent and the Mo grid underneath the films can be seen clearly with the beam energy of 20 keV. Since the Cr films were deposited on rock salt substrates, two possible impurities were chlorine and sodium. Figure 27 shows EDS spectrum from as-deposited Cr thin film sample. Neither chlorine nor sodium is found in the spectrum from the thin film within the sensitivity. Together with perfect bcc single crystal electron diffraction patterns obtained from as-deposited films (Figure 3), this proves no significant, if any, contamination by the NaCl substrate during vapor deposition. Besides Cr peaks, strong Mo L peaks appear in the spectrum because the Cr thin film is sandwiched and supported by the folding Mo TEM grid. The electron beam can penetrate the thin film and the x-ray signal was also generated from the Mo grid underneath. The back scattered electron with energy up to the energy of the primary beam can also generate x-ray from surrounding Mo grid.

Figure 28 and 29 show EDS spectra from a H<sub>2</sub>-exposed and an Ar-exposed Cr thin film samples respectively. Again neither chlorine nor sodium is found in these spectra. Besides Cr and Mo peaks, a weak Al K $\alpha$  peak can be seen. The diffusive back scattered electrons have a chance to hit the

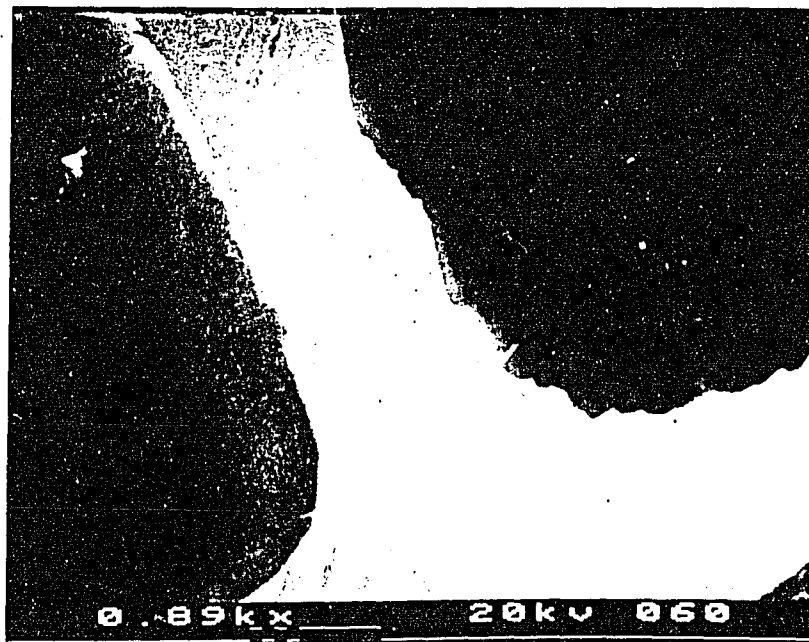
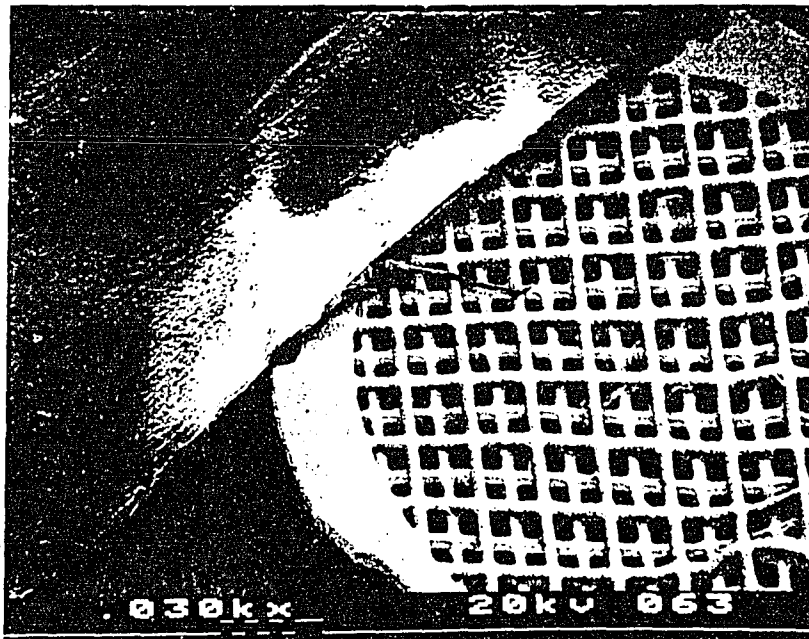


Figure 26. SEM image of Cr thin film on the Mo grid.

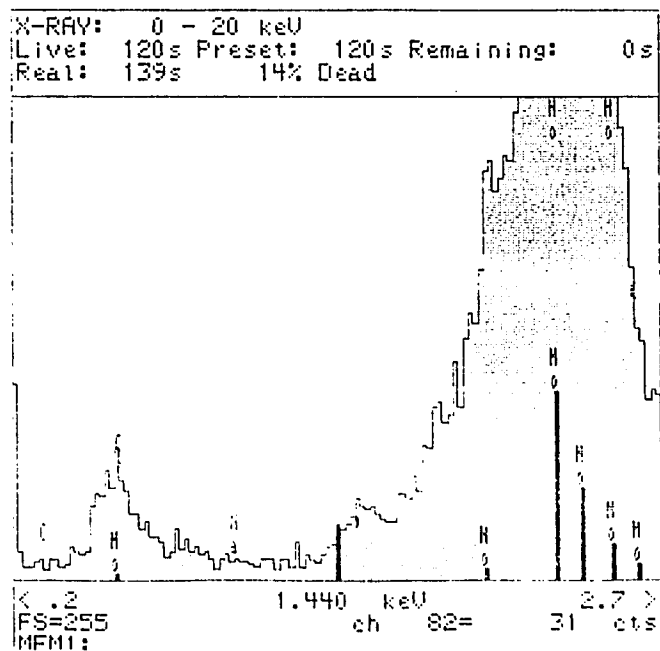
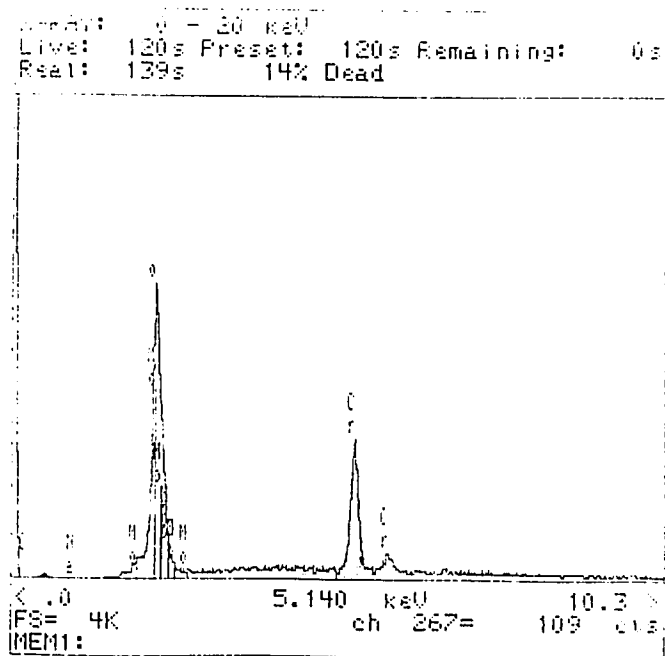


Figure 27. EDS spectrum from as-deposited Cr film. It shows no contamination by NaCl.

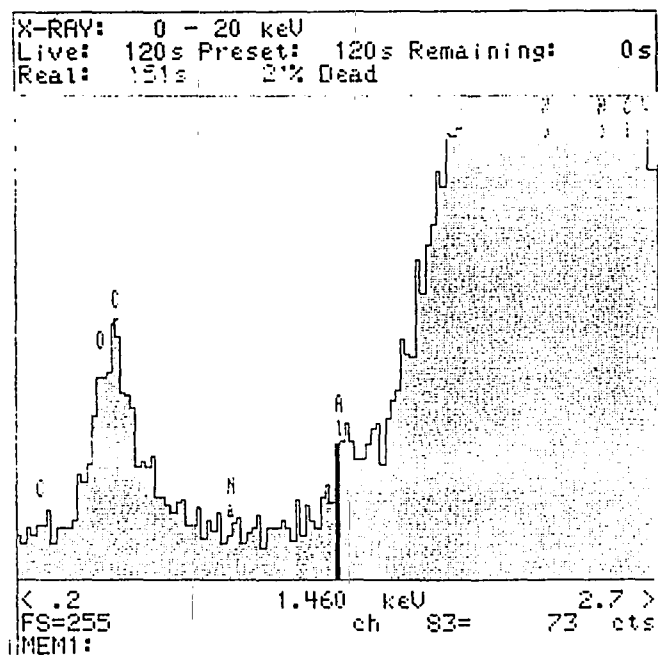
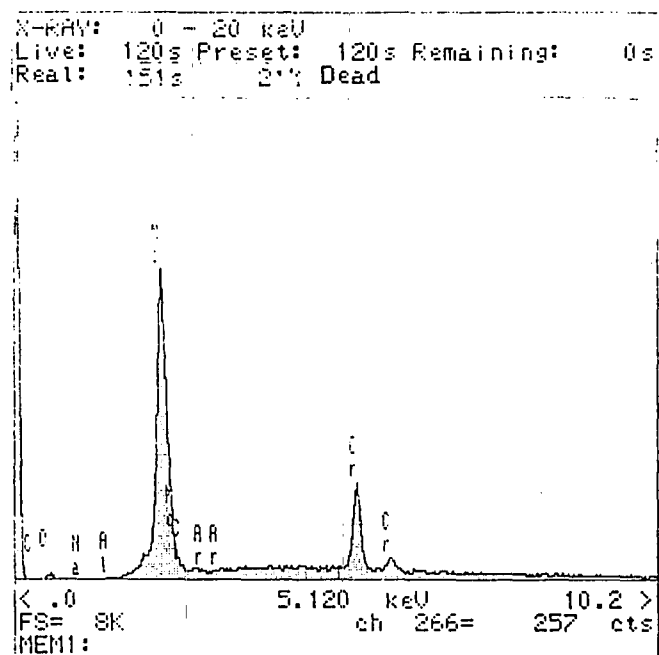


Figure 28. EDS spectrum from H<sub>2</sub>-exposed Cr film.

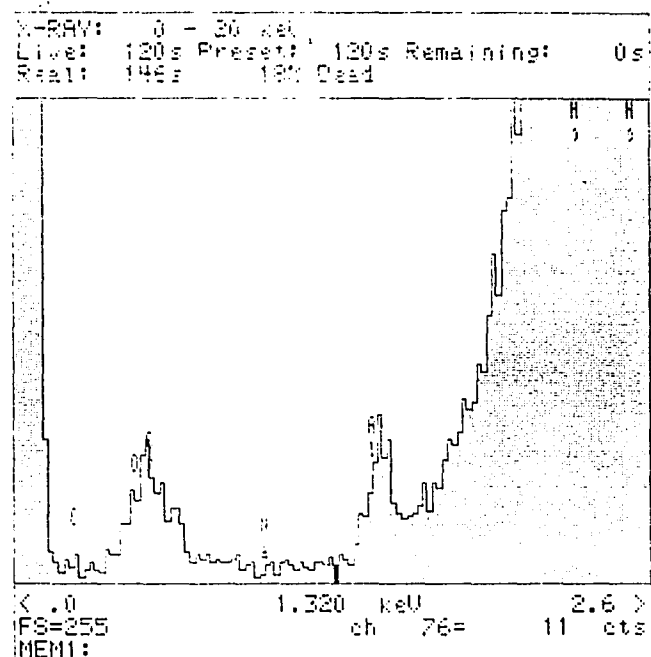
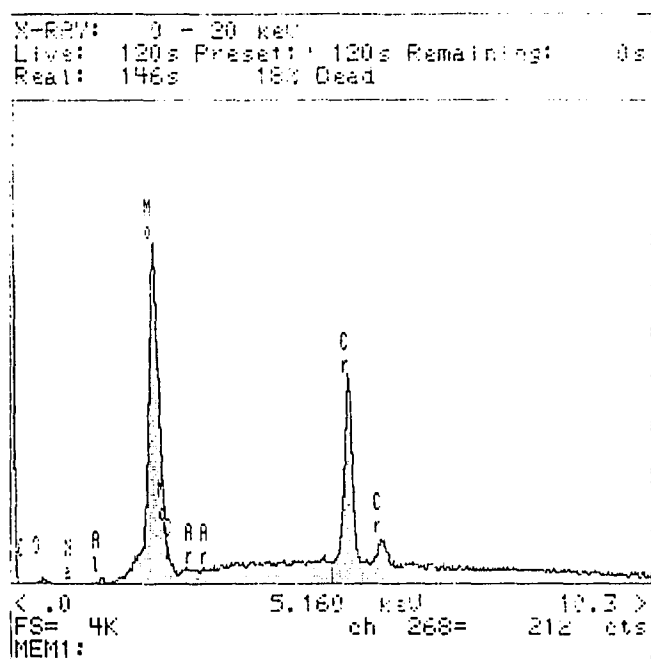


Figure 29. EDS spectrum from Ar-exposed Cr film.

Al stub and generate x-rays from it. Except for these, there were no unexpected elements appearing in these spectra.

#### SUMMARY

As argued above, the superhexagonal structure is caused neither by the possible contamination of NaCl substrate, nor air leaked into the BC, nor Mo grid, nor other unexpected contamination in the experiment performance. After all possible contaminations are ruled out and considering the fact of decomposition by electron beam bombardment and heating, and the observation of the hydrogen spectrum from the discharge tube, those particles could be hydride only.

## CHAPTER VIII

### X-RAY DIFFRACTION EXPERIMENT AND DISCUSSION

#### INTRODUCTION

In an attempt to determine accurate d-spacings of the superhexagonal structure, the Phillips XRG-3000 and General Electric XRD-5 D/F x-ray diffractometers were used to examine the hydrogen exposed samples. However, no matter how many times the samples had been exposed, the x-ray spectra did not show any new structure. In this chapter, x-ray diffraction experiments are summarized, and followed by analysis and discussion.

#### X-RAY DIFFRACTION EXPERIMENT

##### X-ray Diffraction Experiments on Cr Thin films

The x-ray diffraction experiment is similar to that for electron diffraction in principle. The wavelength of x-rays (depending on the target material) is much longer than that of electrons, so the diffraction angle is much larger in the x-ray case according to Bragg's law. Another difference is the fact that the selected area for electron diffraction is as small as a round area with diameter about from 0.5  $\mu\text{m}$  to 5  $\mu\text{m}$ , whereas the x-ray diffraction pattern comes from an area about 1cm x 1cm. Since the sample films are sandwiched



by Mo grids which are much thicker than Cr film (see Figure 26), the mass of the Mo grid involved in x-ray diffraction is much more than that of Cr film. Furthermore, the Mo grid may block some x-rays generated from thin films. Therefore, the x-ray diffraction shows a strong Mo diffraction pattern and a relatively weak Cr diffraction pattern. Some portion of the thin film melts and vaporizes during the exposure, so the Cr diffraction pattern becomes weaker and weaker after each exposure. If some portion of the bcc Cr film transforms into chromium hydride with hexagonal structure, the intensity of diffraction from the new phase depending on its relative amount in the matrix will be even weaker. So, when x-ray diffraction spectra are obtained, more attention is paid to the background pattern to observe the new phase.

#### Cr Thin Films on Mo Grids

The first samples for the x-ray experiment were a group of the same samples which were used for TEM observations-- original thin films with single crystal structure. A group of 9 samples in Mo grids were mounted in front of the piston head of the BC and exposed to hydrogen simultaneously. TEM was used as a monitor to show that the superhexagonal phase had formed in the films. In order to show stronger diffraction from thin film, the sandwich Mo grids were opened and the top grids were removed after the fifth exposure. But still no new phase was observed in the x-ray

diffraction pattern. The  $\text{Cr}_{(110)}$  peak is too weak to be observed. By comparison,  $\text{Mo}_{(200)}$ ,  $\text{Mo}_{(211)}$ , and  $\text{Mo}_{(310)}$   $K\alpha$  peaks are off the scale. TABLE XI lists the measured angles and d-spacings from diffraction peaks and compared with d-spacings of Cr [53] and Mo [54] in literatures. The last column specifies the characteristic x-rays with which the d-spacings are calculated from the observed angles. A weak peak fits  $\text{Mo}_{(211)}$  by calculation with wave length of Cu  $K_\beta$ .

TABLE XII  
X-RAY DIFFRACTION OF Cr THIN FILM ON Mo GRID  
AFTER FIVE EXPOSURES TO  $\text{H}_2$

peak	angle (deg.)	d-spacing ( $\text{\AA}$ )	liter. ( $\text{\AA}$ ) [53, 54]	x-ray of Cu
$\text{Cr}_{(200)}$	64.7	1.439	1.4419	$\bar{K}$
$\text{Mo}_{(110)}$	40.6	2.220	2.225	$\bar{K}$
$\text{Mo}_{(211)}$	65.6	1.285	1.285	$K_\beta$
$\text{Mo}_{(310)}$	101.4	.9954	.9952	$K_{\alpha 1}$
$\text{Mo}_{(310)}$	101.7	.9957	.9952	$K_{\alpha 2}$

Note:  $\bar{K}$  is the average of  $k_{\alpha 1}$  and  $k_{\alpha 2}$ .

#### Cr Thin Films on Glass Slides

In order to remove the interference by Mo grids, sample films are also deposited directly onto the glass slide. Since the substrate is amorphous, the Cr thin films are either amorphous or polycrystalline depending on the substrate temperature. Research on the thin film deposited on glass with temperature 250 °C to 430 °C showed that the

TABLE XIII

X-RAY DIFFRACTION OF Cr THIN FILM DEPOSITED ON GLASS SLIDE  
AFTER SIX EXPOSURES TO H<sub>2</sub>

peak	angle (deg.)	d-spacing (Å)	liter. (Å) [53]	x-ray of Cu
Cr <sub>(110)</sub>	44.7	2.027	2.039	$\bar{K}$
Cr <sub>(200)</sub>	64.8	1.439	1.4419	$\bar{K}$
Cr <sub>(211)</sub>	82.1	1.174	1.1774	$\bar{K}$
Cr <sub>(220)</sub>	98.6	1.017	1.0195	$\bar{K}$
Cr <sub>(310)</sub>	115.8	0.910	0.912	$\bar{K}$

Note:  $\bar{K}$  is the average of  $k_{\alpha 1}$  and  $k_{\alpha 2}$ .

thin films are always polycrystalline [28,29]. In this work, the glass slide was heated to 400 °C in order to obtain crystalline thin films. The chemical reaction of hydrogen during the exposure on polycrystalline film or on single crystal film should be the same. The glass slides then were mounted in front of the piston head of the BC and exposed to hot, dense hydrogen. A sample film on Mo grid was mounted together with the glass slide to serve as a monitor, since the film deposited on the glass can not be investigated under TEM. The polycrystalline films are more desirable for the x-ray diffraction experiment, since they have more chance to show all possible reflections. However, the experimental result still has no sign of a new phase after six exposures in the BC. TABLE XII lists observed peaks angles and d-spacings compared with literature values for Cr [53]. The last column specifies the characteristic

x-rays with which the d-spacings are calculated from the observed angles.

### Discussion

Since the sample films were mounted together with either the Mo grids or the glass slide, they were off its standard plane in the x-ray diffractometer, if there was no proper correction. If so, a sample displacement error would be introduced in the spectra. This particular kind of systematic error causes a peak shift in the spectra [43]. Even though the samples were carefully mounted, still it appears in TABLE XII as the angle (or the calculated d-spacing) shift in one particular direction. By mounting the sample the same way each time, the sample displacement error was kept the same. Any modifications in spectra due to the exposures can be easily observed by comparing the spectra before and after the exposures. Within the sensitivity of x-ray diffractometer, no modification was observed.

## DISCUSSION

### Comparison of electron diffraction and x-ray diffraction

The fact that x-ray diffraction can not detect the superhexagonal phase grown in the thin films suggests something different from that in electron diffraction, which limits the x-ray diffraction experiment. First, since electrons are charged particles, they interact much more strongly with matter than x-rays. The stronger diffraction

effect in electron diffraction (about  $10^6$  times stronger than x-ray diffraction [43]) is easier to be observed from thin film sample. Secondly, the longer wave length of x-rays ( $\approx 1 \text{ \AA}$ ), compared with that of electron ( $\approx 0.05 \text{ \AA}$ ), generate a broader peak width. (A good approximation for diffraction width  $\Delta\theta$  in one dimension gratings diffraction is  $\Delta\theta = \lambda / (Nd)$ , where  $N$  is the number of slits and  $d$  is the spacing between the centers of adjacent slits.) The weak and broad x-ray diffraction peaks may merge within the background diffraction.

#### Non-equilibrium Mechanism

Theoretical Estimation of Heat Diffusion. A rough estimation of the depth of grown particles is give here by comparing thermal diffusion and hydrogen diffusion in the thin film during exposure. The temperature distribution in the thin film during the exposure can be estimated by one dimensional heat conduction theory [55]. The thin film can be thought of as an infinite plate with thickness  $2b$ . The problem can be stated as follows: the plate at initial temperature  $t_i$  is put into a heat reservoir at temperature  $t_a$ . Find the temperature  $t(x, \tau)$  distribution over the plate at time  $\tau$ . Here  $x$  is the distance measured from central symmetrical plane in the plate. The problem is reduced to solve the heat diffusion equation:

$$\frac{\partial t(x, \tau)}{\partial \tau} = a \frac{\partial^2 t(x, \tau)}{\partial x^2} \quad (\tau > 0; -b \leq x \leq b) \quad (8.1)$$

with conditions:

$$t(x, 0) = t_i \quad (8.2)$$

$$t(\pm b, \tau) = t_a \quad (8.3)$$

$$\left. \frac{\partial t(x, \tau)}{\partial x} \right|_{x=0} = 0 \quad (8.4)$$

where  $a$  is the thermal diffusivity of the plate and assumed to be constant for simplicity. The solution can be written in a function:

$$\frac{t(x, \tau) - t_a}{t_i - t_a} = \theta(x/b, Fo) \quad (8.5)$$

where  $Fo = a\tau/b^2$  is the Fourier number, which reflects the effect of dimensionless characteristic time on the process of heating or cooling. When  $Fo > 1.5$ ,  $\theta \approx 0$  for any value of  $x/b$ , and the process of heating or cooling is essentially complete. Since the thermal diffusivity of Cr is 0.29-0.0725 cm<sup>2</sup>/s from room temperature to melting point [56], the thickness of thin film is about  $5.0 \times 10^{-6}$  cm, and if exposure time is about one millisecond, then in the worst case:

$$Fo = 0.0725 \times 1 \times 10^{-3} / (0.25 \times 10^{-5})^2 = 1.2 \times 10^7$$

This indicates that the whole thin film is heated almost instantaneously to the gas temperature uniformly during the

exposure in the ballistic compressor before it is cooled down. Obviously, the formation of superhexagonal chromium hydride is not limited by thermal conduction.

Theoretical Estimation of Hydrogen Diffusion. The diffusion of hydrogen into Cr thin films can be estimated by the differential equation similar to the above equation, including the initial and boundary conditions from (8.1) to (8.5), except that the temperature field  $t(x, \tau)$  is replaced by hydrogen concentration field  $c(x, \tau)$ . The hydrogen permeability in Cr has a value ranged lower than in Cu, but higher than in Al according to [57]. The hydrogen diffusivity in Cu is  $2.3 \times 10^{-9} \text{ cm}^2/\text{s}$  at  $23 \text{ }^\circ\text{C}$  [58]. Calculation with the data from Cu gave the estimated Fourier number hydrogen diffusion in Cr (of  $b=5 \times 10^{-6} \text{ cm}$  at  $\tau=1 \text{ ms}$ ) of less than 0.37 ( $Fo = 2.3 \times 10^{-9} \times 1 \times 10^{-3} / (2.5 \times 10^{-6})^2 = 0.37$ ). The small  $Fo$  means the diffusion process has not been completed. The estimated time required to complete the diffusion process is longer than 4 ms

$(\tau > 1.5 \times b^2 / a = 1.5 \times (2.5 \times 10^{-6})^2 / (2.3 \times 10^{-9}) \approx 4 \times 10^{-3})$ . In the BC, the peak condition time of exposure to  $\text{H}_2$  is only 1 ms. Furthermore, hydrogen gas may undergo a surface reaction to dissociate into atomic hydrogen before diffusing into the thin film. In the  $\text{H}_2$ -Fe system, a calculation predicts [59] that surface dissociation made a significant contribution to the time delay associated with transient hydrogen transport

through iron membranes. If this prediction is also applicable to Cr, hydrogen only penetrates a small distance from surface of Cr film within the exposure time. This calculation indicates that the particles grow only near the surface of the thin film.

Non-equilibrium Mechanism. The above analysis gives an explanation for the non-equilibrium mechanism. During the cooling process, the thermal energy diffuses much faster than hydrogen, and hydrogen remains in the metal. A prediction can be made to other metal-hydrogen systems (or other gas-solid systems) where the same non-equilibrium method can be used to obtain a hydride phase (or other new phases). This is the unique property of a ballistic compressor and its advantage in a non-equilibrium study of materials.

In order to increase the diffusion depth of hydrogen, a longer exposure time is needed. This is limited by the recoil movement of the free piston in the ballistic compressor. Repeated exposures significantly increase the reaction on the surface, but the depth of the reaction changes very slowly. This seems to be the limitation of the ballistic compressor.

In the Cr x-ray diffraction experiment, the estimated depth of the layer from which the diffraction signal is generated, is about 10  $\mu\text{m}$  from the bulk Cr sample surface [43]. In the case of EDS, the estimated depth of the layer



where characteristic x-ray signal generated from, is about 1  $\mu\text{m}$  from a bulk metal sample surface (Appendices of [52]), varying in a depth range with the electron energy. If Cr thin film of about 500  $\text{\AA}$  (0.05  $\mu\text{m}$ ) is used as the sample, the x-ray diffraction pattern or EDS spectrum would be weak. If crystal structure and chemical composition have any modification on the surface layer, in either case, the signal from the modification would be even weaker. The Cr peaks are weaker than Mo peaks in the EDS spectra from Figure 27 to 29, indicating that the majority of the EDS signals are generated from Mo. If the Cr films have some impurities, the peaks showing them would be even weaker. A small amount of contamination on the surface layer may not be detectable by EDS. This suggests that to examine the modification on the sample exposed to hot dense gas in the BC, some other proper techniques and instruments may be more desirable, which are able to examine the crystal structure and chemical component from the outmost surface layer (say within 100  $\text{\AA}$ ), such as low energy electron diffraction (LEED) and Auger electron spectroscopy (AES).

#### Topics for the Future Research

Some experiments for the future research on the superhexagonal chromium hydride would be a must:

1. accurate measurement d-spacings of superhexagonal structure: x-ray diffraction on chromium hydride or other technique for the surface structure.

2. hydrogen atom location, quantitative analysis of hydrogen content, the way of particle growth.
3. exact formation and decomposition conditions, the accurate calculation of exposure temperatures below Cr melting point, relationship between superhexagonal and streak pattern which was observed from the Ar-H<sub>2</sub> mixture exposed Cr film sample.
4. exposure of Fe film (also bcc structure) to pure H<sub>2</sub> would be interesting: to compare with FeH which has double hexagonal structure by high pressure experiment [60] and to compare with Fe<sub>16</sub>H<sub>2</sub> which was obtained by exposure to Ar-H<sub>2</sub> mixture in the BC [22].

## CHAPTER IX

### CONCLUSION

The achievement of this research on synthesis of chromium hydride by direct reaction of metallic Cr with hydrogen at temperatures close to the Cr melting point can be summarized as followings:

1. Chromium hydride with superhexagonal structure and precipitate particle shape is synthesized by exposing Cr thin films to hot, dense hydrogen in a BC. With the quenching effect in the BC, this high temperature phase was obtained and observed in the TEM.

2. With TEM, the lattice constant of the superhexagonal structure was determined as  $A=4.77\text{\AA}$  and  $C/A=1.84$ . It contains 12 Cr atoms in its unit cell with hydrogen atoms occupying interstitial positions.

3. The superhexagonal structure has a larger volume per Cr atom than that of hcp CrH indicates it may contain more hydrogen than hcp CrH.

4. The superhexagonal structure has a definite orientation relation with the bcc Cr matrix:  $[021]_{sh} // [001]_b$  and  $(2\bar{1}2)_{sh} // (\bar{1}\bar{1}0)_b$ .

5. The superhexagonal structure is rather stable at room temperature and at atmospheric pressure in air. When

it is heated to 250 °C in vacuum, the structure changes to bcc by releasing hydrogen which was spectroscopically observed by using a discharge tube.

6. The non-equilibrium method used in this work can probably be used to other metal-hydrogen system (or gas-solid system) to obtain possible high temperature phase.

This superhexagonal Cr hydride is a new observation. To achieve this result, pure hydrogen was for the first time used as testing gas in BC, and every effort had been exerted to keep air contamination to a minimum.

## REFERENCE

1. J. P. Blackledge, in Metal Hydrides, Edited by W. M. Mueller, J. P. Blackledge, and G. G. Libowitz, Academic Press, New York and London, 1968, pp.1-19.
2. G. Thornton and B. Blumberg, *Nucleonics*, Vol. 19, pp.45-51, January, (1961).
3. USAEC Report GA-570, General Dynamics Corporation, Dec. 10, 1958.
4. H. M. Dickamp, R. Balent, and J. R. Welch, *Nucleonics*, Vol. 19, pp.74-75, April, (1961).
5. W. M. Mueller, in Metal Hydrides, Edited by W. M. Mueller, J. P. Blackledge, and G. G. Libowitz, Academic Press, New York and London, 1968, pp.21-50.
6. R. Wiswall, in Hydrogen in Metals, Vol. 2, Edited by G. Alefeld and J. Volkl, Springer-Verlag, Berlin, Heidelberg, and New York, 1978, pp.201-236.
7. G. G. Haselden, Cryogenic Fundamentals, Academic Press, New York, London, 1971, p.23.
8. M. J. Moran and H. N. Shapiro, Fundamentals of Engineering Thermodynamics, John Wiley & Sons, Inc., New York, Chichester, Brisbane, Toronto, Singapore, 1988.
9. J. R. Powell, F. J. Salzano, W. -S. Yu, and J. S. Milan, *Science*, Vol. 193, p.314 (1967).
10. G. Alefeld, in Hydrogen in Metals, Vol. 2, Edited by G. Alefeld and J. Volkl, Springer-Verlag, Berlin, Heidelberg, and New York, 1978, pp.2-10.
11. C. A. Snavely, *Trans. Electrochem. Soc.*, Vol. 92, p.537, (1947).
12. C. A. Snavely, D. A. Vangham: *J. Am. Chem. Soc.*, Vol. 71, p.313, (1949).
13. Yoshiichi Sakamoto, *Journal of Japanese metallurgy society*, Vol. 36, P.458 (1972).

14. K. Sasaki and S. Sekito, *Trans. Electrochem. Soc.*, Vol. 59, p.437 (1931).
15. R. Speiser, in Metal Hydrides, Edited by W. M. Mueller, J. P. Blackledge, and G. G. Libowitz, Academic Press, New York and London, 1968, pp.51-90.
16. A. S. Tetelman, C. N. J. Wagner, and W. D. Robertson, *Acta Met.*, Vol. 9, p.205 (1961).
17. B. Baranovskii and K. Boyarskii, *Roczn, Chem.*, Vol. 46, p.525, (1972).
18. E. G. Ponyatovskii and I. T. Belash, *Dokl. Akad. Nauk SSSR*, Vol. 229, pp.1171-3, (1976).
19. B. Baranovskii (Baranowski) and K. Boyarskii (Bojarski), *Roczn. Chem.*, Vol. 46, P.1403 (1972).
20. M. Takeo and Yi Pan, in Proceedings of the 10th International Conference on High Energy Rate Fabrication, Ljubljana, Yugoslavia. Sept. 18-22, 1989. pp.298-307.
21. H. E. Boyer and T. L. Gall, in Metals Handbook Desk Edition, ASM, Metals Park, Ohio, 1985. pp.1.45-46.
22. M. Takeo, Final Report on Erosion of Metals Exposed to Hot, Dense gases, U. S. Army Research Office Contract #DAAG29-84-K0080, February, 1988.
23. J. Dash, M. Takeo, A. R. Trzyka, J. M. Roush, A. M. Kasaaian, F. B. Brace, H. Takeo, and P. G. Weaver, in Metallurgical Applications of Shock-wave and High-Strain-Rate Phenomena, Edited by L. E. Murr, K. P. Staudhammer, and M. A. Myers, Marcel Dekker Inc., New York and Base, 1986, pp.1051-1069.
24. I. H. Khan, in Handbook of Thin Film Technology, McGraw-Hill, Edited By L. I. Maissel and R. Glang, 1970, chap. 10.
25. Ludmila Eckertova, Physics of Thin Films, Plenum Press, New York, 1977. pp.72-114.
26. O. S. Heavens, Thin Film Physics, Methuen & Co Ltd, 1970, pp.39-52.
27. K. L. Chopra, Thin Film Phenomena, McGraw Hill Book Company, New York, 1969. pp.137-254.

28. A. A. Milgram and Chih-shun Lu, *Journal of Applied Physics*, vol. 39, No. 6, pp.2851-6.
29. K. Hieber and L. Lassak, *Thin Solid Films*, vol. 20, pp.63-73, (1974).
30. A. F. Bardamid and A. I. Shshldervan, *Sov. Phys. Crystallogr.*, Vol. 19, No. 3, pp.414-5, Nov.-Dec., (1974).
31. Hitoshi Hara and Makoto Sakata, *Journal of the Physical Society of Japan*, Vol. 43, No.2, pp.468-476, August, (1977).
32. J. E. Nestell, Jr. and R. W. Christy, *J. Vac. Sci. Technol.* Vol. 15, No. 2, pp.366-9, March/April, (1978).
33. T. Imura, N. Ishihara, M. Okada, and M. Katoh, *Surface Science*, Vol. 86, pp.196-9, (1979).
34. J. E. Nestell, Jr., R. W. Christy, Mitchell H. Cohen, and G. C. Ruben, *J. Appl. Phys.* Vol. 51, No. 1, January, pp.655-660, (1980).
35. T. Imura, *Jpn. J. Appl. Phys.* Vol. 19, No. 1, pp.215-6, (1980).
36. M. Gasfnier and L. Nevot, *Phys. Stat. Sol. (a)* 66, pp.525-540, (1981).
37. V. Agarwal, V. D. Vankar, and K. L. Chopra, *J. Vac. Sci. Technol. A* 6 (4), pp.2341-3, Jul/Aug, 1988.
38. D. Goyal, A. H. King and J. C. Bilello, *Mat. Res. Soc. Symp. Proc.* Vol. 108, pp.395-8, (1988).
39. R. M. Fisher and J. Z. Duan, *Mat. Res. Soc. Symp. Proc.* Vol. 153, pp.299-304, (1989).
40. W. A. Crossland and C. A. Marr, *Japan. J. Appl. Phys.*, Vol. 6, pp.544-6, (1967).
41. J. E. Nestell, Jr. and R. W. Chrusty, *J. Vac. Sci. Technol.*, Vol. 15, No. 2, pp.366-9, (1978).
42. P. B. Hirsch, A. Howie, R. B. Nicholson, D. W. Pashley, and M. J. Whelan, *Electron Microscopy of Thin Film*, New York Plenum Press, London, 1965.
43. S. T. Li, *Analysis Technology of Metal X-Ray Diffraction and Electron Microscopy*, Metallurgical Industry Press, Beijing, 1980. (in Chinese).

44. S. P. Chen and Y. R. Wang, Electron Microscopy of Metals, Mechanical Industry Press, Beijing, 1982. (in Chinese).
45. M. Takeo, Q. A. Holems, and S. Y. Chen, *J. Appl. Phys.*, Vol. 38, No. 9, pp.3544-50, August (1967).
46. A. Trzynka and M. Takeo, *Rev. Sci. Instr.*, March (1988).
47. G. Albert, F. D. Doenitz, K. Kleinstuck and M. Betzl, *Phys. Status. Solidi* 3, K249 (1963).
48. J. W. Christian, The Theory of Transformations in Metals and Alloys, Pergamon Press, Oxford, 1965. p.882.
49. A. Knodler, *Metalloberflache*, Vol. 17, p.331. 1963.
50. Swanson et al., in Index to the Powder Diffraction File 1971, Edit by Leonard G. Berry, Joint Committee on Powder Diffraction Standards, Swarthmore, Pennsylvania, 1971. File ID# 6-0504.
51. Hilty, Forgeng and Folkman, in Index to the Powder Diffraction File 1971, Edit by Leonard G. Berry, Joint Committee on Powder Diffraction Standards, Swarthmore, Pennsylvania, 1971. File ID# 12-559.
52. I. M. Watt, The Principles and Practice of Electron Microscopy, Cambridge University Press, London, 1985.
53. Swanson et al., in Index to the Powder Diffraction File 1971, Edit by Leonard G. Berry, Joint Committee on Powder Diffraction Standards, Swarthmore, Pennsylvania, 1971. File ID# 6-0694.
54. Swanson et al., in Index to the Powder Diffraction File 1971, Edit by Leonard G. Berry, Joint Committee on Powder Diffraction Standards, Swarthmore, Pennsylvania, 1971. File ID# 4-0809.
55. A. V. Luikov, Analytical Heat Diffusion Theory, Edited by James P. Hartnett, Academic press, 1968. New York and London. pp.97-109.
56. Y. S. Touloukian et al., Thermal Diffusivity, Thermophysical properties of Matter, The TPRC Data Series, Vol 10, Plenum Pud. Corp., 1970.
57. G. Adachi, H. Sakaguchi, t. Shimoguhri, J. Shiokawa, *Journal of the Less-Common Metals*, Vol. 133, No. 2, pp.271-5, (1987).



58. D. W. Dewulf, A. J. Bard, *Journal of the Electrochemical Society*, Vol. 132, No. 2, pp.2965-7, (1985).
59. M. R. Shanabarger, A. Taslami, H. G. Nelson, *Scr. Metall.*, Vol. 15, No.8, pp.923-33, (1981).
60. V. E. Antonov, I. T. Belash, V. F. Degtyareva, D. N. Mogilyansky, B. K. Ponomarev and V. Sh. Shekhtman, *Int. J. Hydrogen Energy*, Vol. 14, No. 6, pp.371-7, (1989).

APPENDIX A

PROCEDURE FOR MAKING SINGLE CRYSTAL Cr THIN FILMS

## APPENDIX A

## PROCEDURE FOR MAKING SINGLE CRYSTAL Cr THIN FILMS

- a. Open vacuum chamber by lifting the chamber cap with ratchet mechanism. (see Figure 2).
- b. Cover the vacuum chamber with a piece of plastic sheet to prevent dust from dropping into the chamber.
- c. Open the shield case for the tungsten basket and open the substrate holder at the bottom of the substrate heater.
- d. Put about 5 mg of chromium powder into the tungsten basket.
- e. Cleave a piece of rock salt with surface area about  $1 \times 1 \text{ cm}^2$  and thickness 3mm, blow rock salt dust off the cleaved surface with nitrogen gas, put it on the substrate holder with the cleaved surface down, then insert the holder onto the substrate heater.
- f. Close the tungsten basket shielding case.
- g. Take off the plastic sheet and gradually lower the vacuum chamber cap assembly. Let the cap sit on the top of the chamber so that the O-ring is in its proper place.
- h. Evacuate the chamber with the absorption pump for about 1 hour, followed by the ion pumps, until the pressure comes down to  $4-6 \times 10^{-7}$  torr.
- i. Switch on the substrate oven, wait until oven temperature goes up to about  $500 \text{ }^\circ\text{C}$ . Keep the temperature at  $515-525 \text{ }^\circ\text{C}$  for 15 minutes. The pressure in vacuum chamber usually goes up to  $1-2 \times 10^{-6}$  torr.
- j. Switch on the variac for heating the tungsten basket and turn it quickly so that a voltage of about 7.75 volt output from variac was applied to a transformer. The evaporation of chromium powder inside the tungsten basket occurs within 2-3 seconds, this can be judged by the pressure in the chamber, which first increase rapidly and comes back down again. Turn the variac to zero voltage and switch it off.
- k. Switch off the oven and cool it with compressed air.
- l. Switch off the ion pumps and wait until the oven gets to room temperature. (usually 30-40 minutes)

- m. Introduce nitrogen gas into vacuum chamber, lift the chamber cap, and cover the chamber with a protecting plastic sheet. Then take out the rock salt substrate. The deposit films are shiny.
- n. Carve the deposit with a cleaving knife and divide the whole deposit film into small squares about 2mmx2mm.
- o. Dissolve the rock salt in deionized water in a crystallizing dish. The deposited chromium thin film will float on the surface due to the surface tension. The floating films are then picked up and transferred to another dish of deionized water. In this way the chance of contamination of deposit film by sodium chloride is minimized.
- p. Pick up a small square film with a molybdenum folding grid for the transmission electron microscope and sandwich the film in the grid. In this way, about a dozen sample grids can be made from one evaporation.

APPENDIX B

PROCESSING OF ELECTRON MICROSCOPE DATA

## APPENDIX B

## PROCESSING OF ELECTRON MICROSCOPE DATA

## ELECTRON DIFFRACTION PATTERNS

1. Procedures.

- a. The distances from the center of the pattern and angles subtended by the diffraction spots at the center were measured directly from the photographic negative by a computerized camera [46] and from the positive print by a microscope with a micrometer on it. Spots with 'symmetry' flag in the computer output help the decision of diffraction pattern center in the program.
- b. The camera constant was calibrated with spots due to known matrix bcc chromium. In the diffraction pattern, the camera constant is related to the distance  $r$  of a spot from the center by [43]:

$$c.c.=a+b*r^2$$

where  $a$  and  $b$  are constants. The distances ( $r$ ) from center of spots with known bcc Cr lattice spacing  $d_s$  were measure and the relation  $c.c.'=d_s*r$  was use to find 'known' c.c.' data to calibrate c.c., This was done by the computer program 1, 'cc' (in Appendix C) with least squares method.

- c. With camera constant from (b), the corresponding  $d$ -spacings were calculated for all spots on the diffraction pattern with computer program 2, 'ds'(in Appendix C). These  $d$ -spacings and angles obtained from step (a) are the observed values.
- d. For the superhexagonal structure, trial values were assigned to the lattice constant  $A$  and ratio  $C/A$ . Index the diffraction spots from the best estimate. Then calculate  $d$ -spacings and relative angles. This step was repeated with computer program 3, 'hex1'. The final value for  $A$  is  $A=4.77\text{\AA}$ , from Figure 10, because it has  $(H00)_{sh}$ , and the ratio  $C/A=1.84$  from Figure 16 because it has  $(00L)_{sh}$ .
- e. For  $Cr_2O_3$  (Figure 25) and  $Cr_3O_4$  (Figure 26), the observed values were compared with literature values.

## 2. Output of Computer Calculation.

Calculation from Figure 10. See Figure 10 (c) for spot number and TABLE IV for the comparison of theoretical and observed values.

FILE: 9-13-007.DAT

Number	Symmetry	Distance (cm)	Angle (deg)
0	FALSE	0.051	-14.1
1	TRUE	1.825	0.0
2	TRUE	1.814	180.7
3	TRUE	1.837	89.5
4	TRUE	1.811	269.7
5	TRUE	2.561	315.0
6	TRUE	2.616	45.1
7	TRUE	2.656	135.6
8	TRUE	2.682	224.6
9	TRUE	0.874	222.1
10	TRUE	0.909	39.8
11	TRUE	1.808	39.2
12	TRUE	1.807	221.3
13	TRUE	1.225	333.0
14	TRUE	1.212	152.1
15	TRUE	1.224	109.3
16	TRUE	1.210	290.4
17	FALSE	2.326	131.5
18	FALSE	2.789	221.6
19	FALSE	1.773	81.3
20	FALSE	1.766	261.5
21	FALSE	2.704	311.5
22	FALSE	3.411	-0.1
23	FALSE	3.718	0.9

All distances are +/- 0.017 cm within 99% confidence limits.  
End of data.

cc=a+b\*r\*r

r(obs.)	d	cc
1.8250	2.0390	3.7212
1.8140	2.0390	3.6987
1.8370	2.0390	3.7456
1.8110	2.0390	3.6926
2.5610	1.4419	3.6927
2.6160	1.4419	3.7720
2.6560	1.4419	3.8297
2.6820	1.4419	3.8672
3.7180	1.0195	3.7905

a=3.69775900

b= .00968863

	r(obs.)	d	cc
1	1.8250	2.0439	3.7300
2	1.8140	2.0560	3.7296
3	1.8370	2.0307	3.7305
4	1.8110	2.0594	3.7295
5	2.5610	1.4687	3.7613
6	2.6160	1.4389	3.7641
7	2.6560	1.4180	3.7661
8	2.6820	1.4047	3.7675
9	.8740	4.2393	3.7052
10	.9090	4.0767	3.7058
11	1.8080	2.0627	3.7294
12	1.8070	2.0639	3.7294
13	1.2250	3.0304	3.7123
14	1.2120	3.0627	3.7120
15	1.2240	3.0329	3.7123
16	1.2100	3.0677	3.7119
17	2.3260	1.6123	3.7502
18	2.7890	1.3529	3.7731
19	1.7730	2.9528	3.7282
20	1.7660	2.1110	3.7280
21	2.7040	1.3937	3.7686
22	3.4110	1.1171	3.8105
23	3.7180	1.0306	3.8317

Calculation from Figure 13. See Figure 13 (b) for spot number and TABLE V for the comparison of theoretical and observed values.

FILE: 11-7-007.DAT

Number	Symmetry	Distance (cm)	Angle (deg)
0	FALSE	0.035	-54.9
1	TRUE	1.239	0.0
2	TRUE	1.227	180.9
3	TRUE	1.405	245.7
4	TRUE	1.391	64.1
5	FALSE	1.413	116.0
6	FALSE	1.419	296.9
7	TRUE	2.949	295.2
8	TRUE	3.021	115.8
9	TRUE	2.314	147.4
10	TRUE	2.255	-32.7
11	FALSE	2.550	271.3
12	FALSE	2.574	277.1
13	FALSE	2.869	245.1
14	FALSE	2.286	215.7
15	FALSE	2.570	181.5
16	TRUE	2.550	189.0
17	TRUE	2.534	222.9
18	TRUE	3.333	248.1
19	TRUE	2.557	8.1
20	FALSE	2.495	10.3
21	TRUE	2.564	41.5
22	FALSE	2.526	51.0
23	TRUE	3.364	68.4
24	FALSE	3.246	-17.5
25	FALSE	3.520	-37.4
26	FALSE	4.033	268.4
27	FALSE	1.298	281.4

All distances are +/- 0.016 cm within 99% confidence limits.  
End of data.

$$cc=a+b*r*r$$

r(obs.)	d	cc
1.4130	2.0390	2.8811
1.4190	2.0390	2.8833
2.9490	1.0195	3.0065
3.0210	1.0195	3.0799
2.5500	1.1774	3.0024
3.3340	1.1774	3.9835
3.3330	1.9120	3.0397
2.5570	1.1774	3.0106
2.5640	1.1774	3.0189
3.3640	.9120	3.0680

$$a=2.86646000$$

$$b= .01876798$$

r(obs.)	d	cc
1	1.2390	2.3368
2	1.2270	2.3592
3	1.4050	2.0666
4	1.3910	2.0868
5	1.4130	2.0552
6	1.4190	2.0467
7	2.9490	1.0274
8	3.0210	1.0055
9	2.3140	1.2822
10	2.2550	1.3135
11	2.5500	1.1720
12	2.5740	1.1619
13	2.8690	1.0530
14	2.2860	1.2968
15	2.5700	1.1636
16	2.5500	1.1720
17	2.5340	1.1788
18	3.3330	.9226
19	2.5570	1.1690
20	2.4950	1.1957
21	2.5640	1.1661
22	2.5260	1.1822
23	3.3640	.9152
24	3.2460	.9440



Calculation from Figure 16. Spots were measured by microscope from print. From this measurement, the ratio C/A was decided. See Figure 16 (c) for spot indices and TABLE VI for the comparison of theoretical and observed values.

spot	distance (mm)	angle (deg.)
$(1 \bar{2} 0)_{sh}$	58.248	0
$(0 0 2)_{sh}$	31.663	90

$$d_{(002)}=C/2, d_{(1\bar{2}0)}=A/2, \text{ and}$$

$$d_{(002)}/d_{(1\bar{2}0)}=C/A=58.248/31.663=1.84$$

Calculation from Figure 25. Spots #19 and #20 are measured by micrometer. See Figure 25 (c) for other spot numbers. See TABLE X for comparison with  $Cr_3O_4$  data.

FILE: 8-22-010.DAT

Number	Symmetry	Distance (cm)	Angle (deg)	r(obs.)	d	cc
0	FALSE	0.035	-347.2	1.7810	2.0390	3.6315
1	TRUE	1.781	0.0	1.7900	2.0390	3.6498
2	TRUE	1.790	-271.0	1.7650	2.0390	3.5988
3	TRUE	1.765	-180.7	1.7900	2.0390	3.6498
4	TRUE	1.790	-90.7	2.5560	1.4419	3.6855
5	TRUE	2.556	-45.6	2.5450	1.4419	3.6696
6	TRUE	2.545	-315.1	2.5540	1.4419	3.6826
7	TRUE	2.554	-225.9	2.5930	1.4419	3.7388
8	TRUE	2.593	-135.3			
9	FALSE	1.377	-123.7			
10	FALSE	1.388	-18.9			
11	FALSE	1.405	-286.1			
12	FALSE	1.387	-203.9			
13	FALSE	1.612	-188.7			
14	FALSE	1.527	-165.8			
15	FALSE	2.188	-170.4			
16	FALSE	2.198	-191.6			
17	FALSE	2.161	-344.3			
18	FALSE	2.174	-16.0			

cc=a+b\*r\*r

a=3.57214200      b= .01872458

r(obs.)	d	cc	
1	1.7810	2.0390	3.6315
2	1.7900	2.0291	3.6321
3	1.7650	2.0569	3.6305
4	1.7900	2.0291	3.6321
5	2.5560	1.4454	3.6945
6	2.5450	1.4512	3.6934
7	2.5540	1.4465	3.6943
8	2.5930	1.4262	3.6980
9	1.3770	2.6199	3.6076
10	1.3880	2.5996	3.6082
11	1.4050	2.5688	3.6091
12	1.3870	2.6014	3.6082
13	1.6120	2.2462	3.6208
14	1.5270	2.3679	3.6158
15	2.1880	1.6736	3.6618
16	2.1980	1.6663	3.6626
17	2.1610	1.6935	3.6596
18	2.1740	1.6838	3.6606
19	.7500	4.7769	3.5827
20	1.1650	3.0880	3.5976

All distances are +/- 0.016 cm within 99% confidence  
End of data.

Calculation from Figure 24. See Figure 24 (c) for spot number and TABLE IX for comparison with Cr<sub>2</sub>O<sub>3</sub> data.

FILE: 8-1-009.DAT

cc=a+b\*r\*r

Number	Symmetry	Distance (cm)	Angle (deg)	r(obs.)	d	cc
0	FALSE	0.012	352.1	2.0560	2.0390	4.1922
1	FALSE	1.167	0.0	2.0720	2.0390	4.2248
2	FALSE	1.601	-2.0	2.0790	2.0390	4.2391
3	FALSE	1.710	-1.8	2.0660	2.0390	4.2126
4	FALSE	1.946	-0.6	2.9970	1.4419	4.3214
5	FALSE	2.051	353.8	2.9800	1.4419	4.2969
6	FALSE	2.334	355.5	2.9710	1.4419	4.2839
7	FALSE	2.543	-0.3	2.9840	1.4419	4.3026
8	FALSE	2.670	-0.1			
9	FALSE	2.967	2.1			
10	FALSE	1.142	175.1			
11	FALSE	1.595	179.6	a=4.13857700	b= .01830544	
12	FALSE	1.697	179.1			
13	FALSE	1.940	179.9			
14	FALSE	2.065	166.1			
15	FALSE	2.355	175.6			
16	FALSE	2.565	176.8			
17	FALSE	2.721	176.8			
18	FALSE	3.022	175.9			
19	FALSE	1.167	85.2			
20	FALSE	1.601	78.2			
21	FALSE	1.712	80.4			
22	FALSE	1.957	79.4			
23	FALSE	2.056	75.9			
24	FALSE	2.350	77.0			
25	FALSE	2.565	75.7			
26	FALSE	2.710	73.7			
27	FALSE	3.012	75.1			
28	FALSE	1.149	268.3			
29	FALSE	1.594	278.6			
30	FALSE	1.696	277.2			
31	FALSE	1.931	269.8			
32	FALSE	2.014	264.3			
33	FALSE	2.333	266.3			
34	FALSE	2.543	269.3			
35	FALSE	2.699	264.3			
36	FALSE	2.998	257.9			
37	TRUE	2.056	286.7			
38	TRUE	2.072	15.8			
39	TRUE	2.079	105.8			
40	TRUE	2.066	196.2			
41	TRUE	2.997	241.1			
42	TRUE	2.980	331.5			
43	TRUE	2.971	61.4			
44	TRUE	2.984	151.6			
1						
2						
3						
4						
5						
6						
7						
8						
9						
10						
11						
12						
13						
14						
15						
16						
17						
18						
19						
20						
21						
22						
23						
24						
25						
26						
27						
28						
29						
30						
31						
32						
33						
34						
35						
36						
37						
38						
39						
40						
41						
42						
43						
44						

All distances are +/- 0.022 cm within 99% confidence  
End of data.

ROTATION OF TEM MICROGRAPHS WITH RESPECT TO  
ELECTRON DIFFRACTION PATTERN

The rotation angles ( $\theta$ ) of electron micrographs relative to the electron diffraction pattern due to the change in strength of intermediate and projector lenses of HU-125C were calibrated.

A series of images of a grid (2000 lines/in) were taken by steps from diffraction lens settings to the conventional micrograph lens settings by first changing intermediate lens current by steps with a constant projector lens current, then changing the projector lens current by steps with a constant intermediate lens current.

Angles are then measured from the edges of image negatives to an arbitrary direction drawn on the paper for the calibration. By plotting the angles of micrographs as a function of lens current, slopes were obtained which represent the rotation angles per unit lens current by the lens. The rotation angles for the conventional micrographs can be calculated by extrapolating to the diffraction current with the obtained slopes. Similar calibrations were made for both intermediate and projector lenses.

Since the rotation of the intermediate lens was opposite to the projector lens, a negative sign was for rotation of the intermediate lens, which is in counter clockwise direction, and a positive sign for the rotation of the projector lens, which is in clockwise direction.

50kV. The intermediate lens. (with projector lens current 35.2 mA)

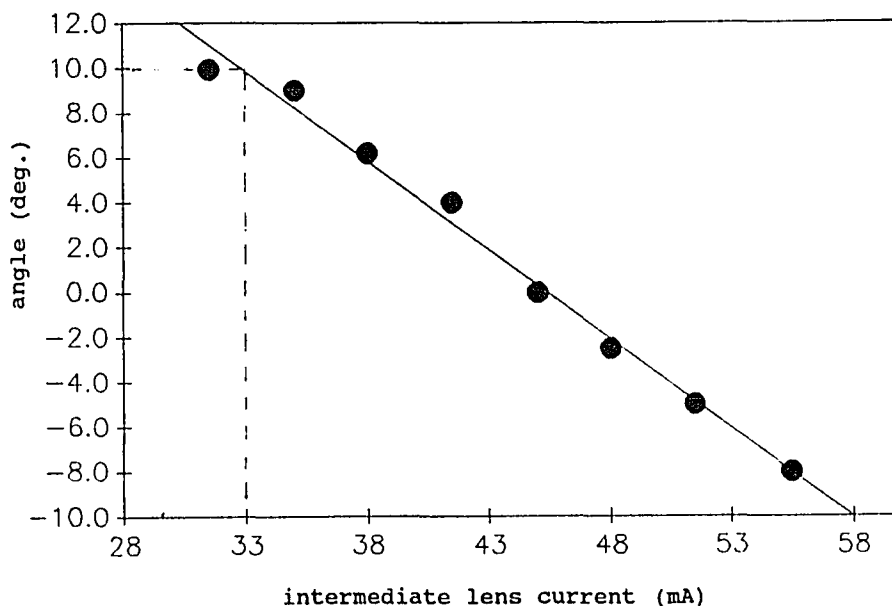


Figure 30. Image rotation by intermediate lens. (50kv)

$$\text{Slope} = (-10-10)/(58-33) = -.80 \text{ (deg./mA)}$$

To compare a micrograph and corresponding diffraction pattern, the necessary rotation  $\theta_1$  of the micrograph (I=55.5 mA) from diffraction (I=29.5 mA) should be:

$$\theta_1 = \text{slope} \times (55.5-29.5) = -0.80 \times 26.0 = -20.8 \text{ (deg.)}$$

The negative angle means the rotation of the micrographs is counterclockwise.

The projector lens. (with intermediate lens current 55.5 mA)

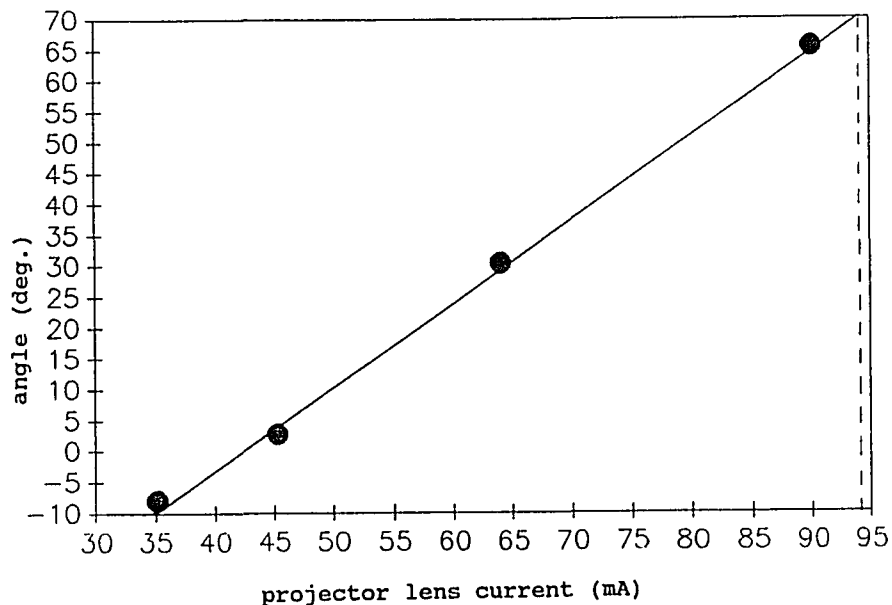


Figure 31. Image rotation by projector lens. (50kv)

$$\text{Slope} = (70+10)/(93-33.5) = 1.34 \text{ (deg./mA)}$$

The necessary rotation  $\theta'$  of micrograph of higher magnification from lower magnification due to the change in strength of the projector lens should be:

$$\theta' = \text{slope} \times (90-35.2) = 1.34 \times 54.8 = 73.7 \text{ (deg.)}$$

The positive angle means the rotation of the micrographs is clockwise. The necessary rotation  $\theta_2$  of micrograph of higher magnification from

diffraction pattern is obtained and should be:

$$\theta_2 = \theta' + \theta_1 = 73.7 - 20.8 = 52.9 \text{ (deg.)}$$

The net positive angle means the rotation is clockwise.

75kV. The intermediate lens. (with projector lens current 41.0 mA)

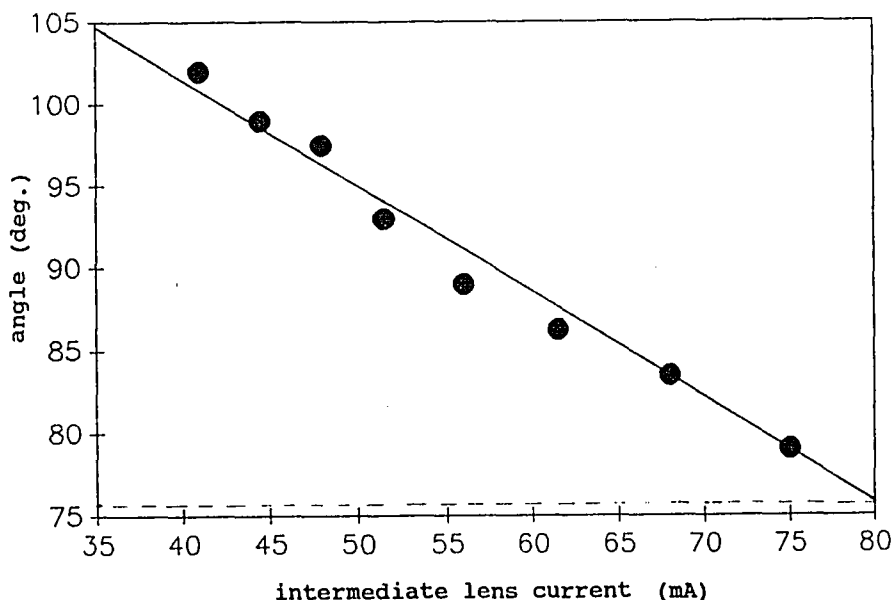


Figure 32. Image rotation by intermediate lens. (75kv)

$$\text{Slope} = (76 - 105) / (80 - 35) = -0.64 \text{ (deg./mA)}$$

To compare micrograph and diffraction, the necessary rotation of micrograph (I=75.0 mA)  $\theta_1$  from diffraction (I=37.0 mA) should be:

$$\theta_1 = \text{slope} \times (75.0 - 37.0) = -0.64 \times 38 = -24.5 \text{ (deg.)}$$

The negative angle means the rotation of the micrographs is counterclockwise.

The projector lens. (with intermediate lens current 75.0 mA)

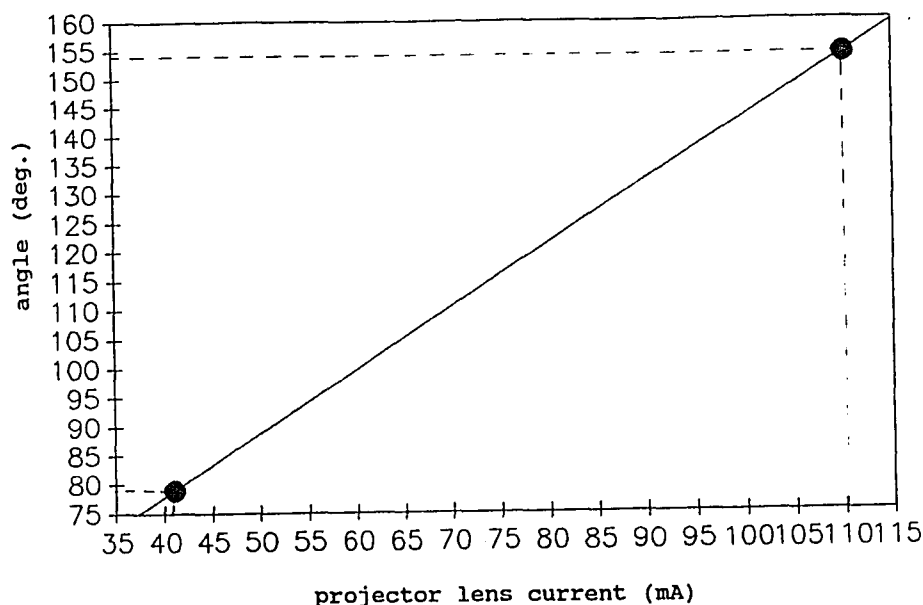


Figure 33. Image rotation by projector lens. (75kv)

$$\text{Slope} = (154-79)/(110-41) = 1.09 \text{ (deg./mA)}$$

The necessary rotation of a micrograph of higher magnification from lower magnification due to the change in strength of projector lens should be:

$$\theta' = \text{slope} \times (110.0 - 41.0) = 75.0 \text{ (deg.)}$$

The positive angle means the rotation of the micrographs is clockwise. The necessary rotation of a micrograph of higher magnification from the diffraction pattern is obtained and should be:

$$\theta_2 = \theta' + \theta_1 = 75.0 - 24.5 = 50.5 \text{ (deg.)}$$

The net positive angle means the rotation is clockwise.

### Discussion.

The rotation of an image by a magnetic lens can be expressed by [42]:

$$\theta = \frac{k}{\sqrt{E}} \int H_z dz = \frac{k}{\sqrt{E}} i \int H'_z dz = \frac{K}{\sqrt{E}} i$$

and

$$K = k \int H'_z dz$$

where E is the electron energy in electron volts;  $H_z$  is the z-component of the field and proportional to the lens current i, so that  $H_z = iH'_z$  and  $H'_z$  is the proportionality constant; K is a constant independent of the lens current. Therefore, the rotation due to the lens strength can be plotted in a straight line and the slope can be written as:

$$\frac{\partial \theta}{\partial i} = \frac{K}{\sqrt{E}}$$

For a given lens, the slope is proportional to the reciprocal of the square root of the electron beam energy:

$$\frac{(\text{slope})_{50\text{kV}}}{(\text{slope})_{75\text{kV}}} = \sqrt{\frac{75}{50}} = 1.225$$

The result of calibration for the intermediate lens and the projector lens shows the slope ratios are close to the above analysis. In the case of the intermediate lens:

$$\text{slope ratio} = 0.80/0.64 = 1.24$$

and in the case of the projector lens:

$$\text{slope ratio} = 1.34/1.09 = 1.23.$$

The comparison of the results from HU-125C for high voltages of 50 kV and 75 kV proves the calibrations were made properly.

APPENDIX C

COMPUTER PROGRAM



## APPENDIX C

## COMPUTER PROGRAM

(Program 1 to 7 are coded in FORTRAN, 8 in TRUE BASIC)

1. cc

```

      program cc
c*****
c*
c*   this program is for the camera constant from electron *
c*   diffraction pattern data by least squares             *
c*
c*   variable:      cc = a+b*r*r                            *
c*                  r      distance of spot from center    *
c*                  n      number of measured r            *
c*                  d      known d-spacings                *
c*****
      integer n
      real a,b,deta,r(20),cc(20),d(20)
      open (6,file='lpt1:',status='new')
      open (7,file='ccin1',status='old')
      deta=0.0000001
      rewind 7
      read (7,*) n
      write(6,100)
      write (6,103)
      a=1.1
      b=1.1
      a1=0.0
      b1=0.0
      c1=0.0
      d1=0.0
      do 10 i=1,n
         read (7,*) r(i),d(i)
         cc(i)=d(i)*r(i)
         a1=a1+cc(i)
         b1=b1+r(i)**2.0
         c1=c1+r(i)**4.0
         d1=d1+r(i)**2.0*cc(i)
         write (6,102) r(i),d(i),cc(i)
10      continue
20      a0=a
         b0=b
         a=(a1-b*b1)/n
         b=(d1-a*b1)/c1
         if (abs(a-a0).gt.deta.and.abs(b-b0).gt.deta) goto 20
         write (*,*) 'a=',a
         write (*,*) 'b=',b

```

```

write(6,101) a,b
100 format(10x,'cc=a+b*r*r')
101 format(/,10x,'a=',f10.8,5x,'b=',f10.8)
102 format(6x,3(f8.4,3x))
103 format(/,10x,'r(obs.)',5x,'d',9x,'cc')
stop
end

```

## 2. ds

```

program ds
c*****
c*
c*   this program is for d-spacings with known camera   *
c*   constant                                             *
c*
c*   variable:      cc = a+b*r*r                         *
c*                  ds = cc/r                           *
c*                  r   distance of spot from center    *
c*                  n   number of measured r           *
c*
c*****
integer n
real a,b,deta,r(80),cc(80),d(80)
open (6,file='lpt1:',status='new')
open (7,file='dsin1',status='old')
deta=0.000001
read (7,*) n
write (*,*) 'input a, b'
read (*,*) a,b
write (6,101)a,b
write (6,103)
c   a=4.138577
c   b=.01830544
do 10 i=1,n
  read (7,*) r(i)
  cc(i)=a+b*r(i)*r(i)
  d(i)=cc(i)/r(i)
  write (6,102)i, r(i),d(i),cc(i)
10 continue
101 format (8x,'cc=a+b*r*r, a=',f8.6,1x,'b=',f8.6)
102 format(8x,i2,3(3x,f6.4))
103 format(13x,'r(obs.)',5x,'d',6x,'cc')
stop
end

```

3. hex1

```

      program hex1
c*****
c*
c*   this program is for plotting a table of d spacings,
c*   angles with known a and c/a, comparing with
c*   observed values
c*
c*   variable:   1/d**2=4/3(h*h+h*k+k*k)/a**2+l**2/c**2
c*
c*           h1*h2+k1*k2+(h2*k1+h1*k2)/2+3/4*l1*l2*(a/c)**2
c* cos(fi)=-----
c*           sqrt((h1*h1+k1*k1+h1*k1+3/4(a/c)**2*l1*l1)*
c*                (h2*h2+k2*k2+h2*k2+3/4(a/c)**2*l2*l2))
c*
c*           4(c/a)**2*(h1*h1+k1*k1+h1*k1)+3*l1*l1
c* r2/r1=sqrt(-----)
c*           4(c/a)**2*(h2*h2+k2*k2)+3*l2*l2
c*
c*****
      integer h1,k1,l1,h2,k2,l2,h(50),k(50),l(50)
      real d,d1(3),fi,fi1(4),a,c1(4),rac,d0(50),fi0(50)
      open (7,file='hex1in1',status='old')
      open (6,file='lpt1:',status='new')
      rewind 7
      read (7,*) a
      read (7,*)(c1(i),i=1,1)
      write (6,103) a,(c1(i),a*c1(i),i=1,1)
      write (6,102)
      m=1
10  read(7,*) h(m),k(m),l(m),d0(m),fi0(m)
      h1=h(m)
      k1=k(m)
      l1=l(m)
      if (h1.eq.0 .and. k1.eq.0.and.l1.eq.0) goto 104
      ip=h1*h1+k1*k1+h1*k1
          if (ip.eq.2) goto100
          if (ip .eq. 5) goto 100
          if (ip .eq. 6) goto 100
          if (ip .eq. 8) goto 100
          if (ip .eq. 10) goto 100
          if (ip .eq. 11) goto 100
      if ((ip.eq.0).and.(l1.eq.0)) goto 104
      do 15 j=1,1
          c=c1(j)*a
          d=float(ip)*4.0/3.0/a**2.0
          d=d+float(l1*l1)/c**2.0
          d=1/sqrt(d)
          if (m.eq.1) then
              h2=h1
              k2=k1

```

```

                l2=l1
                fi=0.0
            endif
            fi=float(h1*h2+k1*k2)+float(h1*k2+h2*k1)/2.0
            fi=fi+3.0/4.0*(a/c)**2.0*l1*l2
            f=float(h1*h1+k1*k1+k1*h1)+3.0/4.0*(a/c)**2.0*l1*l1
            f=f*(float(h2*h2+k2*k2+k2*h2)+3./4.*(a/c)**2.*l2*l2)
            f=sqrt(f)
            fi=acos(fi/f)*180.0/3.1415926
            d1(j)=d
            fi1(j)=fi
15  continue
    if (m .ne.1) then
        fi0(m)=abs(fi0(m)-fi0(1))
        if (fi0(m) .gt. 180.0) then
            fi0(m)=360.0-fi0(m)
        endif
        f= fi0(m)
        go to 20
    endif
18  f=0.0
20  write (6,101) h1,k1,l1,d0(m),f,d1(1),fi1(1)
    m=m+1
100 go to 10
101 format(1x,'(',3(I2)')',2(3x,F6.3,2x,f5.1))
102 format(13x,'d(o)   an(o)',(4x,'d(c)',3x,'an(c)'))
103 format (////,1x,'hex a=',f5.3,5x,(2x,'r=', f4.2,
    &          1x, 'c=',f5.3))
104 stop
    end

```

#### 4. hex2 angle between zone axes

```

    program hex2
c*****
c*
c*   this program is for plotting a table of angles
c*   between different zone axes with a given c/a.
c*
c*   variable:  x=u-sin(pi/6)*v
c*              y=v*cos(pi/6)
c*              z=(c/a)*u
c*
c*
c*              x1*x2+y1*y2+z1*z2
c* cos(fi)=-----
c*          sqrt((x1*x1+y1*y1+z1*z1)*(x2*x2+y2*y2+z2*z2))
c*
c*****
    real x(20),y(20),z(20)
    integer u(20),v(20),w(20)
    real r,fi(20)

```

```

character s*1
open (7,file='hex2in',status='old')
open (6,file='lpt1:',status='new')
rewind 7
read (7,*) r
write (6,103) r
m=0
10  m=m+1
    read(7,*) u(m),v(m),w(m)
    if (u(m).eq.0 .and. v(m).eq.0.and.w(m).eq.0) goto 14
    go to 10
14  m=m-1
    write (6,102) (u(i),v(i),w(i), i=1,m)
    do 15  i=1,m
        x(i)=float(u(i))-float(v(i))*sin(3.1415926/6.0)
        y(i)=float(v(i))*cos(3.1415926/6.0)
        z(i)=r*float(w(i))
15  continue
    do 30 i=1,m
    do 18 j=1,m
        fi(j)=x(i)*x(j)+y(i)*y(j)+z(i)*z(j)
        f=x(i)*x(i)+y(i)*y(i)+z(i)*z(i)
        f=f*(x(j)*x(j)+y(j)*y(j)+z(j)*z(j))
        f=sqrt(f)
        fi(j)=acos(fi(j)/f)*180.0/3.1415926
18  continue
    write (6,101) u(i),v(i),w(i),(fi(j),j=1,m)
30  continue
101 format (1x,[' ',3(I1),'] ',15(1x,F5.1))
102 format (//,1x,['zone] [' ',15(3(I1),'] [''])
103 format (////,1x,'hex angles between zone axis',3x,
           'c/a=',f5.3)
stop
end

```

### 5. hex3 intensity of x-ray diffraction

```

program hex3
c*****
c*
c*  this program is for plotting a table of hcp structure *
c*  factors of superlattice---F(hkl)**2 to represent *
c*  the diffraction intensity. *
c*
c*  variable: *
c*      F(hkl)**2=cos(2*pi*(h*x(i)+k*y(i)+l*z(i))**2 *
c*                +sin(2*pi*(h*x(i)+k*y(i)+l*z(i))**2 *
c*
c*****
real x(12),y(12),z(12)
integer h(20),k(20),l(20)

```

```

real f1,f2,f(20)
character s*1
open (7,file='hex3in',status='old')
open (6,file='lpt1:',status='new')
rewind 7
do 10 i=1,12
    read(7,*) x(m),y(m),z(m)
10  continue
    write (6,102)
    m=0
12  m=m+1
    read(7,*) h(m),k(m),l(m)
    if (h(m).eq.0 .and. k(m).eq.0.and.l(m).eq.0) goto 14
    go to 12
14  m=m-1
    do 20 i=1,m
        f1=0.0
        f2=0.0
        do 15 j=1,12
            f1=f1+cos(h(m)*x(j)+k(m)*y(j)+l(m)*z(j))
            f2=f2+sin(h(m)*x(j)+k(m)*y(j)+l(m)*z(j))
15  continue
        f(m)=f1**2.0+f2**2.0
        write (6,101) h(m),k(m),l(m),f(m)
20  continue
101 format (1x,'(',3(I2),')',1x,F7.4))
102 format (//,1x,'( zone )',1x,'F[hkl]',/)
stop
end

```

#### 6. hex4 indices transformations between hcp and superhexagonal coordinate systems

```

program hex4
c*****
c*
c*  this program is for plotting a table of indices of
c*  directions and planes in superhexagonal and hcp
c*
c*  variable:
c*      H      1  -1  0  h      h      2/3   1/3  0  H
c*      K =    1   2  0  k      k = -1/3  1/3  0  K
c*      L      0   0  2  l      l      0    0  1/2  L
c*
c*****
    real h1(100),k1(100),l1(100)
    integer loop, h(100),k(100),l(100)
    open (7,file='hex4in',status='old')
    open (6,file='lpt1:',status='new')
    rewind 7
5  read (7,*) loop

```

```

m=0
12  m=m+1
    read(7,*) h(m),k(m),l(m)
    if (h(m).eq.0 .and. k(m).eq.0.and.l(m).eq.0) goto 14
    go to 12
14  m=m-1
    if (loop.eq.2) goto 40
    if (loop.eq.3) goto 60
    if (loop.eq.4) goto 80
    do 20 i=1,m
        h1(i)=2./3.*float(h(i))+1./3.*float(k(i))
        k1(i)=-1./3.*float(h(i))+1./3.*float(k(i))
        l1(i)=.5*float(l(i))
20  continue
    write (6,111)
25  do 30 i=1,m
        write (6,121) i, h(i),k(i),l(i),h1(i),k1(i),l1(i)
30  continue
    go to 5

40  do 50 i=1,m
        h1(i)=float(h(i)-k(i))
        k1(i)=float(h(i)+2*k(i))
        l1(i)=float(2*l(i))
50  continue
    write (6,112)
    do 55 i=1,m
        write (6,121) i,h(i),k(i),l(i),h1(i),k1(i),l1(i)
55  continue
    goto 5

60  do 70 i=1,m
        h1(i)=float(h(i)+k(i))
        k1(i)=float(-h(i)+2*k(i))
        l1(i)=float(2*l(i))
70  continue
    write (6,113)
    do 75 i=1,m
        write (6,123) i,h(i),k(i),l(i),h1(i),k1(i),l1(i)
75  continue
    goto 5

80  do 95 i=1,m
        h1(i)=2./3.*float(h(i))-1./3.*float(k(i))
        k1(i)=1./3.*float(h(i))+1./3.*float(k(i))
        l1(i)=.5*float(l(i))
95  continue
    write (6,114)
    do 98 i=1,m
        write (6,123) i,h(i),k(i),l(i),h1(i),k1(i),l1(i)
98  continue
111 format (/ ,1x, 'LOOP1 (HKL)==>(h k l) ')
112 format (/ ,1x, 'LOOP2 (hkl)==>(H K L) ')
113 format (/ ,1x, 'LOOP3 [UVW]==>[u v w] ')

```

```

114 format (/ ,1x, 'LOOP4 [uvw]==>[U V W]')
121 format (1x,I2,'. (' ,3I2,')',3x, '(' ,3F6.2,')')
123 format (1x,I2,'. [' ,3I2,']',3x, '[' ,3F6.2,']')
      stop
      end

```

7. hex5 indices transformations between 3- and 4- axis system

```

      program hex5
c*****
c*
c* this program is for plotting a table of indices of
c* directions of hex. in 3 axis and 4 axis systems
c*
c*****
      real u1(100),v1(100),t1(100),w1(100)
      integer loop, u(100),v(100),w(100),t(100)
      open (7,file='hex5in',status='old')
      open (6,file='lpt1:',status='new')
      rewind 7
5     read (7,*) loop
      m=0
12    m=m+1
      read(7,*) u(m),v(m),w(m),
      if (u(m).eq.0 .and. v(m).eq.0.and.w(m).eq.0) goto 14
      go to 12
14    m=m-1
c     if (loop.eq.2) goto 40
      do 20 i=1,m
          u1(i)=2./3.*float(u(i))-1./3.*float(v(i))
          v1(i)=-1./3.*float(u(i))+2./3.*float(v(i))
          t1(i)=-u1(i)-v1(i)
          w1(i)=float(w(i))
20    continue
      write (6,111)
25    do 30 i=1,m
          write (6,121) i,u(i),v(i),w(i),u1(i),v1(i),
&                t1(i), w1(i)
30    continue
      read (7,*) loop
      m=0
32    m=m+1
      read(7,*) u(m),v(m),t(m), w(m)
      if (u(m).eq.0.and.v(m).eq.0 .and.t(m).eq.0.and.
&      w(m).eq.0) goto 34
      go to 32
34    m=m-1
40    do 50 i=1,m
          u1(i)=float(u(i)-t(i))
          v1(i)=float(v(i)-t(i))

```



```

        w1(i)=float(w(i))
50  continue
    write (6,112)
    do 55 i=1,m
        write (6,123) i,u(i),v(i),t(i),w(i),u1(i),
&                v1(i),w1(i)
55  continue
111 format (/ ,1x,'LOOP1  [UVW]=>[u v t w]')
112 format (/ ,1x,'LOOP2  [uvw]==>[U V W]')
121 format (1x,I2,'.  [' ,3I2,']',3x,[' ,4F6.2,']')
123 format (1x,I2,'.  [' ,4I2,']',3x,[' ,3F6.2,']')
    stop
    end

```

8. hex6 draw the superhexagonal model in 3-D by known euler angles.

```

SET MODE"EGA"
LIBRARY"QQ.TRC"
SET WINDOW -5*1.38,5*1.38, -5,5
!-----
DIM A(0:1000),B(0:1000)
FOR W=90 TO 360 STEP 2022
    LET FI=w
    LET SETA=12
    LET PSI=-15
!   PRINT "FI=";FI
!   PRINT "SETA=";SETA
!   PRINT "PSI=";PSI
!-----
LET J=0                                !OUTER 6 PARTICLES
LET R=1
FOR Z=-.92 TO .92 STEP .92
    LET J=J+1
    CALL PLOT3D(FI,SETA, PAI,0,0,Z,A(J),B(J))
    CALL PLOT3D(FI,SETA,PSI,1/6,3^(.5)/6,Z-.46,A(45+J),
        B(45+J))
    FOR I=0 TO 6 STEP 1
        LET J=J+1
        LET T=60*I
        LET X=R*COS(T*PI/180)
        LET Y=R*SIN(T*PI/180)
        CALL PLOT3D(FI,SETA,PSI,X,Y,Z,A(J),B(J))
        CALL PLOT3D(FI,SETA,PSI,X+1/6,Y+3^(.5)/6,Z-.46,
            A(45+J),B(45+J))
        IF J=18 THEN CALL PLOT3D(FI,SETA,PSI,0,0,0,A(45+J),
            B(45+J))
        IF J=24 THEN CALL PLOT3D(FI,SETA,PSI,0,0,0,A(45+J),
            B(45+J))
        IF J=30 THEN CALL PLOT3D(FI,SETA,PSI,0,0,0,A(45+J),
            B(45+J))

```

```

IF J=16 THEN CALL PLOT3D(FI,SETA,PSI,0,0,0,A(45+J),
                        B(45+J))
IF J=11 THEN CALL PLOT3D(FI,SETA,PSI,X-1/3,Y-3^(.5),
                        Z-.46,A(45+J),B(45+J))
IF J=19 THEN CALL PLOT3D(FI,SETA,PSI,X-1/3,Y-3^(.5),
                        Z-.46,A(45+J),B(45+J))
IF J=12 THEN CALL PLOT3D(FI,SETA,PSI,X-1/3,
                        Y-2/3^(.5),Z-.46,A(45+J),B(45+J))
IF J=20 THEN CALL PLOT3D(FI,SETA,PSI,X-1/3,
                        Y-2/3^(.5),Z-.46,A(45+J),B(45+J))
NEXT I
NEXT Z
!-----
LET R=R/(3)^(0.5)                !INNER 6 PARTICLES
FOR Z=-.92 TO .92 STEP .92
FOR I=0 TO 6 STEP 1
  LET J=J+1
  LET T=60*I+30
  LET X=R*COS(T*PI/180)
  LET Y=R*SIN(T*PI/180)
  CALL PLOT3D(FI,SETA,PSI,X,Y,Z,A(J),B(J))
  CALL PLOT3D(FI,SETA,PSI,X+1/6, Y+3^(.5)/6,Z-.46,A(45+J),
              B(45+J))
NEXT I
NEXT Z
!*****PLOT THE SOLUTION *****
clear
PRINT "FI="; FI
PRINT "SETA="; SETA
PRINT "PSI="; PSI
!-----
LET J=0                !OUTER 6 PARTICLES
FOR Z=-1 TO 1
FOR I=0 TO 7 STEP 1
  LET J=J+1
  SET COLOR 11
  CALL FLOOD(0.1,0.1,A(J),B(J)*.9,11,11)
  IF Z>=0 THEN CALL CIRCLE(0.1,0.1,A(45+J),B(45+J)*.9,2,2)
NEXT I
NEXT Z
!-----
FOR Z=-1 TO 1                !INNER 6 PARTICLES
FOR I=0 TO 6 STEP 1
  LET J=J+1
  SET COLOR 11
  CALL FLOOD(0.1,0.1,A(J),B(J)*.9,11,11)
  IF Z>=0 THEN CALL CIRCLE(0.1,0.1,A(45+J),B(45+J)*.9,2,2)
NEXT I
NEXT Z
!-----
LET J=0                ! CONNECT THE OUTER 6 PARTICLES
FOR Z=-1 TO 1

```

```

FOR I=0 TO 7 STEP 1
  LET J=J+1
  SET COLOR 6
  PLOT A(1+(Z+1)*8),B(1+(Z+1)*8)*.9;A(J),B(J)*.9
  IF I<=6 THEN PLOT A(J),B(J)*.9;A(J+1),B(J+1)*.9
NEXT I
NEXT Z
!-----
FOR Z=-1 TO 1                                ! CONNECT THE INNER 6 PARTICLES
FOR I=0 TO 6 STEP 1
  LET J=J+1
  SET COLOR 6
  PLOT A(1+(Z+1)*8),B(1+(Z+1)*8)*.9;A(J),B(J)*.9
  IF I<=5 THEN PLOT A(J),B(J)*.9;A(J+1),B(J+1)*.9
NEXT I
NEXT Z
!-----
FOR J=1 TO 8                                  ! CONNECT VERTICAL OUTLINE
  PLOT A(J), B(J)*.9; A(16+J),B(16+J)*.9
NEXT J
FOR J=25 TO 38
  PLOT A(J),B(J)*.9; A(7+J),B(7+J)*.9
NEXT J
CALL CARTESIAN1(FI,SETA,PSI)
!CLEAR
!-----
NEXT W
PRINT
END

```

APPENDIX D

CuK<sub>β</sub> PEAKS IN THE X-RAY SPECTRA FROM  
GENERAL ELECTRIC XRD-5 D/F UNIT

## APPENDIX D

CuK<sub>β</sub> PEAKS IN THE X-RAY SPECTRA FROM  
GENERAL ELECTRIC XRD-5 D/F UNIT

K<sub>β</sub> peaks in the x-ray spectra probably have been ignored for a long time, when spectra were taken with the diffractometer unit, General Electric XRD-5 D/F, located in the x-ray crystallography laboratory, room #212, Science Building I. Spectra from samples of gold film, chromium film, sodium chloride powder and rock salt show strong CuK<sub>β</sub> peaks which have heights about 5 to 10 percent of those from CuK<sub>α</sub> peaks. These CuK<sub>β</sub> peaks have been confusing and leading to incorrect analysis of sample crystal structures. Even though a Ni filter was used to absorb CuK<sub>β</sub> X-rays, it is not completely effective. So strong CuK<sub>β</sub> still can go through it together with CuK<sub>α</sub>. The standard x-ray spectra from silicon dioxide (α-quartz), chart #1, and from sample silicon, chart #2, both on the wall of the x-ray laboratory, also show strong CuK<sub>β</sub> peaks. Unfortunately, the CuK<sub>β</sub> peaks in both spectra have been labeled as impurities. These are not due to the impurities in the samples instead "impurity" CuK<sub>β</sub> in the x-ray beam mixed with CuK<sub>α</sub>.

In the table below are the data from samples of gold film, chromium film, sodium chloride powder, rock salt, silicon dioxide and silicon. Spectra for the last two samples are on the wall in the x-ray laboratory. d-spacings of crystal structures calculated from peaks due to CuK<sub>α</sub> and CuK<sub>β</sub> rays are compared. Also the peak height ratios are estimated if possible and put in the last column. The calculated d-spacings are of the same values for CuK<sub>α</sub> and CuK<sub>β</sub>, within experimental error. This indicates that the existence of CuK<sub>β</sub> x-rays in the incidence beam was true. The ratios of peaks suggest that the relative intensity of CuK<sub>β</sub> may be 5 to 10 percent of that of CuK<sub>α</sub> in the incidence beam. These effects should not have been ignored.

TABLE XIV

## X-RAY DIFFRACTIONS OF VARIOUS SAMPLES

sample	hkl	CuK $_{\alpha}$ =1.54178Å			CuK $_{\beta}$ =1.39217Å			$\frac{P_{k\beta}}{P_{k\alpha}}$
		2 $\theta$	intensity	d-sp.	2 $\theta$	intensity	d-sp.	
gold	111	38.4		2.342	34.6	24.0	2.355	
	222	82.0	36	1.175	72.7	1.5	1.174	0.04
Cr	200	64.5		1.443	58.2	4.0	1.431	
NaCl powder	200	32.1	83	2.821	28.6	7.5	2.821	0.09
rock salt	200	31.7		2.823	29.9	6.0	2.838	
	220	45.4		1.998	40.8	1.5	1.997	
silicon dioxide chart#1	100	20.84	86	4.26	18.8	3.5	4.262	0.04
	101	26.44		3.343	24.1	17.0	3.334	
	110	36.52	39	2.458	33.0	2.0	2.451	0.05
	102	39.46	35	2.282	35.6	1.5	2.277	0.04
	112	50.16	55.5	1.817	45.1	2.5	1.815	0.045
	211	59.98	43	1.541	53.8	2.0	1.539	0.047
silicon chart#2	111	28.42	48	3.138	25.8	4.5	3.118	0.094
	220	47.30	44	1.920	42.7	3.5	1.912	0.080
	311	56.10	25.5	1.638	50.6	2.0	1.629	0.078
	422	88.05	18	1.108	78.0	1.3	1.106	0.072